

Light Trapping with Plasmonic Back Contacts in Thin-Film Silicon Solar Cells

Ulrich Wilhelm Paetzold

Forschungszentrum Jülich GmbH
Institute of energy- and climate research (IEK)
Photovoltaics (IEK-5)

Light Trapping with Plasmonic Back Contacts in Thin-Film Silicon Solar Cells

Ulrich Wilhelm Paetzold

Schriften des Forschungszentrums Jülich
Reihe Energie & Umwelt / Energy & Environment

Band / Volume 185

ISSN 1866-1793

ISBN 978-3-89336-895-2

Bibliographic information published by the Deutsche Nationalbibliothek.
The Deutsche Nationalbibliothek lists this publication in the Deutsche
Nationalbibliografie; detailed bibliographic data are available in the
Internet at <http://dnb.d-nb.de>.

Publisher and
Distributor: Forschungszentrum Jülich GmbH
Zentralbibliothek
52425 Jülich
Tel: +49 2461 61-5368
Fax: +49 2461 61-6103
Email: zb-publikation@fz-juelich.de
www.fz-juelich.de/zb

Cover Design: Grafische Medien, Forschungszentrum Jülich GmbH

Printer: Grafische Medien, Forschungszentrum Jülich GmbH

Copyright: Forschungszentrum Jülich 2013

Schriften des Forschungszentrums Jülich
Reihe Energie & Umwelt / Energy & Environment, Band / Volume 185

D 82 (Diss., RWTH Aachen, University, 2013)

ISSN 1866-1793
ISBN 978-3-89336-895-2

Neither this book nor any part of it may be reproduced or transmitted in any form or by any
means, electronic or mechanical, including photocopying, microfilming, and recording, or by any
information storage and retrieval system, without permission in writing from the publisher.

Doing science is like being on a venturesome and endless expedition! An expedition into the exciting landscapes of reality. An expedition which challenges us to explain nature with the simple rules of logic. An expedition which deserves all efforts as long as it serves humanity!

– Enjoy this expedition!

Summary

Trapping light in silicon solar cells is essential as it allows an increase in the absorption of incident sunlight in optically thin silicon absorber layers. This way, the costs of the solar cells can be reduced by lowering the material consumption and decreasing the physical constraints on the material quality. In this work, plasmonic light trapping with Ag back contacts in thin-film silicon solar cells is studied. Solar cell prototypes with plasmonic back contacts are presented along with optical simulations of these devices and general design considerations of plasmonic back contacts.

Based on three-dimensional electromagnetic simulations, the conceptual design of plasmonic nanostructures on Ag back contacts in thin-film silicon solar cells is studied in this work. Optimizations of the nanostructures regarding their ability to scatter incident light at low optical losses into large angles in the silicon absorber layers of the thin-film silicon solar cells are presented. Geometrical parameters as well as the embedding dielectric layer stack of the nanostructures on Ag layers are varied. Periodic as well as isolated hemispherical Ag nanostructures of dimensions above 200 nm are found to scatter incident light at high efficiencies and low optical losses. Hence, these nanostructures are of interest for light trapping in solar cells. In contrast, small Ag nanostructures of dimension below 100 nm are found to induce optical losses.

At the surface of randomly textured Ag back contacts small Ag nanostructures exist which induce optical losses. In this work, the relevance of these localized plasmon induced optical losses as well as optical losses caused by propagating plasmons are investigated with regard to the reflectance of the textured back contacts. In state-of-the-art solar cells, the plasmon-induced optical losses are shifted out of the relevant wavelength range by incorporating a ZnO:Al interlayer of low refractive index at the back contact. The additional but small potential for increasing the reflection at the back contact with dielectric interlayers of even lower refractive index, such as SiO₂ and air, is demonstrated.

The light-trapping effect of two types of plasmonic back contacts, which make use of large and efficiently scattering Ag nanostructures, is studied in thin-film silicon solar cell prototypes. The first type of plasmonic back contact applies non-ordered Ag nanostructures. The preparation, characterization and three-dimensional electromagnetic simulations of these back contacts with various distributions of non-ordered Ag nanostructures are presented. Measured reflectance spectra of the Ag back contacts with non-ordered nanostructures are correlated with reflectance spectra derived from three-dimensional electromagnetic simulations of isolated nanostructures on Ag back contacts. A microcrystalline silicon solar cell fabricated on one type of plasmonic Ag back contact with non-ordered Ag nanostructures shows a significantly enhanced plasmonic light trapping when compared with a flat solar cell.

The second type of plasmonic back contact applies periodic arrangements of plasmonic nanostructures in a square lattice at the surface of the Ag back contact. It is called a plasmonic reflection grating back contact. A particular advantage of this device is the control of the scattering angles via the diffraction orders of the grating while taking advantage of the efficient plasmon-induced light scattering at the Ag nanostructures. The plasmonic reflection grating back contacts are prepared with a nanoimprint process. They are implemented in microcrystalline thin-film solar cells prototypes. The prototypes exhibit a very good light-trapping effect. Even in comparison with solar cells with a state-of-the-art random texture for light trapping, an enhanced light-trapping effect is demonstrated for a solar cell with a plasmonic reflection grating back contact of optimized period. Based on electromagnetic simulations, the light-trapping effect caused by the plasmonic reflection grating back contact is explained from the intuitive perspective of geometrical optics as well as from the perspective of leaky waveguides. The obtained excellent agreement between the measured and simulated spectral response of the prototype solar cells allowed a simulation based optimization of the geometric parameters of the plasmonic reflection grating back contact. An additional significant improvement potential of thin-film silicon solar cells with plasmonic reflection grating back contacts is shown. The demonstrated light-trapping effect of plasmonic reflection grating back contacts is the first experimental proof that plasmonic nanostructures can induce a light-trapping effect competitive with the state-of-the-art random texture for light trapping in microcrystalline thin-film silicon solar cells. Improved plasmonic reflection grating back contacts are likely able to induce a light-trapping effect which leads even to significantly improved energy conversion efficiencies.

Zusammenfassung

Konzepte zur Lichtsammlung, sogenannte Lichtfallen, in Silizium-Solarzellen erlauben es die Absorption des einfallenden Sonnenlichtes in optisch dünnen Siliziumschichten zu erhöhen. Lichtfallen reduzieren die Kosten der Solarzellenproduktion, indem Absorbermaterial eingespart wird und die physikalischen Anforderungen an die Qualität des Materials reduziert werden. In dieser Arbeit werden plasmonische Ag-Rückkontakte in Dünnschicht-Silizium-Solarzellen im Hinblick auf deren Lichtfalleneigenschaften untersucht. Elektromagnetische Simulationen plasmonischer Ag-Rückkontakte werden einhergehend mit Prototypen der plasmonischen Rückkontakte in Dünnschicht-Silizium-Solarzellen präsentiert.

Zunächst werden die Ergebnisse grundlegender Untersuchungen zur Konzeption der plasmonischen Nanostrukturen auf Ag-Rückkontakten in mikrokristallinen Dünnschicht-Silizium-Solarzellen dargestellt. Die Untersuchungen basieren auf dreidimensionalen elektromagnetischen Simulationen. Ein Optimierungen der Form, Anordnung und des umgebenden Materials der Ag-Nanostrukturen im Hinblick auf deren Fähigkeit Licht mittels plasmonischer Effekte bei niedrigen Verlusten und hoher Streueffizienz in die mikrokristallinen Absorberschichten einzukoppeln ist beschrieben. Allgemein zeigt sich, dass periodische und auch vereinzelte halbsphärische Ag-Nanostrukturen von Strukturgrößen oberhalb von 200 nm sehr effizient Licht streuen. Allerdings zeigen kleine Ag-Nanostrukturen von Strukturgrößen unterhalb von 100 nm starke optische Verluste.

An rauen Ag-Rückkontakten konventioneller Dünnschicht-Silizium-Solarzellen treten Ag-Nanostrukturen von Strukturgrößen unterhalb von 100 nm auf. Die damit verbundenen plasmoneninduzierten optischen Verluste am Rückkontakt der Solarzellen werden in dieser Arbeit untersucht und diskutiert. Dabei werden sowohl propagierende Plasmonen als auch lokalisierte Plasmonen in den Ag-Nanostrukturen berücksichtigt. In konventionellen Dünnschicht-Silizium-Solarzellen wird eine ZnO:Al-

Schicht mit niedrigem Brechungsindex eingesetzt, um die plasmonischen Verluste aus dem relevanten Spektralbereich zu verschieben. In dieser Arbeit wird das darüber hinausgehende Potential von dielektrischen Zwischenschichten mit niedrigerem Brechungsindex demonstriert.

Zwei Ansätze zu plasmonischen Rückkontakten mit Lichtfallen-Eigenschaften in Dünnschicht-Silizium-Solarzellen werden in dieser Arbeit verfolgt. Der erste Ansatz basiert auf Ag-Rückkontakten mit ungeordneten Verteilungen von Ag-Nanostrukturen. Die Herstellung, Charakterisierung und dreidimensionale elektromagnetische Simulation dieser Rückkontakte ist dargestellt. Gemessene Reflexionsspektren dieser plasmonischen Rückkontakte wurden erfolgreich mittels der elektromagnetischen Simulationen einzelner Nanostrukturen, die lokalisierte plasmonische Resonanzen besitzen, nachgebildet. Dies zeigt, dass die diffuse Reflexion der Ag-Rückkontakte durch plasmonische Lichtstreuung verursacht wird. Eine mikrokristalline Solarzelle, die auf einem solchen plasmonischen Rückkontakt hergestellt wurde, zeigt eine erhöhte Lichtsammlung im Vergleich zu einer flachen Solarzelle.

Der zweite Ansatz dieser Arbeit zu plasmonischen Rückkontakten mit Lichtfallen-Eigenschaften in Dünnschicht-Silizium-Solarzellen verwendet periodisch angeordnete Ag-Nanostrukturen am Rückkontakt, die plasmonische Reflexionsgitter genannt werden. Ein implizierter Vorteil dieser Struktur ist die mögliche Kontrolle der Streuwinkel mittels der Beugungsordnungen des plasmonischen Gitters. Die plasmonischen Gitterstrukturen wurden in einem Nanoimprint-Prozess hergestellt. Prototypen der Dünnschicht-Silizium-Solarzellen, die plasmonische Reflexionsgitter verwenden, zeigen sehr gute Lichtfallen-Eigenschaften. Insbesondere konnte eine Verbesserung der Lichtausbeute im Vergleich zu konventionellen Dünnschicht-Silizium-Solarzellen mit rauer Lichtfallen-Textur erzielt werden. Basierend auf elektromagnetischen Simulationen wurde der Lichtfallen-Effekt der plasmonischen Gitter am Rückkontakt der Solarzelle untersucht. Sowohl eine intuitive Erklärung auf Basis der geometrischen Optik als auch eine Erklärung auf Basis der Wellenleitertheorie ist dargestellt. Die erzielte sehr gute Übereinstimmung der simulierten und gemessenen spektralen Antwort der Prototypensolarzellen erlaubt es die plasmonischen Gitter mittels Simulationen zu optimieren. Ein hohes Verbesserungspotential ist identifiziert. Der demonstrierte Lichtfallen-Effekt für plasmonische Gitter am Rückkontakt von Dünnschicht-Silizium-Solarzellen ist der erste experimentelle Nachweis, dass plasmonische Strukturen ein hohes Potential zur Verstärkung des Lichtfallen-Effektes in mikrokristallinen Dünnschicht-Silizium-Solarzellen besitzen.

Contents

Summary	III
Zusammenfassung	V
1 Introduction	1
2 Fundamentals	5
2.1 Thin-Film Silicon Solar Cells	5
2.1.1 Operating Principle	5
2.1.2 Device Structure and Materials	7
2.1.3 Characterization of Solar Cells and Materials	11
2.2 Electrodynamics, Photonics and Optics	15
2.2.1 Excursion into Classical Electrodynamics	15
2.2.2 Optics and Photonics	17
2.3 Plasmonics	20
2.3.1 Propagating Surface Plasmon Polaritons	21
2.3.2 Localized Surface Plasmon Polaritons	23
2.4 Optical Simulations	27
2.4.1 Finite Element Method for Maxwell's Equations	27
2.4.2 Optical Simulations with JCMsuite	28

2.4.3	Simulations of Localized Surface Plasmon Polaritons	31
3	Light Trapping	33
3.1	Fundamentals and Limits	33
3.2	State-of-the-Art Light Trapping	40
3.3	Plasmonic Light-Trapping Concepts	43
4	Nanoimprint Lithography - Replication of Light-Trapping Nanotextures	47
4.1	Introduction to Nanoimprint Lithography	48
4.2	Nanoimprint Lithography Process	48
4.3	Periodic Nanotextures for Light Trapping	51
4.4	Random Textures for Light Trapping	52
4.4.1	Replication Precision of Random Nanotextures	53
4.4.2	Prototype Thin-Film Silicon Solar Cells	54
4.5	Conclusion and Discussion	57
5	Design of Plasmonic Back Contacts for Light Trapping	61
5.1	Light Trapping with Plasmonic Back Contacts	61
5.2	Plasmonic Light Scattering of Nanostructures on Ag Back Contacts	64
5.2.1	Ag Nanoparticles vs. Nanostructures on Ag Back Contacts	64
5.2.2	Embedding Material of Nanostructures on Ag Back Contacts	66
5.2.3	Shape of Nanostructures on Ag Back Contacts	67
5.2.4	Light-Trapping with Plasmonic Light Scattering	69
5.3	Light Scattering at Plasmonic Reflection Grating Back Contacts	74
5.4	Conclusion	77
6	Plasmon-Induced Optical Losses at Textured Ag Back Contacts	79
6.1	Optical Losses at Textured Ag Surfaces	80
6.1.1	Preparation of Textured Ag Surfaces	80

6.1.2	Discussion of Plasmon-Induced Optical Losses	80
6.2	Avoiding Plasmon-Induced Optical Losses at Ag Back Contacts . . .	86
6.3	Conclusion	89
7	Plasmonic Back Contacts with Non-Ordered Ag Nanostructures	91
7.1	Preparation of Back Contacts with Non-Ordered Ag Nanostructures .	92
7.2	Optical Simulation of the Back Contacts	94
7.2.1	Reflectance of the Back Contacts in Air	94
7.2.2	Light Scattering into the $\mu\text{c-Si:H}$ Absorber Layer	100
7.3	Prototype $\mu\text{c-Si:H}$ Thin-Film Solar Cell	104
7.4	Conclusion	106
8	Plasmonic Reflection Grating Back Contacts	107
8.1	Prototype $\mu\text{c-Si:H}$ Thin-Film Solar Cell	108
8.1.1	Back Contact and Solar Cell Preparation	108
8.1.2	Results of the Prototype Solar Cells	110
8.1.3	Geometrical Optics Perspective on the Light-Trapping Effect	113
8.2	Optical Simulations of the Solar Cells	117
8.2.1	Optical Simulations of the Prototype Solar Cells	117
8.2.2	Optimization of the Light-Trapping Effect	124
8.3	Leaky Waveguide Perspective on the Light-Trapping Effect	126
8.4	Conclusion	133
9	Conclusion and Outlook	135
A	Optical Parametrization	139
B	Waveguide Modes in Planar Layer Stacks	143
	References	145

List of Symbols and Abbreviations	167
List of Publications	169
Acknowledgments	173
Curriculum Vitae	175

Chapter 1

Introduction

At the heart of a sustainable future, a fair and equitable access to clean electrical energy needs to be guaranteed to all people on this planet. Solar cells can generate the required amount of electrical energy by harvesting the globally available and inexhaustible energy resource of the sun. To allow a global widespread use of solar cells, their economic costs need to decrease. One way to reduce the economic costs of thin-film silicon solar cells is to enhance their potential to absorb incident solar radiation and transform it into electrical energy. In this regard, plasmonic light trapping with nanostructured Ag back contacts in thin-film silicon solar cells is studied in this work.

Meeting Global Energy Challenges By 2050, it is expected that around nine billion people will live on this planet [1]. At a human living standard, forecasts predict that these people need at least twice the annual energy generated today to clean their drinking water, heat their houses, light their homes or manufacture goods and so on [2, 3]. Providing this large amount of energy with low harm to the environment requires tremendously increasing the harvest of renewable energy sources [2, 4]. Only renewable energy sources like solar, wind, geothermal and hydro energy can be harvested almost all over this planet at low emissions of greenhouse gases and toxic by-products [5]. Therefore, the diffusion and further development of technologies to harvest renewable energy sources at low economic costs is one of the great challenges of this generation. Exemplary calculations show that only around 5% of the world's deserts would need to be covered by conventional solar cells to generate the required amount of global primary energy [5, 6]. Thus, in principle, the photovoltaic techno-

logies are ready to make their contribution to the renewable electricity generation. However, despite the tremendous price reduction of solar cells in the last decades, for a global widespread use of the photovoltaic technology, the economic costs of the solar cells still need to decrease strongly.

Solar Cells In 1954, the first practical solar cell was presented by Chapin, Fuller and Pearson [7]. Their solar cell was based on a silicon pn-junction of an n-doped crystalline silicon wafer covered by a thin p-doped silicon layer. Initially, solar cells were used in space applications [8]. Only since the early nineties of the last century, the amount of electricity generated from solar cells has tremendously increased to a noticeable proportion of the total world electricity generation [8]. This increase has continued up to date and in 2011 a total amount of 69.6 GWp of cumulative photovoltaic capacity was installed, which is sufficient to cover the annual power supply needed for around 20 million households [9]. The crystalline silicon solar cell, of similar device structure as the first practical solar cell, still dominates the world market with a share of around 88% in 2012 [9, 10]. The major cost reduction for this technology was achieved in the past decade by a vast advancement of the production technologies, reduction of costs for silicon wafers and the increased production volume – the annually installed power generation capacity increased from less than 0.3 GWp in 2000 to 29.7 GWp in 2011 [9]. In order to further decrease the costs, new solar cell devices aim for a reduction of the cost of the absorber materials. On the one hand, novel techniques to manufacture much thinner crystalline silicon absorber layers have been proposed [11, 12]. On the other hand, novel absorber materials and deposition techniques have been developed in thin-film solar cells and organic solar cells. Common absorber materials of thin-film solar cells are cadmium telluride, copper indium gallium diselenide as well as amorphous and microcrystalline silicon [13–15]. The thickness of the absorber layers in thin-film solar cells ranges from hundreds of nanometers to a few micrometers. In the past years, the market share of thin-film silicon solar cells has increased to around 12% in 2012 [10]. Thin-film silicon solar cells made of amorphous and microcrystalline silicon are the focus of this work. The particular advantages of this technology are the use of abundant and non-toxic materials as well as the availability of large scale manufacturing technologies [16, 17].

Plasmonic Light Trapping Light-trapping structures allow incident light to be guided in the absorber layer of a solar cell. This way, the absorptance of light in the solar cell can be enhanced beyond the absorption of a single light pass through the device. Light trapping induces several advantages for the design of a solar cell

device. First, it allows the reduction of the thickness of the absorber material. Second, in thinner solar cells, the charge carrier recombination is reduced [18,19]. Third, with decreasing thickness of the absorber layer, the requirements on the material such as stability of hydrogenated amorphous silicon with regard to light-induced degradation can be reduced. Thus, light trapping increases solar cell efficiencies and reduces the costs of generating electricity with solar cells. For thin-film silicon solar cells, light trapping is particularly important as the absorber layer of these solar cells is much thinner than the absorption lengths of incident light in relevant regions of the solar spectrum.

In the last decade, the research on nanooptics and plasmonics has developed numerous approaches and concepts for guiding and localizing light with metal nanostructures in dielectric layer stacks [20–25]. Making use of these concepts in the solar cell devices creates novel light-trapping concepts and new solar cell designs.

Scope of the Thesis In this work, plasmonic light trapping with nanostructured Ag back contacts in thin-film silicon solar cells is studied. General design considerations for the plasmonic back contacts are presented along with prototypes of thin-film silicon solar cells applying plasmonic Ag back contacts. The plasmonic back contacts are designed for the application in tandem thin-film silicon solar cells with microcrystalline silicon bottom solar cells. In these solar cells, light trapping is particularly relevant for light in the near-infrared spectral range. The plasmonic back contacts studied throughout this work address this spectral range.

Outline This thesis is organized as follows. In Chapter 2, essential fundamentals along with the experimental methods applied throughout this work are introduced. The review of the fundamentals of thin-film silicon solar cells, optics, plasmonics, and the applied three-dimensional electromagnetic simulation method shall help the reader to follow the content of this thesis. In Chapter 3, the limits of light trapping in solar cells as well as state-of-the-art light trapping in silicon solar cells are introduced. In addition, an overview of the field of plasmonic light trapping is presented. The development of the ultra violet nanoimprint lithography as an alternative preparation technique for nanotextures for light trapping in solar cells is presented in Chapter 4. In the following chapters results of plasmonic light trapping with Ag back contacts in thin-film silicon solar cells are presented. First, a study on general design principles of plasmonic Ag nanostructures on the back contact of thin-film silicon solar cells is presented in Chapter 5. For this study, the electromagnetic coupling of incident propagating light and localized plasmonic resonances in nanostructures on Ag

back contacts was simulated with a three-dimensional numerical solver of Maxwell's equations. An optimization of the Ag nanostructures on the back contacts in terms of plasmon-induced light scattering for light trapping in thin-film silicon solar cells is presented. Therefore, geometrical parameters as well as the embedding material of single and periodic nanostructures on Ag back contacts were varied.

A dominant non-radiative decay of plasmonic resonances in small Ag nanostructures induces optical losses. These losses decrease the reflectivity of Ag back contacts with the state-of-the-art random texture for light trapping. In Chapter 6, the absorbance spectra of such back contacts are discussed with regard to localized plasmon induced optical losses as well as propagating plasmon induced optical losses. The impact of the decreased reflectivity of the back contact on the spectral response of state-of-the-art thin-film silicon solar cells is shown. Furthermore, a potential to decrease the plasmon-induced optical losses by applying low refractive index intermediate layers is demonstrated.

A dominant radiative decay of plasmonic resonances in Ag nanostructures induces an efficient scattering of incident light. If this light scattering is directed into the absorber layer of a thin-film silicon solar cell, the metal nanostructures serve as sub-wavelength scattering components that couple incident propagating light into the thin absorber layers of the solar cells. In Chapter 7 and Chapter 8, two types of plasmonic back contacts are introduced which make use of plasmon-induced light scattering to induce a light-trapping effect in prototype solar cells. In Chapter 7, the light trapping in thin-film silicon solar cells which apply plasmonic back contacts with non-ordered Ag nanostructures is investigated. Measured optical reflectance spectra of the plasmonic back contacts with non-ordered nanostructures are compared with simulated reflectance spectra calculated from optical simulations of localized plasmon resonances in isolated nanostructures on Ag back contacts. Furthermore, the light trapping in a prototype microcrystalline silicon thin-film solar cell deposited on one promising type of Ag back contact with non-ordered nanostructures is studied. In Chapter 8, the optical simulation and development of prototypes of microcrystalline silicon thin-film solar cells applying plasmonic reflection grating back contacts is presented. The plasmonic reflection grating back contacts consist of Ag nanostructures which are arranged in a square lattice on the back contact of the solar cell. Based on experimental and numerical studies, the light trapping in solar cells with plasmonic reflection grating back contacts is explained from the perspective of geometrical optics as well as waveguide theory.

Chapter 2

Fundamentals

This chapter provides a brief introduction and a review of essential fundamentals along with experimental methods applied in this work. In the first section, the working principle, device structure and characterization of thin-film silicon solar cells are presented. The second section provides a brief summary of classical electrodynamics and optics. In the third section, the fundamentals of plasmonics are introduced. The last section introduces the electromagnetic simulation method applied in this work.

2.1 Thin-Film Silicon Solar Cells

2.1.1 Operating Principle

The solar cell is an optoelectronic device that converts sunlight into electrical power. In this section, the working principle of a thin-film silicon solar cell is presented. For a more detailed description of the theory on solar cells, the reader is directed to authoritative textbooks [26,27].

Basic Photovoltaic Operation Principle For any photovoltaic energy conversion process, a photon is absorbed via the excitation of an electron beyond an energy barrier. This way an electron-hole pair is induced which can be either free or bound in an exciton state. Then, after an optionally transmission, this electron-hole pair must be separated by some kind of selective contact in order to avoid its recombination. In a steady-state scenario of constant photon flux and closed electrical circuit,

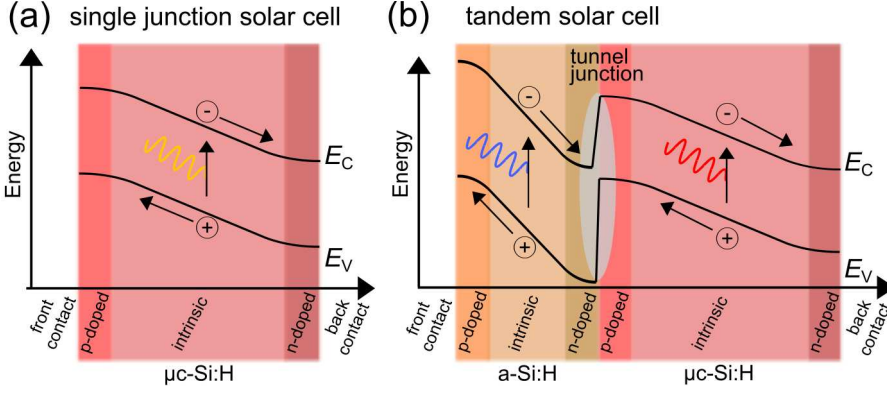


Figure 2.1: Band diagram of (a) a single junction μc -Si:H thin-film solar cell and (b) a tandem thin-film silicon solar cell.

the separated charge carriers induce a voltage across the device, called photovoltage, as well as a photocurrent. The generated electric power is given by multiplying the photocurrent and the photovoltage.

Single Junction Thin-Film Silicon Solar Cell In this work, thin-film silicon solar cells based on hydrogenated amorphous silicon (a -Si:H) [28–30] and hydrogenated microcrystalline silicon (μc -Si:H) [31–33] absorber layers are investigated. In these semiconductor materials, incident photons of energy larger than the band gap can be absorbed by exciting an electron from the energetically lower valence band (E_V) to the energetically higher conduction band (E_C) [26, 27, 29]. This produces free electron-hole pairs (see Figure 2.1 (a)). The electrons and holes are separated and directed towards the two contacts via an electric field. This electric field is created by the entropy-driven difference in the concentration of electrons and holes in the thin p-doped and n-doped layers at the front and rear sides of the solar cell [34].

Tandem Thin-Film Silicon Solar Cell In a single junction solar cell, on the one hand, only those photons of energy larger than the band gap of the absorber material can excite an electron-hole pair. On the other hand, the energy of photons which exceeds the band gap is lost due to thermalization of the charge carriers to the band edges of the absorber material. The resulting limitations on the conversion efficiency have been described first in [35]. In order to harvest a larger portion of the broadband solar energy, multiple single junction thin-film silicon solar cells of different absorber

materials are combined. For this work, the tandem thin-film silicon solar cell is in focus. In Figure 2.1 (b), the operation principle of a tandem thin-film silicon solar cell is illustrated. This device consists of an *a*-Si:H single junction solar cell and a μ c-Si:H single junction solar cell which are connected in series [36–39]. The *a*-Si:H top solar cell typically exhibits a band gap of 1.7–1.9 eV and the μ c-Si:H bottom solar cell typically exhibits a band gap of around 1.1 eV. Thus, the *a*-Si:H top cell absorbs light of short wavelengths of the solar spectrum and the μ c-Si:H bottom solar cell absorbs light of longer wavelengths of the solar spectrum. Due to a better match of tandem thin-film silicon solar cells to the solar spectrum, the overall efficiencies of this device are higher than the efficiencies achieved for single junction *a*-Si:H and μ c-Si:H solar cells. For tandem thin-film silicon solar cells, the highest reported initial and stabilized energy conversion efficiencies are 14.4% and 12.3% [40,41], respectively.

A major challenge for the development of tandem thin-film silicon solar cells is the required matching of the photocurrent in the top and bottom solar cell. As both single junction solar cells are connected in series, the generated charge carriers recombine at the n/p-tunnel junction in the centre of the device (see Figure 2.1 (b)). Thus, the total photocurrent of the solar cell is limited by the lower photocurrent of either the top or bottom solar cell. To match both photocurrents, intermediate reflectors are incorporated in high efficiency devices [42–44].

2.1.2 Device Structure and Materials

The core element of thin-film silicon solar cells is the afore described p-i-n diode of *a*-Si:H or μ c-Si:H. In addition, a transparent and conductive front contact and a conductive and reflective back contact are integral parts of the solar cell. Depending on whether a superstrate or a substrate is used for the preparation of the solar cell, the thin-film silicon solar cell is referred to as a solar cell in 'p-i-n configuration' or 'n-i-p configuration', respectively. To provide an example, Figure 2.2 (a) and Figure 2.2 (b) show schematic cross-sections of μ c-Si:H thin-film solar cells in p-i-n configuration and in n-i-p configuration, respectively. For the solar cell in p-i-n configuration, incident light travels through the glass superstrate and the transparent and conductive textured aluminium-doped zinc oxide (ZnO:Al) front electrode. The front ZnO:Al layer exhibits a texture needed to scatter and diffract incident light into the μ c-Si:H absorber layer of the solar cell (for details on the light trapping see Section 3.2). The adjacent p-i-n diode of μ c-Si:H exhibits a thin p-doped μ c-Si:H layer of 10 nm–30 nm,

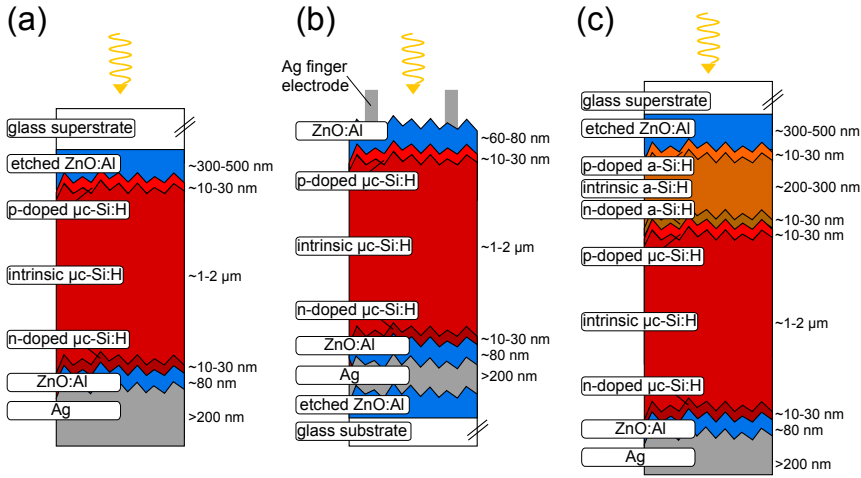


Figure 2.2: Cross-section of (a) a single junction $\mu\text{c-Si:H}$ thin-film solar cell in p-i-n configuration, (b) a single junction $\mu\text{c-Si:H}$ thin-film solar cell in n-i-p configuration and (c) a tandem thin-film silicon solar cell.

a 1 μm - 2 μm thick intrinsic $\mu\text{c-Si:H}$ layer and a thin n-doped $\mu\text{c-Si:H}$ layer of 10 nm-30 nm. The conductive and reflective back contact consists of an 80 nm thick ZnO:Al interlayer and a Ag back layer of thickness larger than 200 nm. In thin-film solar cells in n-i-p configuration, the deposition order of the layers is inverse (see Figure 2.2 (b)). However, in the n-i-p configuration, incident light does not travel through the substrate, which allows the substrate to be modified independently of its transparency. Due to enhanced incoupling of incident light, the layer thickness of the ZnO:Al front contact is only around 80 nm for solar cells in n-i-p configurations [45]. This results in a low conductivity which is compensated by additional Ag finger electrodes on the front contact of thin-film silicon solar cells in n-i-p configuration. The layer stack of $\alpha\text{-Si:H}$ thin-film solar cells is similar to the above presented $\mu\text{c-Si:H}$ thin-film solar cells, but the intrinsic absorber layer thickness of $\alpha\text{-Si:H}$ is much thinner (between 200 nm to 350 nm). In addition, Figure 2.2 (c) shows a tandem thin-film silicon solar cells which consists of an $\alpha\text{-Si:H}$ top solar cell and a $\mu\text{c-Si:H}$ bottom solar cell which are deposited one after the other.

ZnO:Al as Transparent and Conductive Front Contact Several materials and deposition processes have been investigated in the past to prepare transparent and

conductive front contacts which have a good texture for light trapping in thin-film silicon solar cells. Prominent examples are sputtered and wet-chemically etched ZnO:Al layers [46–48], as-deposited grown SnO₂ layers [49, 50] or as-deposited grown ZnO:Al layers prepared by low pressure chemical vapor deposition [51]. In this work, wet-chemically etched ZnO:Al layers are used which are deposited by radio frequency magnetron sputtering [52]. The transparency and conductivity of the sputtered ZnO:Al layers highly depends on numerous deposition parameters such as the temperature, the pressure, the deposition power, the oxygen flow added as well as the Al₂O₃ doping of the ZnO:Al₂O₃ sputtering target [46, 53–56]. Furthermore, the deposition parameters influence the layer growth and in turn the etching behavior of the ZnO:Al layers, which are typically wet-chemically etched for around 40s in 0.5 w/w% HCl. Due to the complexity of the deposition parameter setting, identifying a stable sputtering process which yields optimal ZnO:Al front electrodes for thin-film silicon solar cells is an on-going field of research. The textured ZnO:Al front contacts applied in this work were deposited at substrate temperatures of around 300 °C and a sputtering target doping level of around 0.5 wt%. For the ZnO:Al interlayer and the thin ZnO:Al front contact of solar cells in n-i-p configuration, the deposition temperature was reduced to room temperature and 150 °C, respectively.

Hydrogenated Amorphous Silicon Amorphous silicon (*a*-Si) exhibits no long range order of the silicon atoms due to variations of their bond lengths and bond angles. Nevertheless, the local order is sufficient for the formation of bands of the electron energy levels [29, 57]. Thus, *a*-Si is a semiconductor. However, due to the disorder of the material, some atoms in *a*-Si have dangling bonds which create a large number of defect states within the band gap. In order to enhance the quality of the *a*-Si semiconductor, the dangling bonds need to be saturated by hydrogen atoms [29]. The resulting material is called hydrogenated amorphous silicon (*a*-Si:H).

In *a*-Si:H, due to the disorder, the band edges of the valence band and the conduction band exhibit localized tail states that extend into the band gap. As a result, the band gap is not well defined. Instead, it is defined via the mobility of charge carriers, which is strongly decreased in the localized tail states. Typical band gaps of *a*-Si:H are 1.7–1.9 eV [29, 57]. Another aspect related to the disorder in the *a*-Si:H is that the crystal momentum is not a good quantum number. Thus, *a*-Si:H acts as a quasi-direct semiconductor with much higher absorptivity when comparing with crystalline silicon, which is an indirect semiconductor.

A major drawback of *a*-Si:H thin-film solar cells is the light-induced degradation of the *a*-Si:H material. This degradation was first described by Staebler and Wron-

ski [58]. The commonly accepted model for this effect states that weak strained silicon-silicon bonds can break under illumination and induce additional dangling bonds. These dangling bonds create additional recombination centers which lower the photoconductivity of the material. High quality *a*-Si:H material for thin-film silicon solar cells is deposited from the gas phase. The gases silane and hydrogen are decomposed so that a deposition of silicon is possible (for details see [29, 59]). This decomposition is very efficient in a plasma enhanced chemical vapor deposition (PECVD) process.

Hydrogenated Microcrystalline Silicon Under certain deposition conditions, the afore mentioned PECVD deposition process of *a*-Si:H induces a crystalline silicon phase enclosed by an *a*-Si matrix in the deposited material [31, 33, 59–62]. The resulting two-phase material is called microcrystalline silicon. Due to the amorphous phase, the grain boundaries as well as possible voids in the microcrystalline silicon layers, microcrystalline silicon need to be passivated with hydrogen in order to form a high quality semiconductor material. For this hydrogenated microcrystalline silicon (μ c-Si:H), the crystalline grains grow columnar-wise on top of an amorphous incubation layer [61]. However, the exact morphology and crystalline volume fraction highly depend on the deposition conditions. For example, by decreasing the SiH₄ to H₂ ratio in the PECVD deposition chamber, the material growth can be varied from *a*-Si:H to μ c-Si:H of very high crystalline volume fraction. High quality μ c-Si:H for application in thin-film silicon solar cells has crystalline volume fractions of around 70%. Other important deposition parameters for the μ c-Si:H material are pressure, total gas flow, high frequency power, substrate temperature and excitation frequencies of the plasma. For more details on the material employed in this work, the reader is directed to the literature [45, 59, 61]. The band gap of high quality μ c-Si:H is around 1.1 eV. Thus, μ c-Si:H is able to absorb light in a much larger spectral range than *a*-Si:H. However, due to the indirect band gap, its absorptivity is lower in comparison with *a*-Si:H. For this reason, the μ c-Si:H absorber layer in a tandem thin-film silicon solar cell must be much thicker than the *a*-Si:H absorber layer.

Sputtered ZnO:Al Interlayer and Ag Back Layer The back contact of a thin-film silicon solar cell consists of an 80 nm thick ZnO:Al interlayer prepared by radio frequency magnetron sputtering and an optically thick Ag back layer. The Ag layer can be either deposited by dc-sputtering or physical vapor deposition.

2.1.3 Characterization of Solar Cells and Materials

Current Density - Voltage Characteristic The energy conversion efficiency is the ultimate figure of merit for all solar cells. It is derived from the current density - voltage characteristic (J - V characteristic) of the solar cell under illumination with the sun spectrum. There is an obvious dependency of the J - V characteristic on the illuminated sun spectrum. The reference spectrum used today to determine the conversion efficiency of solar cells is the AM1.5G173-03 spectrum [63, 64]. This spectrum, which is shown in Figure 2.3 (a), represents the solar irradiance (diffuse and specular components) onto a 37° tilted surface on earth which corresponds to an air mass of 1.5 times the atmosphere.

In Figure 2.3 (b), a typical J - V characteristic of a tandem thin film silicon solar cell, as introduced in the previous section, is shown. The important quantities are illustrated: the open-circuit voltage (V_{oc}), the short-circuit current density (J_{sc}), the voltage at the maximum power point (V_{mpp}), the current density at the maximum power point (J_{mpp}) and the maximum power ($P_{max} = J_{mpp} \cdot V_{mpp}$). Another important quantity is the fill factor ($FF = P_{max}/(V_{oc} \cdot J_{sc})$) which denotes the ratio of the power at the maximum power point and a hypothetical power calculated by multiplying the J_{sc} and the V_{oc} . Then, the conversion efficiency η of the solar cell is given as function of the irradiated power P_0 by:

$$\eta = \frac{P_{max}}{P_0} = \frac{J_{sc} \cdot V_{oc} \cdot FF}{P_0}. \quad (2.1)$$

External Quantum Efficiency Particularly for the analysis of light trapping in solar cells, the spectral response of a solar cell on the incident light is an important characteristic of the device. Usually, the spectral response of a solar cell is given by the external quantum efficiency (EQE). The EQE describes the probability of an incident photon of a given energy to generate an electron-hole pair that contributes to the J_{sc} . The EQE is measured by illuminating the solar cell with monochromatic light of in the investigated spectral range. The EQE is given by:

$$EQE(\lambda) = \frac{\tilde{J}_{ph}(\lambda)}{e \cdot \phi_p(\lambda)}, \quad (2.2)$$

where λ is the wavelength, e is the elementary charge, $\tilde{J}_{ph}(\lambda)$ is the photo-current induced by illuminating the solar cells with photon flux $\phi_p(\lambda)$. The measurements of

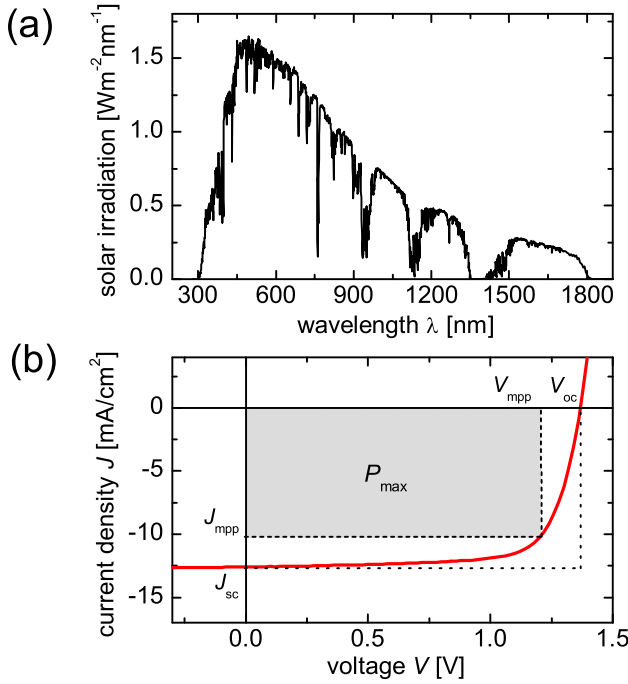


Figure 2.3: (a) Spectral irradiance of the AM1.5G173-03 spectrum [63, 64]. (b) Representative illuminated current density - voltage characteristic of a tandem thin-film silicon solar cell [65]. Indicated are the short-circuit current density (J_{sc}), the open-circuit voltage (V_{oc}), the current density at maximum power (J_{mpp}), the maximum power (P_{max}) and the voltage at maximum power (V_{mpp}).

the EQE are usually conducted at a voltage of 0 V. In this case, the J_{sc} can be calculated as an integral of the product of the EQE and the solar spectrum. The typical spectral resolution of the EQE measurements is around 10 nm in wavelengths.

In Figure 2.4, a typical EQE of a tandem thin-film silicon solar cell is shown. The EQE of each single junction solar cells is given as well as the total EQE . It is shown that only light of wavelengths shorter than 780 nm is absorbed in α -Si:H top cell with the high band gap. In turn, for wavelengths longer than 500 nm, the incident light passes at least partly through the α -Si:H top solar cell and can be absorbed in the μ c-Si:H bottom solar cell. It shall be noted, that due to the series connection, the EQE

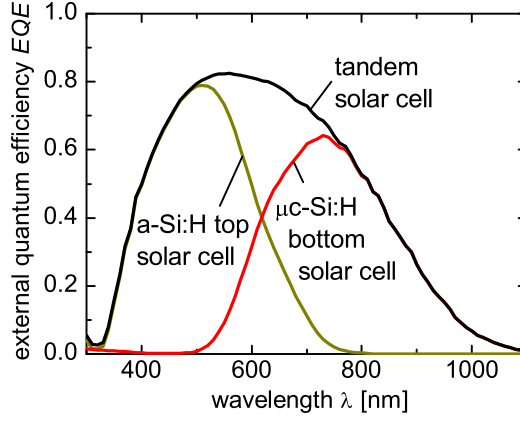


Figure 2.4: External quantum efficiency (EQE) of a tandem thin-film silicon solar cell [65]. Indicated are the EQE of the a -Si:H top solar cell, the μc -Si:H bottom solar cell as well as the EQE of the total tandem thin-film silicon solar cell.

of the top and bottom solar cell must be measured separately at co-bias illumination of light in a spectral range which is solely absorbed by one of the solar cells. The total EQE is then calculated by summing up the EQE of the a -Si:H and μc -Si:H solar cells.

Reflectance Measurements Reflectance measurements of thin-film silicon solar cells as well as layer stacks are carried out with a LAMBDA950 spectrophotometer (Perkin Elmer, Waltham, USA) [66]. This spectrophotometer uses a monochromator that allows the spectral analysis of the light reflected at or transmitted through a sample for wavelengths between 175 nm and 3300 nm. The incident beam of the light source is split into a probe beam and a reference beam. The probe beam enters an integrating Ulbrich sphere and impinges on the sample. Due to the highly reflective surface, the integrating Ulbrich sphere collects all light reflected in any direction at the sample. This way, the total reflectance (R_{tot}) is measured. In addition, the diffuse reflectance (R_{diff}) can be measured by excluding the light reflected specularly by the sample. The experimental setup encloses an angle of 8° for specular reflection. The uncertainty in the reflectance spectra presented throughout this work is below 2%. The absorbance (A) of a non-transparent solar cell or non-transparent dielectric layer stack is calculated by subtracting the reflectance from unity.

Scanning Electron Microscopy Scanning electron microscopy (SEM) is an experimental imaging method that images the surface of a sample by scanning it with a beam of electrons [67,68]. The electrons are emitted from a filament or field emission tip. They are accelerated and confined via an electron lens towards the surface of the sample. The focused spot of the electron beam scans across the sample surface. By evaluating the amount of secondary electrons, a brightness value can be assigned to each surface position. As the signals primarily result from interactions of the electron beam with atoms near the surface of the sample, the resulting brightness image provides a two-dimensional surface topography. In this work, the measurements were conducted with the scanning electron microscope Supra 55VP Smart-SEM (Carl Zeiss, Oberkochen, Germany). The images were taken under an angle of 45° and 60° with respect to the surface normal.

Atomic Force Microscopy Another method to determine the surface topography of a sample is the atomic force microscopy (AFM) [69,70]. This method uses a fine tip with a curvature radius of around 10 nm and opening angle of 30° . The tip is positioned at the end of a resonantly oscillating cantilever. As the tip approaches the surface of the sample, its resonance frequency is changed due to attractive van der Waals forces between the tip and the surface. The resulting change in the amplitude of the oscillating cantilever is detected. A feedback loop and a piezo-electric height control allow the distance between tip and surface to be kept constant as the tip scans across the surface (non-contact tapping mode). By detecting the position of the tip normal to the surface, a three-dimensional surface topography is mapped. The AFM measurements conducted in this work utilized a NANStation 300 (S.I.S GmbH, Herzogenrath, Germany). Due to the tilt and a drift of the AFM tip, a plane-fitted background was subtracted from the measured surface topographies with the software SPIP, version 5.1.6 (Image Metrology A/S, Horsholm, Denmark) [71].

Optical Data The optical data of the materials employed in this work are described via the complex refractive index (\tilde{n}). The complex refractive indices of intrinsic, p-doped and n-doped μc -Si:H and a -Si:H as well as front and back ZnO:Al layers are taken from a reference set of experimental data. These data are taken from measurements of state-of-the-art materials which are applied in thin-film silicon solar cells. The experimental methods applied are photothermal deflection spectroscopy, transmission and reflection measurements and ellipsometry. The optical data of Ag are taken from ellipsometry measurements performed on as-grown planar and optically thick Ag layers. The data agree, within the reported growth-dependent variations,

with reference data from literature [72, 73]. The data is presented in Appendix A. For details on the measurements see [74, 75].

2.2 Electrodynamics, Photonics and Optics

This section provides a brief introduction to classical electrodynamics which forms the theoretical basis of the light-matter interaction in thin-film silicon solar cells as well as for light-matter interaction of metal nanostructures which exhibit plasmons.

2.2.1 Excursion into Classical Electrodynamics

The theory of classical electrodynamics was condensed in 1873 by James Clerk Maxwell into a set of partial differential equations [76, 77]. It accurately describes the temporal and spatial evolution of electromagnetic fields. As long as quantum effects can be neglected, a combination of classical electrodynamics and solid state theory provides a complete description of classical optics.

Maxwell's Equations The central component in the theory of classical electrodynamics is a pair of vector fields, the electric field ($\mathbf{E}(\mathbf{x}, t)$) and the magnetic field ($\mathbf{H}(\mathbf{x}, t)$), where $\mathbf{x} = (x, y, z)$ determines the position in space and t is the time. In addition, the dielectric displacement ($\mathbf{D}(\mathbf{x}, t)$), the magnetic induction ($\mathbf{B}(\mathbf{x}, t)$), the external electric current density ($\mathbf{J}_{\text{ext}}(\mathbf{x}, t)$) and the scalar free charge density ($\rho_{\text{ext}}(\mathbf{x}, t)$) are needed for the formulation of Maxwell's equations (in the SI system of units):

$$\nabla \cdot \mathbf{D}(\mathbf{x}, t) = \rho_{\text{ext}}(\mathbf{x}, t), \quad (\text{Gauss' law}) \quad (2.3)$$

$$\nabla \cdot \mathbf{B}(\mathbf{x}, t) = 0, \quad (\text{Gauss' law for magnetism}) \quad (2.4)$$

$$\nabla \times \mathbf{E}(\mathbf{x}, t) = -\frac{\partial \mathbf{B}(\mathbf{x}, t)}{\partial t}, \quad (\text{Faraday's law of induction}) \quad (2.5)$$

$$\nabla \times \mathbf{H}(\mathbf{x}, t) = \mathbf{J}_{\text{ext}}(\mathbf{x}, t) + \frac{\partial \mathbf{D}(\mathbf{x}, t)}{\partial t}. \quad (\text{Ampère's circuital law}) \quad (2.6)$$

This formulation of Maxwell's equations represents a macroscopic average over the microscopic fields. The microscopic response of matter, caused by the fundamental interactions between charged particles in matter and the electromagnetic fields, is averaged macroscopically. The resulting interrelations are given in the material equa-

tions also known as constitutive relations. The general time-dependent formulation of the constitutive relations is complex. In this work, solely problems in steady state with harmonic excitation are investigated where the electromagnetic field is of harmonic time-dependence that is $\mathbf{E}(\mathbf{x}, t) = \text{Re}(\mathbf{E}(\omega, t)e^{-i\omega t})$ and accordingly for \mathbf{H} , \mathbf{D} , \mathbf{B} , \mathbf{J}_{ext} and ρ_{ext} . In the case of isotropic materials with a linear response to the external fields, the constitutive relations can be written as:

$$\mathbf{D}(\mathbf{x}, \omega) = \epsilon_0 \epsilon(\mathbf{x}, \omega) \mathbf{E}(\mathbf{x}, \omega), \quad (2.7)$$

$$\mathbf{B}(\mathbf{x}, \omega) = \mu_0 \mu(\mathbf{x}, \omega) \mathbf{H}(\mathbf{x}, \omega), \quad (2.8)$$

$$\mathbf{J}_{\text{ext}}(\mathbf{x}, \omega) = \sigma(\mathbf{x}, \omega) \mathbf{E}(\mathbf{x}, \omega). \quad (2.9)$$

The dielectric constant ($\epsilon(\mathbf{x}, \omega)$), the relative permeability ($\mu(\mathbf{x}, \omega)$) and the conductivity ($\sigma(\mathbf{x}, \omega)$) describe the macroscopic optical, magnetic and electrical properties of the material. The vacuum permittivity (ϵ_0) and vacuum permeability (μ_0) are universal constant. Via a Fourier transformation, the dielectric constant and the conductivity are linked by $\epsilon(\mathbf{x}, \omega) = 1 + i\sigma(\mathbf{x}, \omega)/(\epsilon_0\omega)$. $\epsilon(\mathbf{x}, \omega)$ and $\mu(\mathbf{x}, \omega)$ are fundamental material properties which can be either derived from first principle calculations of solid state theory or taken from experiments. In this work, experimental data is applied to specify the dielectric constant of the materials under study (see Appendix A). Instead of $\epsilon(\mathbf{x}, \omega)$, in optics conventionally the complex refractive index $\tilde{n}(\omega) = n(\omega) + i\kappa(\omega) = \sqrt{\epsilon(\omega)}$ is used. Often, the real part of the complex refractive index ($n(\omega)$) is simply called the refractive index and the imaginary part of the complex refractive index ($\kappa(\omega)$) is called extinction coefficient. Furthermore, in a good approximation $\mu(\mathbf{x}, \omega) \approx 1$ for electromagnetic problems as the variation in $\epsilon(\mathbf{x}, \omega)$ is dominant.

Helmholtz Equations and Electromagnetic Waves In the absence of free charges and currents the constitutive relations and Maxwell's equations can be reformulated in a simplified form called *Helmholtz equations*:

$$\nabla \times \nabla \times \mathbf{E}(\mathbf{x}, \omega) = -\mu_0 \mu(\mathbf{x}, \omega) \epsilon_0 \epsilon(\mathbf{x}, \omega) \frac{\partial^2 \mathbf{E}(\mathbf{x}, \omega)}{\partial t^2}, \quad (2.10)$$

$$\nabla \times \nabla \times \mathbf{H}(\mathbf{x}, \omega) = -\mu_0 \mu(\mathbf{x}, \omega) \epsilon_0 \epsilon(\mathbf{x}, \omega) \frac{\partial^2 \mathbf{H}(\mathbf{x}, \omega)}{\partial t^2}. \quad (2.11)$$

The general time harmonic solution of the Helmholtz equations can be expressed as a superposition of plain electromagnetic waves of various angular frequencies which

are given by:

$$\mathbf{E}_\omega(\mathbf{x}, t) = \mathbf{E}_0 e^{i(\mathbf{k}\mathbf{x} - \omega t)} \quad \text{and} \quad \mathbf{B}_\omega(\mathbf{x}, t) = \mathbf{B}_0 e^{i(\mathbf{k}\mathbf{x} - \omega t)}, \quad (2.12)$$

where the direction of the electromagnetic waves is given by the wavevector (\mathbf{k}) with $|\mathbf{k}| = \omega|\tilde{n}|/c$. The local speed of light in a certain material is given by $c_0/|\tilde{n}|$, where c_0 is the speed of light in the vacuum.

2.2.2 Optics and Photonics

This section introduces relevant basic concepts, terms and definitions in the field of optics which are essential to follow this work.

Geometrical Optics and Wave Optics Geometrical optics only applies if the wavelength of the considered electromagnetic wave is very small in comparison with any geometrical dimension of the system under study. In such systems, the propagation of light can be studied in terms of light rays. For these light rays, the refraction, reflection and transmission at the interface between two media of different refractive indices is described by Fresnel's equations [78]. From these equations, basic optical formulas like Snell's law of refraction and the condition of total internal reflection can be derived. Also, the attenuation of the intensity of light, given by the Lambert-Beer law, can be studied with geometrical optics. Prominent fields of application are crystalline silicon solar cells with a silicon absorber layer thickness above 150 μm . However, in thin-film solar cells, the light-trapping textures as well as the layer thicknesses are in the range of the wavelength of light in the $a\text{-Si:H}$ and $\mu\text{c-Si:H}$ absorber layers. Thus, geometrical optics provide a very limited picture when studying the propagation of light within a thin-film silicon solar cell. However, for some arguments and discussions presented in this work, geometrical optics is used as it is intuitive and encompassed by wave optics.

In wave optics, the propagation of light is described by electromagnetic waves which are solutions of the Helmholtz equations. These electromagnetic waves exhibit a time-harmonic dependence and a wavelength (λ). Wave optics encompass the field of geometrical optics but can, additionally, explain the interaction of light with objects of dimensions close to the wavelength of light. Prominent phenomena which are explained by wave optics are the interference of electromagnetic waves or the diffraction of light at a grating.

Nearfield and Farfield The nearfield and the farfield denote two regions of conceptually different characteristics of the electromagnetic fields induced by any object which interacts with electromagnetic waves [79, 80]. In particular, for objects of dimensions in the order of the wavelength and below, both types of electromagnetic fields are present. The fundamental reason for these two characteristics is that those electric fields which are induced by changes in charge distribution of the object exhibit a much different character than those electric fields induced by changing magnetic fields (c.f. Eq. (2.3) and Eq. (2.5), respectively). The nearfield consists of those electromagnetic fields which are associated with an immediate electromagnetic response to local changes in the charge distribution in the object. It can induce strong amplitudes of the electromagnetic fields in the vicinity of the object [80]. The farfield dominates at larger distances from the object. At this distance, the electromagnetic fields are radiative and can be expressed as a superposition of propagating electromagnetic waves.

The boundary between the nearfield region and farfield region is vague and its definition varies between different fields of application [81]. Furthermore, there is a broad transition region, wherein nearfields and farfields coexist. For an antenna shorter than half the size of the investigated wavelength, the propagating electromagnetic fields, belonging to the farfield region, dominate for distances larger than twice the wavelength. For distances smaller than the wavelength, the electromagnetic fields associated with the nearfield typically dominate.

In thin-film solar cells, both new light-trapping concepts as well the state-of-the-art light-trapping concept make use of surface textures of dimensions below the wavelength of light in $\mu\text{c-Si:H}$ or $a\text{-Si:H}$. Thus, the electromagnetic nearfield and farfield need to be considered when investigating optics in thin-film silicon solar cells.

Evanescent Electromagnetic Fields Evanescent fields are formed when light waves are reflected totally at the interface of two materials. Total internal reflection is an optical phenomenon that appears if an electromagnetic wave impinges on a planar boundary of two materials at an angle larger than a particular critical angle. If the refractive index of the first material (n_1) is larger than the refractive index of the second material (n_2), the critical angle (θ_c) for total internal reflection is given by:

$$\theta_c = \arcsin \frac{n_2}{n_1}. \quad \text{for} \quad n_1 > n_2. \quad (2.13)$$

In the case of total internal reflection, evanescent fields extend into the material of low refractive index. The evanescent fields decay exponentially and their time-averaged

Poynting vector, which describes the energy flows across the boundary, vanishes. With regard to thin-film silicon solar cells, the existence of evanescent fields above the front interface of the solar cells indicates the total internal reflection of light within the solar cell absorber layers, which is associated with light trapping. With a scanning near field microscope these evanescent fields can be detected allowing for a unique experimental analysis of light propagating in thin-film silicon solar cells [82, 83].

Optical Diffraction Gratings Optical diffraction gratings are dispersive devices which redirect incident light into discrete diffraction orders. The integral parts are periodically arranged elements which transmit, reflect and/or scatter an incident electromagnetic wave. Due to the periodic arrangement, the phase-correlation of the transmitted, reflected and/or scattered electromagnetic wave at all periodic elements is preserved. For certain angles, called diffraction order, the transmitted, reflected and/or scattered electromagnetic wave superimposes constructively. Thus, incident light is redirected into these diffraction orders. The diffraction orders are numbered for each dimension, starting with the zero- order which denotes specular reflection or transmission. The diffraction angles of the diffraction orders are given by the grating equation. They depend on the incident angle, the refractive index, the period, the unit cell, the wavelengths and the diffraction order. In this work, two-dimensional reflection gratings are of particular interest. The corresponding grating equation is given in Section 5.3.

Optical Planar Waveguide An optical waveguide is a structure that guides electromagnetic waves. In a waveguide, propagating electromagnetic waves are confined in a dielectric material by total reflection at the outer boundaries. For this purpose, the adjacent materials must be either highly reflective or of lower refractive index than the inner material. Figure 2.5 shows a planar waveguide which consists of a dielectric layer ($n > 1$) in between a highly reflective mirror at the lower side and air at the top side. Light which propagates at large angles within the waveguide is completely reflected at the highly reflective rear side and the front side due to total internal reflection. For certain angles, the electromagnetic wave that is twice reflected reproduces itself. Eventually, in this condition, any multiply reflected electromagnetic wave reproduces itself, leading to a periodic electric field pattern of regions of multiple constructive interference and destructive interference.

As this self-reproducibility of the electromagnetic wave cannot be fulfilled at any angle, the number of waveguide modes for a certain waveguide of finite thickness is

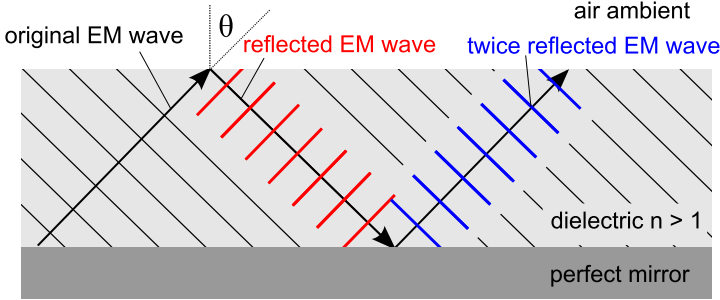


Figure 2.5: Illustration of the condition of self-consistency for the occurrence of waveguide modes. The exemplary system under study is a high refractive index dielectric ($n > 1$) which exhibits a highly reflective mirror at the rear side and an air ambient.

discrete. In explicite, the following condition must be satisfied:

$$\frac{2\pi}{\lambda} \cdot n \cdot 2d \cos(\theta) + \varphi_r + \pi = 2\pi m \quad \text{with} \quad m = 0, 1, 2, \dots, \quad (2.14)$$

where d is the thickness and n is the complex refractive index of the dielectric (see Figure 2.5). φ_r is the phase shift of the reflected electromagnetic wave at the interface between the dielectric and air. This phase shift is dependent on the angle θ and the polarization. For this reason, the dispersion relation of transversal electric (TE) and transversal magnetic (TM) waveguide modes differs.

The above described waveguide modes are confined to the dielectric waveguide. No coupling to propagating electromagnetic waves in the ambient is possible. In order to allow incident light to couple into the waveguide mode, the planar geometry needs to be perturbed, for example, by a grating coupler. In this case, incident light can couple to the waveguide mode and vice versa. The resulting mode is called a leaky waveguide mode.

2.3 Plasmonics

A plasmon is a quantized collective oscillation of the free electron gas density [84–86]. Under certain conditions, these oscillations can couple to an electromagnetic wave. In the case of coupling, the electric field of an incident electromagnetic wave

causes a displacement of the free electron gas density with respect to the ion lattice. Charged regions are induced in phase with the exciting electromagnetic fields. The resulting Coulomb interaction provides a restoring force which causes an oscillation of the free electron gas density. Depending on the boundary conditions, the spatial oscillation of the free electron gas density and in turn the resonance conditions differ. At planar metal surfaces, propagating surface plasmon polaritons (SPP) appear and at the surface of metal nanostructures, localized surface plasmon polaritons (LSP) are formed. In the field of nanophotonics, due to the possible coupling to electromagnetic waves, plasmonic effects are extensively studied to guide and localize light with metal nanostructures within dielectric layer stacks [22, 87]. This section provides a brief introduction. For a thorough understanding the interested reader is directed to the references [84–86].

2.3.1 Propagating Surface Plasmon Polaritons

Surface plasmon polaritons are electromagnetic modes which propagate along an interface of a metal and a dielectric (see Figure 2.6 (a)). They consist of an oscillation of the free electron gas density in the metal and an electromagnetic wave which are coupled in phase to each other. The former aspect reflects the plasmonic character of the SPP and the latter aspect reflects the polaritonic character of the SPP modes. The SPP resonances are eigenmodes and the electric field (see Eq. (2.15)) as well as the dispersion relation (see Eq. (2.16)) can be derived from Maxwell's equations (see Eq. (2.3)-Eq. (2.6)) under consideration of the continuity equations at the interface of the metal and the dielectric [85, 86]:

$$\mathbf{E}(\mathbf{x}, t) = \mathbf{E}_\perp(\mathbf{x}_\perp) e^{i(\mathbf{k}_\parallel \mathbf{x}_\parallel - \omega t)}, \quad (2.15)$$

$$k_\parallel = \frac{\omega}{c} \cdot \sqrt{\frac{\epsilon_m(\omega) \epsilon_D(\omega)}{\epsilon_m(\omega) + \epsilon_D(\omega)}}, \quad (2.16)$$

where ϵ_D and ϵ_m denote the dielectric function of the dielectric and the metal, respectively. The electric field of the SPP mode represents a propagating electrodynamic eigenmode where \mathbf{E}_\perp describes an exponential decay of the electric field perpendicular to the interface into the dielectric as well as into the metal. \mathbf{E}_\perp decays to $1/e$ within approximately 10 nm and 100 nm for noble metals and the dielectric media, respectively [88, 89]. The SPP mode propagates along the metal/dielectric interface

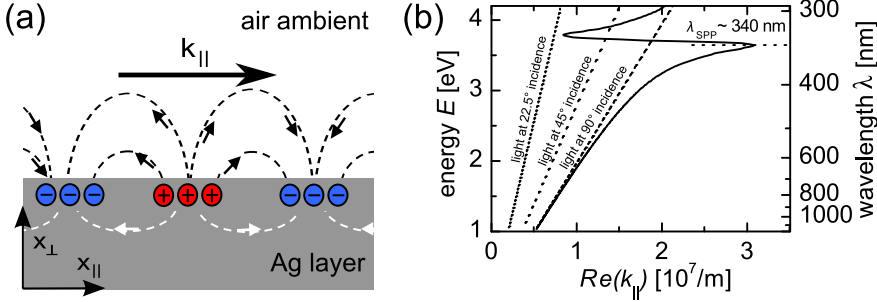


Figure 2.6: (a) Illustration of a propagating SPP at an interface between a planar Ag layer and air. (b) Dispersion relation of the SPP modes at a flat Ag surface in air calculated with Eq. (2.16).

with the wavevector $k_{||}$. For Ag surfaces, propagation lengths on the order of tenths of micrometres have been reported for wavelengths in the visible spectrum [89].

SPP Resonance In Figure 2.6 (b), the dispersion relation of the SPP eigenmodes at an interface of Ag and air, calculated according to Eq. (2.16), is shown. The optical constants for Ag are taken from Appendix A. At the frequency ω_{SPP} , the corresponding λ_{SPP} is marked in Figure 2.6 (b), the density of states per energy increases strongly. In fact, in the case of a perfect conductor ($\text{Im}(\epsilon_m)=0$) and no losses in the dielectric ($\text{Im}(\epsilon_D)=0$) at ω_{SPP} the density of states per energy interval approaches infinity and $\epsilon_{Ag}(\omega) + \epsilon_{air}(\omega) = 0$ is fulfilled. Due to the increased number of states per energy interval at ω_{SPP} , the excitation probability of SPP eigenmodes at that energy is dominant in comparison with other frequencies. In this work, we refer to ω_{SPP} as the resonance frequency of the propagating SPP modes at a particular metal/dielectric interface. λ_{SPP} is the corresponding wavelength.

Coupling of SPP Modes to Incident Light In addition to the dispersion relation of the SPP modes, in Figure 2.6 (b), the dispersion relation of light at 25° incidence, 45° incidence and in the limit of parallel incidence (90°) to the interface are shown. It is shown that the dispersion relations of incident light of low angle of incidence does not intersect with the dispersion relation of the SPP modes. This observation is valid for all dielectrics [85]. Therefore, SPP modes cannot be excited at a perfectly flat metal interface. In order to couple to incident electromagnetic waves, special techniques are required to provide the missing momentum at a specific frequency. The

most common optical methods for the coupling of incident electromagnetic waves to propagating SPP modes are prism couplers, grating couplers and the near-field effects in the vicinity of sub-wavelength nanostructures [85, 86, 88]:

- *Prism couplers*: For this technique, the light impinges on an additional dielectric/air interface above the metal surface, typically via a prism, and is totally internally reflected. If the metal surface is positioned close enough to the dielectric/air interface, such that the evanescent wave can couple to the metal surface, SPP modes on the metal surface can be excited.
- *Grating couplers*: Due to the diffraction of light at the periodically structured metal surfaces, the wavevector of the SPP modes parallel to the grating vector is varied by $\Delta k_{||} = n \cdot 2\pi/l$ where l is the lattice constant of the grating and $n \in \mathbb{N}$. As a result, in the first Brillouin zone, the momentum of the SPP modes and the incident electromagnetic wave intersect which corresponds to a conservation of momentum. Therefore, the SPP modes can couple to incident light.
- *Near-field effects*: In the vicinity of sub-wavelength nanostructures, such as metal nanostructures and scanning nearfield optical microscopy tips, the scattered light cannot be described by single propagating electromagnetic waves. Instead, the local nearfields exhibit all wavevectors and, thus, allow a coupling to SPP modes. Interestingly, near-field optical techniques allow the local excitation of SPP modes and can act as a point source for SPP modes [88, 90].

In this work, the latter two concepts of coupling light to SPP modes are of particular interest as they are relevant for randomly nanotextured surfaces of Ag back contacts in thin-film silicon solar cells [84]. Randomly textured Ag interfaces can be described, on the one hand, as a stochastic distribution of local sub-wavelength nanostructures. On the other hand, randomly textured interfaces can be described as a superposition of periodic gratings of various reciprocal lattice constants.

2.3.2 Localized Surface Plasmon Polaritons

Localized surface plasmon polaritons describe resonant oscillations of the free electron gas density in a nanostructure. Similar to SPP modes, the oscillation of the electron gas density is in phase with oscillating electromagnetic fields (see Figure 2.7 (a)).

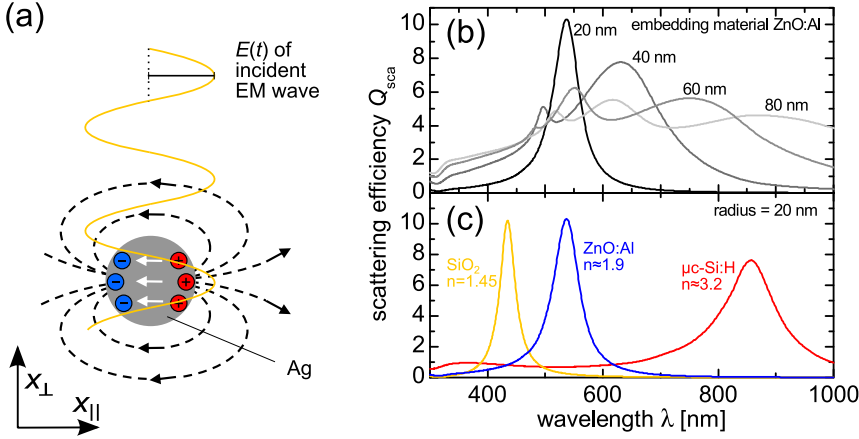


Figure 2.7: (a) Illustration of the oscillation of the electron gas density in a spherical Ag nanoparticle corresponding to a dipolar LSPR resonance. (b) Calculated scattering efficiency (Q_{sca}) of spherical Ag nanoparticles embedded in non-absorbing ZnO:Al of various radii. (c) Calculated Q_{sca} of spherical Ag nanoparticles of 20 nm radius embedded in non-absorbing SiO₂, ZnO:Al and $\mu\text{c-Si:H}$ with refractive index n at the resonance wavelengths of approximately 1.45, 1.9 and 3.2, respectively.

The spatial confinement of the oscillation of the electron gas density affects the resonance condition as well as the coupling to electromagnetic waves. In contrast to SPP resonances, LSPR resonances can be excited by incident light of arbitrary incident angle [84]. For this reason, LSPR resonances in metal nanostructures induce an optical response that differs significantly from that of planar metal interfaces. The rich spectroscopic behavior of metal nanoparticles has raised tremendous interest in their application in nanooptical devices [90,91].

The optical response of a single metallic nanostructure is usually described by the scattering efficiency (Q_{sca}) and the absorption efficiency (Q_{abs}). These dimensionless quantities are calculated by:

$$Q_{\text{abs}} = \frac{P_{\text{abs}}}{I_0 \cdot A_{\text{NP}}} \quad \text{and} \quad Q_{\text{sca}} = \frac{P_{\text{sca}}}{P_0 \cdot A_{\text{NP}}}, \quad (2.17)$$

where I_0 is the intensity of the incident electromagnetic wave, A_{NP} is the cross-section of the nanoparticle normal to the propagation direction of the incident elec-

tromagnetic wave. P_{abs} and P_{sca} are the powers absorbed and scattered by the nanoparticle, respectively.

Mie Theory For spherical nanoparticles which are embedded in non-absorbing materials, an exact solution of the interaction between incident light and the nanoparticle was first described by Gustav Mie [92]. Applying spherical coordinates and multipole expansions of the irradiated electric and magnetic fields, a complete expression was derived for the electrodynamic response of spherical nanoparticles to a plane incident electromagnetic wave. In the derivation, Maxwell's equations are solved rigorously. Thus, the Mie theory is universal to all wavelengths of incident light, sizes of the nanoparticle, non-absorbing embedding materials and materials of the nanostructure. In several experimental studies, the validity of Mie theory, within the above described limitations, has been verified [91, 93, 94]. Furthermore, numerous expansions of the Mie theory are presented for other geometries in the literature such as other shapes of nanoparticles or interactions of multiple nanoparticles [84]. A thorough description and derivation of the Mie theory is given by [95]. In this work, the Mie theory serves as an analytical reference to evaluate the accuracy of the three-dimensional electromagnetic simulations of metallic nanostructures. The Mie theory was calculated with the program code published in [95].

Factors Influencing LSPP Resonances Several factors influence the spectral position and damping of LSPP resonances in noble metal nanostructures. The most relevant factors for this work are described in the following.

- *Size of the nanostructure:* For metallic nanostructures of small size compared with the wavelength of the incident electromagnetic wave, the phase of the latter can be approximated to be constant over the total volume of the nanostructure. Then, the problem under study can be simplified in an electrostatic field which, in turn, yields a dipolar LSPP resonances in spherical nanoparticles. The resonance frequency of this dipolar LSPP resonance can be approximated in the quasi-static approximation. With increasing size of the nanostructure, the spatial variation of the phase extends over the volume of the nanostructure. This is equivalent to a retardation of the electromagnetic fields inside the particle. Deviations from the quasi-static dipolar LSPP resonance arise: the dipolar LSPP resonance shifts to longer wavelengths and the widths of the resonance increases due to radiation damping. In addition, in large nanoparticles, higher multipole modes can be excited by incident electromagnetic waves. These multipolar resonances appear as additional resonances in the

Q_{abs} and Q_{sca} of the nanostructure. In Figure 2.7 (b), the size-dependent spectral response of a spherical Ag nanoparticle embedded in ZnO:Al is shown.

- *Shape of the nanostructure:* In addition to the size of the nanostructure, the shape of the nanostructure influences the oscillation of the electron gas density. Thus, the LSPP resonances depend strongly on the shape of the nanostructure. A nice experimental illustration of the impact of the outer shape of a nanoparticle on the LSPP resonances is given by Mock et al. [96]. For oblate ellipsoidal nanoparticles, two LSPP modes appear due to two differently sized axes. These modes can be excited independently by an electromagnetic wave which is polarized along the respective axis [91]. In addition to a variation of the outer shape of the nanostructure, core-shell metal nanoparticles and nanorings allow additional ways to manipulate the LSPP resonances [97, 98].
- *Embedding material:* A LSPP resonance induces strongly enhanced electric fields in the surroundings of the nanostructure. As a consequence, the embedding dielectric close to the nanostructure is polarized. Charged regions appear in the dielectric which screen the electric field of the LSPP resonance inside the nanoparticle. As a result, the polarizability of the embedding dielectric increases the LSPP resonance wavelength [84]. Therefore, the LSPP resonance wavelength increases with increasing refractive index of the embedding material. This effect is shown for spherical Ag nanoparticles in Figure 2.7 (c). For inhomogeneous embedding materials, such as nanostructures embedded in a dielectric layer stack or nanostructures on substrates, the impact of the embedding medium on the LSPP resonance is much more complex [99].
- *Interaction of LSPP resonances of multiple nanostructures:* If two or more metallic nanostructures are located adjacent to each other, the LSPP-induced enhanced electric fields enable a coupling. This results in a strong change of the LSPP resonances [91, 98]. In fact, for well-defined systems such as dimers of Ag nanoparticles, a hybridization of LSPP resonances has been observed [100–102]. For very complex arrangements of nanostructures of various shapes, the interaction of multiple LSPP resonances induces 'hot-spots' of highly enhanced electric fields. These hot-spots are essential in surface enhanced Raman spectroscopy [103, 104].

2.4 Optical Simulations

There are several numerical methods to simulate the propagation of light in condensed matter. For solar cell applications, the adequate choice of method depends mostly on the spatial dimensions of the textures and structures under study. For very large dimensions of these textures in comparison with the local wavelength, the raytracing method is sufficiently accurate and precise [105]. For textures or layer thicknesses of geometrical dimensions close to or below the considered wavelength, Maxwell's equations have to be solved rigorously to accurately simulate the propagation of light in the solar cell. For three-dimensional devices, the finite difference time-domain method [106], the finite element method (FEM) [107–109], the Fourier modal method [110] or the finite integration technique [111] are commonly applied. By using these techniques, the influence of the textured interfaces on the light trapping has been successfully investigated for thin-film silicon solar cells [112–116] as well as other types of solar cells [117–119].

In this work, the interaction of electromagnetic waves with nanostructured plasmonic Ag back contacts is studied with a three-dimensional electromagnetic solver of Maxwell's equations based on the FEM method. For the accurate simulation of plasmonic effects, the FEM methods holds particular advantages as it allows the application of an adaptive mesh of triangular or prismatic shape. Such meshes are essential on the curved metal/dielectric interface, where strong electric field enhancements appear [98, 120, 121]. The simulations were carried out with the commercially available program JCMSuite (JCMWave GmbH, Berlin, Germany) [122, 123].

2.4.1 Finite Element Method for Maxwell's Equations

JCMSuite solves numerically Maxwell's equations in the stationary case with the finite element method.

Maxwell's Equations in the Stationary Case In the stationary case, the time-dependent behavior of the electromagnetic fields can be separated from the spatial behavior by using a time-harmonic ansatz:

$$\mathbf{E}(\mathbf{x}, t) = \text{Re}(\tilde{\mathbf{E}}(\mathbf{x}, \omega)e^{-i\omega t}) \quad \text{and} \quad \mathbf{H}(\mathbf{x}, t) = \text{Re}(\tilde{\mathbf{H}}(\mathbf{x}, \omega)e^{-i\omega t}). \quad (2.18)$$

Maxwell's equations in combination with the constitutive relations can be rewritten and split into two separate sets of second order differential equations for the electric

field and the magnetic field, respectively. Furthermore, in the time-harmonic ansatz, the magnetic field can be simply derived from the electric field via the relation $i\omega\epsilon_0\epsilon(\mathbf{x},\omega)\tilde{\mathbf{E}}(\mathbf{x},\omega) = \nabla \times \tilde{\mathbf{H}}(\mathbf{x},\omega)$. Thus, in the time-harmonic ansatz, Maxwell's equations can be condensed into the following two second order partial differential equations for the electric field [123, 124]:

$$\nabla \times (\mu_0\mu(\mathbf{x},\omega))^{-1}\nabla \times \tilde{\mathbf{E}}(\mathbf{x},\omega) - \omega^2\epsilon_0\epsilon(\mathbf{x},\omega)\tilde{\mathbf{E}}(\mathbf{x},\omega) = -i\omega\tilde{\mathbf{J}}(\mathbf{x},\omega), \quad (2.19)$$

$$\nabla \cdot \epsilon_0\epsilon(\mathbf{x},\omega)\tilde{\mathbf{E}}(\mathbf{x},\omega) = 0. \quad (2.20)$$

Finite Element Method The FEM method provides a general approach to solve numerically a set of partial differential equations such as Eq. (2.19) and Eq. (2.20) with the given boundary conditions [108]. It applies a variational formulation to solve Eq. (2.19) and Eq. (2.20). A complete description is beyond the scope of this thesis. Nevertheless, the integral steps shall be summarized: First, an appropriate test function, typically a polynomial, is multiplied to the partial differential equation (see Eq. (2.19)), which is integrated over the total simulation domain. Then, by applying a partial integration, the variational formulation of the problem is obtained. In this formulation, a discretization of the simulation domain into a mesh of finite elements is introduced. This discretization allows the original problem to be represented by a large but finite dimensional linear problem whose numerical solution approximates the solution of the original problem. Furthermore, this solution converges numerically stably towards the exact solution by either increasing the number of mesh points used for the discretization of the calculation domain or by increasing the polynomial order of the test function. However, both numbers are proportional to the dimension of the linear problem, which determines the random access memory consumption of a computational treatment.

2.4.2 Optical Simulations with JCMsuite

In this work, three-dimensional electromagnetic simulations of thin-film silicon solar cells as well as plasmonic nanostructures have been conducted. The simulations were conducted with the software JCMsuite which applies the FEM method. In this section, a brief description of the practical procedure of these simulations is given.

Setup of the Problem First, the geometry of the solar cell and the simulation domain must be assigned. To provide an example, the calculation domain of a typ-

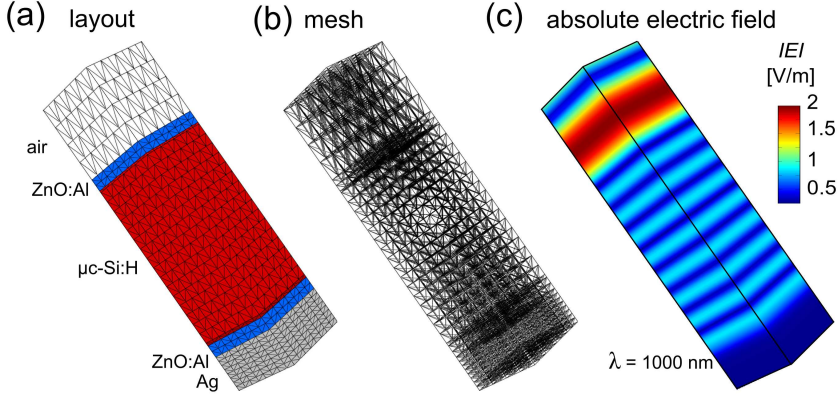


Figure 2.8: (a) Calculation domain and (b) the three-dimensional mesh of a typical flat $\mu\text{c-Si:H}$ thin-film solar cell in n-i-p configuration. (c) The absolute electric field is shown for an incident plane electromagnetic wave with a wavelength of 1000 nm.

ical flat $\mu\text{c-Si:H}$ thin-film solar cell in n-i-p configuration is shown in Figure 2.8 (a). For each material specified in the geometrical setup, the complex refractive index needs to be specified (see Appendix A). To study the interaction of incident light with the sample structure, a planar electromagnetic wave is specified which penetrates the geometry under study. If not explicitly mentioned, the planar electromagnetic wave impinges at normal angle of incidence. The boundaries orthogonal to this incidence are assumed to be either periodic boundaries or open boundaries. In the latter case, perfectly matched layers are introduced at the boundary of the calculation domain, which create non-reflecting interfaces [125].

A prismatic mesh is generated to discretize the three-dimensional space (see Figure 2.8). For non-periodic geometries of cylindrical symmetry, JCMsuite provides a particular setting of the FEM method which solves, under consideration of the cylindrical symmetry, the problem in two dimensions [123]. Due to the highly reduced computational time and reduced consumption of random access memory, this two-dimensional cylindrical FEM method is applied whenever applicable. For any geometry, JCMsuite can generate a mesh with predefined upper limits for the maximal side length of the mesh cells. The mesh and the polynomial order of the test function are the most critical figures for the accuracy of the FEM method. By applying convergence studies, these quantities have been optimized successively for each geometry in terms of accuracy as well as computational time and consumption of random

access memory. The latter was limited to 64 Gigabyte for the computers used in this work. A maximal relative error of 2% of the targeted physical quantities, such as the absorptance or the reflectance, was accepted. This was commonly achieved for polynomial order of the test function larger than or equal to three. For dielectric material, the maximal side length of any mesh cell was set to be 10% of the wavelength of the incident electromagnetic wave. For the interface of planar layers and within Ag nanostructures, a much denser mesh was required. As a rule of thumb, in Ag nanostructures, the maximal side length of the mesh cells was set to the minimum of 10% of the wavelength and 25% of the dimension of the nanostructure.

Post Processing The above described FEM method numerically solves Eq. (2.19) and Eq. (2.20) on the three-dimensional mesh, which yields a three-dimensional complex electric field. In Figure 2.8 (c), the absolute electric field at a wavelength of 1000 nm is shown. Within the post processing, physical quantities are derived from the three-dimensional complex electric field.

- *Absorptance:* A very important quantity throughout this work is the absorptance (A_V) of a subdomain of volume (V) of the calculation domain such as a specific layer or object of the solar cell. It is calculated as a ratio of the power absorbed (P_{abs}) to the total power (P_{tot}) which is irradiated on the calculation domain by the plane wave:

$$A_V = \frac{P_{\text{abs}}}{P_{\text{tot}}}. \quad (2.21)$$

For time-harmonic electromagnetic fields P_{tot} and P_{abs} are given by [76]:

$$P_{\text{tot}} = \sqrt{\frac{\epsilon_0 \epsilon_{\text{BG}}}{\mu_0}} \cdot |\mathbf{E}_0|^2, \quad (2.22)$$

$$P_{\text{abs}} = 4\omega \int_V \text{Im}(\omega_e) dV \quad \text{and} \quad \omega_e = \frac{(\epsilon_0 \epsilon \tilde{\mathbf{E}})^* \cdot \tilde{\mathbf{E}}}{4}, \quad (2.23)$$

where ϵ_{BG} is the dielectric constant of the background material, which is usually air, $\omega_e(\mathbf{x})$ is the local electrical field energy density and \mathbf{E}_0 is the vector of the electric field of the incident electromagnetic wave.

- *Scattering angle distribution, reflection and transmission:* The derivation of the angular scattering intensity distribution, the transmission and reflection de-

depends on the applied boundary conditions. For periodic boundaries, which are applied for the simulation of solar cells and plasmonic reflection gratings, a Fourier transform is conducted on the complex electric field on the flat boundaries at the top or bottom of the calculation domain [123]. This Fourier transform gives the wavevectors of the evanescent as well as propagating Fourier modes. By evaluating the direction of the propagating Fourier modes, which correspond to propagating electromagnetic waves, detailed angular scattering distributions as well as the total and the diffuse reflection can be calculated.

In the case of open boundaries at the calculation domains, a farfield expansion of the electric fields at the boundaries of the calculation domain is conducted [123]. This allows the farfield vectors to be evaluated which gives the scattering intensity into a certain direction.

- *External quantum efficiency:* For a given charge carrier collection efficiency, the *EQE* of a simulated thin-film silicon solar cell can be calculated by multiplying this collection efficiency and the absorptance of the silicon absorber layers. For the intrinsic absorber layer, it is commonly assumed that the charge carrier collection efficiency is 100%. For the n-doped and p-doped layers, to the knowledge of the author, the charge carrier collection efficiencies should be much smaller. However, exact values are not known. In this work, a good agreement between simulated *EQE* and experimental *EQE* of a $\mu\text{c-Si:H}$ thin-film solar cell in n-i-p configuration was obtained for collection efficiencies of 0%, 100% and 50% in the p-doped, intrinsic and n-doped $\mu\text{c-Si:H}$ layer, respectively (see Chapter 8.2.1). For a given *EQE*, the J_{sc} can be calculated as an integral of the product of the *EQE* and the solar spectrum.

2.4.3 Simulations of Localized Surface Plasmon Polaritons

In this work, numerical studies on plasmonic back contacts in thin-film silicon solar cells have been conducted. The accurate simulation of plasmonic effects in metal nanostructures is numerically challenging and requires a very dense mesh at the metal/dielectric interface [120]. In order to evaluate the accuracy of the applied optical simulations for plasmonic effects, a Ag spherical nanoparticle embedded in non-absorbing ZnO:Al was simulated and compared with an analytical reference, the Mie theory. In Figure 2.9 (b) and Figure 2.9 (c), simulated and analytical values of Q_{abs} and Q_{sca} are shown. For this simulation, the maximal side length of the mesh cells was set to the minimum of 10% of the wavelength and 25% of the dimension of

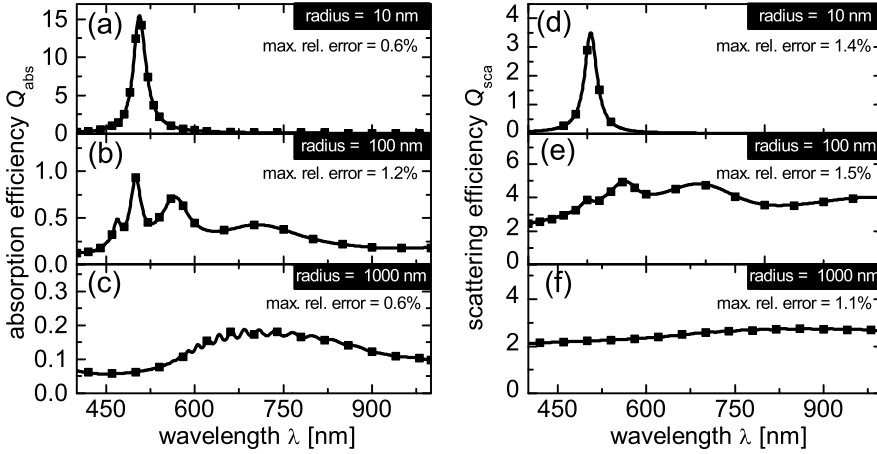


Figure 2.9: Comparison of simulated (filled squares) and analytically derived (black line) scattering efficiency (Q_{sca}) and absorption efficiency (Q_{abs}) of isolated spherical Ag nanoparticles embedded in non-absorbing ZnO:Al.

the nanostructure. For radii ranging over three orders of magnitude from 10 nm to 1000 nm, a very good agreement between the simulated data and the analytical reference is demonstrated. In fact, over the total wavelength spectrum, the relative error of Q_{abs} is below 1.2%. For Q_{sca} , the relative error is larger but still below 1.5%. This result is representative of all other radii of the nanoparticle from 10 nm to 1 μm and of all refractive indices of the embedding material.

Chapter 3

Light Trapping

Light trapping in solar cells is achieved when the absorption of incident light is higher than the absorption of a single light pass through the absorber material. Thus, for optically thin solar cells the light-trapping effect enhances the J_{sc} . Alternatively, light trapping in optically thick solar cells allows the reduction of the absorber material thickness, which reduces the material consumption, enhances the V_{oc} in low mobility solar cells and reduces the requirements on the material such as the stability of a-Si:H with regard to light-induced degradation [29, 126–128]. In consequence, light trapping increases the solar cell efficiencies and reduces the costs of electricity generation with solar cells. In this chapter, fundamental aspects and limits to light trapping in solar cells as well as the state-of-the-art light trapping in silicon solar cells are introduced. In the last section, a review on the emerging field of plasmonic light trapping is presented.

3.1 Fundamentals and Limits

Essential for all research on light trapping is the understanding of the maximum achievable absorption enhancement in solar cells. Initially, the limits to light trapping were studied for optically thick solar cells, typically made of crystalline silicon where the absorber layer is many wavelengths thick. Light trapping in these solar cells is achieved by the scattering of incident light at a textured interface in combination with a highly reflective back contact. Due to internal reflection, the average length

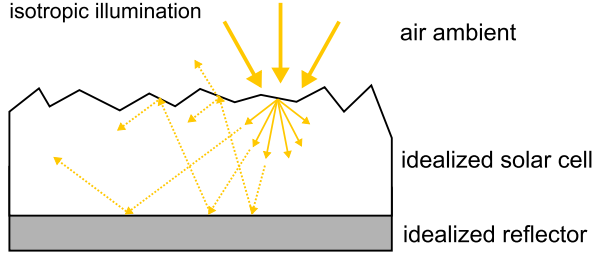


Figure 3.1: Illustration of light trapping in an optically thick idealized solar cell.

of the light path and in turn the absorption in the absorber material is enhanced. A schematic cross-section of a solar cell with a textured front interface is shown in Figure 3.1. In the case of perfect randomization of the scattered light, called Lambertian light scattering, the absorption enhancement can be calculated based on geometrical optics [129, 130].

Lambertian Light Trapping For a single light pass through the absorber layer of a solar cell, the fraction of absorbed light is simply given by the Beer-Lambert law:

$$A(\lambda) = 1 - e^{-\alpha(\lambda)l}, \quad (3.1)$$

where $\alpha(\lambda)$ is the absorption coefficient of the absorber material of the solar cell and l is the length of a single light pass through the solar cell. Assuming a perfect mirror at the back side and a Lambertian scatterer at the front interface, the length of one light path in the absorber material is $l = 2d / \cos(\theta)$, where d is the thickness of the solar cell and θ is the scattering angle. Considering the isotropic distribution of scattering angles induced by the Lambertian scatterer, the absorptance (A_1) for all incoupled and scattered light rays which travel once from the front side through the solar cell and back to the front side is given by [130]:

$$A_1(\alpha d, \lambda) = 1 - \frac{\int e^{-\frac{2\alpha(\lambda)d}{\cos(\theta)}} \cos(\theta) d\Omega}{\int \cos(\theta) d\Omega}. \quad (3.2)$$

An analytical solution of the integral on the right side of Eq. (3.2) can be found in [129]. In order to calculate the overall absorption of a solar cell with Lambertian light trapping, multiple reflections at the front interface need to be considered. If $R_F(\lambda)$ depicts the reflection at the Lambertian scatterer at the front interface, the

total absorptance for the Lambertian light trapping is given by the series:

$$A(\alpha d, \lambda) = \sum_i A_1(\alpha d, \lambda) R_F(\lambda)^{(i)} (1 - A_1(\alpha d, \lambda))^{(i)}, \quad (3.3)$$

$$= \frac{A_1(\alpha d, \lambda)}{1 - (1 - A_1(\alpha d, \lambda)) R_F(\lambda)}. \quad (3.4)$$

Although the Lambertian light trapping in Eq. (3.4) is not a fundamental limit, due to its simple derivation, it often serves in the literature as a reference scenario. In the limit of weak absorption ($\alpha(\lambda) \approx 0$) the Lambertian light trapping fulfills the more fundamental limit for light trapping which was derived by Yablonovitch [131, 132].

Yablonovitch Limit The Yablonovitch limit states that under isotropic illumination, the maximal average length of light path \bar{l}_{\max} at a certain wavelength is given by:

$$\bar{l}_{\max} = 4n^2 d, \quad (3.5)$$

where n is the refractive index of the solar cell absorber material and d is the thickness of the solar cell. A factor $2n^2$ of the maximal light path enhancement comes from the maximal internal reflection of the light in the absorber layer. An additional factor of 2 comes from the reflection at the back contact. The maximal absorptance (A_{\max}), according to the Yablonovitch limit, is then given by $A(\lambda)_{\max} = 4n^2 d \alpha(\lambda)$. Assuming that all absorbed photons in the solar cell induce charge carriers which contribute to the J_{sc} of the solar cell, A_{\max} provides an upper limit for the EQE . A detailed derivation of the Yablonovitch limit can be found in [26, 131, 132]. Here, the assumptions and idealizations of the Yablonovitch limit as well as their implications are discussed:

- *Angular confinement* For the derivation of Eq. (3.5), isotropic illumination of the solar cell is assumed. However, as Yablonovitch already points out in the original manuscript, the angular confinement of the incident light allows the limit presented in Eq. (3.5) to be exceeded. For an angle selective filter, the maximum average light path enhancement changes to $4n^2 d / \sin(\theta_c)^2$, with θ_c being the acceptance angle [133, 134]. Thus, the Yablonovitch limit can be overcome at the cost of a reduced acceptance angle of the solar cell. A detailed analysis on the potential of angular selective filters for silicon solar cells in terms of the annual yield can be found in [135].

- *Optical losses* The solar cell structure considered for the derivation of the Yablonovitch limit exhibits no optical losses, which are certainly present in realistic solar cells. In order to consider these losses, Eq. (3.5) has been developed further for less idealized solar cell structures by Deckman et al. [136]. In their model, optical losses at the front and back contact are considered. As a result, a more realistic limit for the *EQE* can be calculated [54, 136].
- *Limit of weak absorption* The Yablonovitch limit is derived under the assumption of very weak absorption in the absorber layer of the solar cell. This means that the absorption of a single light pass is negligible. In this case, the relevant figure of merit for the absorption is the enhancement factor of the light path rather than the absorption coefficient of the absorber layer. It has been shown in the literature that the factor of maximal average light path enhancement decreases if the single light pass absorption of the absorber layer is relevant [129, 132]. In particular for thin-film silicon solar cells, the assumption of weak absorption is not applicable. To provide an example, the absorption coefficient of $\mu\text{c-Si:H}$ varies from 10^4 cm^{-1} to 10^{-1} cm^{-1} for wavelengths between 600 nm and 1100 nm, while the thickness of $\mu\text{c-Si:H}$ solar cells is typically below 2 μm .
- *Thickness of solar cell absorber* Fundamental for the derivation of Eq. (3.5) is that the thickness of the absorber layer is much larger than the wavelength of incident light. Under this assumption, the propagation of light was studied in terms of geometrical optics. Particularly for thin-film solar cells, this assumption is not valid.
- *Isotropic distribution of propagating light inside the solar cell* Essential for the derivation of the Yablonovitch limit is the statement that light trapping is maximal if the light propagation inside the solar cell device is isotropically distributed. This statement is valid for ergodic systems where the propagation of light inside the solar cell can be approximated in terms of geometrical optics. Misleadingly, the assumed isotropic light distribution inside the solar cell is often put equal to Lambertian light scattering at a randomly textured interface. In fact, the Yablonovitch limit is also applicable to light-trapping concepts which make use of directional selective light scattering such as gratings of periodicity significantly larger than the wavelength of incident light [132, 133, 137].

The last two assumptions are applicable if the wave nature of light can be disregarded. Thus, wave optical effects like diffraction, interferences and local electromagnetic field enhancements are not considered. As a result, the Yablonovitch limit is not applicable if the local wave nature of light becomes relevant. This occurs, for example, in thin-film solar cells or solar cells with diffraction gratings of period below the wavelength of incident light. Especially for thin-film silicon solar cells, understanding the limits to light trapping in solar cells which apply low absorber thicknesses or diffraction gratings is very crucial. Several recent works have studied light trapping in such solar cells numerically as well as experimentally [114, 115, 138–150]. In the recently work of Z. Yu, A. Raman and S. Fan [151, 152], a formalism was developed that allows the maximum light absorption enhancement to be calculated under rigorous consideration of the electromagnetic perspective.

Electromagnetic Limit on Light Trapping by Z. Yu, A. Raman and S. Fan

Yu et al. apply a rigorous electromagnetic leaky mode formalism that allows the maximum absorption enhancement to be calculated for solar cells with wavelength-scale thickness or wavelength-scale gratings. In their formalism, the propagation of light inside the solar cell is represented by leaky waveguide modes. For a certain light-trapping concept, such as a square lattice gratings of period p , these modes couple to propagating waves in the ambient (see Figure 3.2). The case of random texture for light trapping is considered as the limit of the periodic system with a period of the grating which approaches infinity. Similarly to the Yablonovitch limit, their formalism is based upon the assumption of weak absorption in the solar cell, but considers optically thin absorber layers as well as wavelength-scale grating couplers. In the case of low absorption, all light propagation inside the solar cell is described well with leaky waveguide modes. For a single leaky waveguide mode, the spectral absorption can be calculated from the temporal coupled-mode theory [152]. By summing up the maximal absorption of all leaky waveguide modes of the solar cell in the limit of strong coupling of the modes to incident light, Yu et al. derived an upper limit for the absorptance A_{\max} in the solar cell:

$$A_{\max} = \frac{2\pi\gamma_i}{\Delta\omega} \cdot \frac{M}{N}, \quad (3.6)$$

where M is the number of coupling modes in the solar cell and N is the number of plane waves in the ambient of the solar cell that can couple to a certain leaky mode. γ_i is the intrinsic loss rate of the leaky modes, which is considered to be equal for all modes. Equation 3.6 is valid for a frequency range of bandwidth ($\Delta\omega$) which is

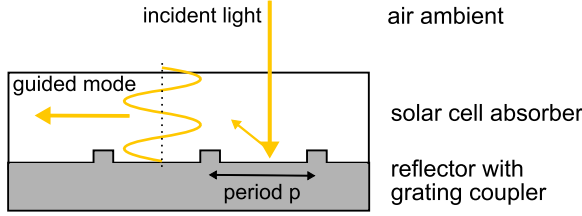


Figure 3.2: Illustration of light trapping in an optically thin solar cell with a period grating on the back contact.

larger than the bandwidth of the single leaky waveguide modes. Due to the broad solar spectrum, this condition is fulfilled for all bulk solar cells and thin-film solar cells.

In conclusion, the formalism developed by Yu et al. allows the maximum possible absorptance to be calculated for a certain solar cell device based on the number of waveguide modes, the absorption rate of the waveguide modes and the number of propagating waves in the ambient which couple to the waveguide modes. Depending on the considered geometry, these figures and their dependencies differ strongly. Thus, A_{\max} differs in bulk solar cells, solar cells with wavelength-scale square lattice gratings and thin solar cells:

- *Solar cells with thicknesses and period of many wavelengths* For solar cells of thickness d and a period p much larger than the local wavelength, the leaky waveguide modes in the solar cell can be approximated by propagating waves. Then, the total number M of leaky modes in a unit cell of the solar cell is simply given by multiplying the local photon density with the volume ($V = p^2 d$). Furthermore, the decay rate of each guided mode is given by $\gamma_i = \alpha c/n$. The number of accessible planar waves in the ambient is determined by the grating-coupling of the guided modes to the planar waves. The resulting maximal absorption enhancement, which is derived from Eq. (3.6), corresponds to the Yablonovitch limit ($A(\lambda)_{\max} = 4n^2 d \alpha(\lambda)$).
- *Solar cells with a wavelength-scale two-dimensional grating* If the periodicity p of the solar cells is comparable to the wavelength, the number of propagating waves which can couple via the grating to a leaky mode is highly discretized, as illustrated in Figure 3.3 (a). The accessible propagating waves in the ambient are shown in the parallel wavevector space k_{\parallel} . Due to the square lattice grat-

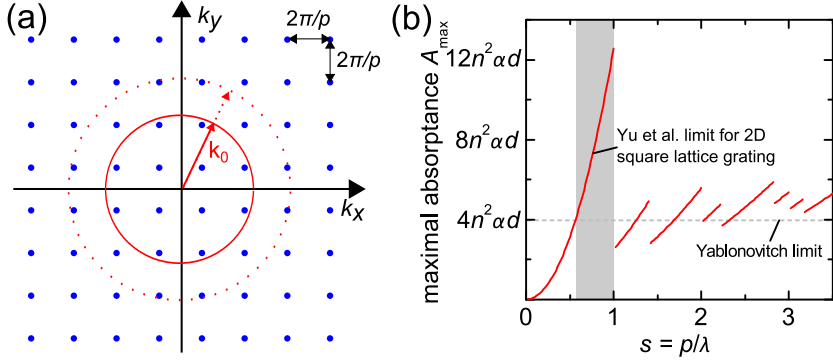


Figure 3.3: Light trapping with two-dimensional grating couplers in optically thick solar cells (a) Propagating waves in the ambient (blue dots) in the two-dimensional $\mathbf{k}_{||}$ space. Propagating waves within the red circle are able to couple to a guided mode of propagation constant $|\mathbf{k}_0|$. (b) Theoretical maximum absorbance (A_{\max}) of the solar cell with two-dimensional gratings of periodicity close to the wavelength [151]. The gray area indicates the wavelength range wherein A_{\max} is larger than the Yablonovitch limit.

ing, the density of accessible propagating planar waves is given by $(p/2\pi)^2$. For those waves where $|\mathbf{k}_{||}| \leq |\mathbf{k}_0| = \omega/c$ is fulfilled, a coupling is possible. For large periods $p \gg \lambda = 2\pi/k$, N can be approximated by multiplying the density of accessible propagating waves and the considered area ($\pi|\mathbf{k}_0|^2$) of the $k_{||}$ space. However, for small p the discretization of the accessible propagation waves in the $\mathbf{k}_{||}$ space becomes relevant. In fact, with decreasing period, the number of accessible propagating waves varies discontinuously and in turn the $A_{\max} \propto 1/N$ varies discontinuously. In Figure 3.3 (b), the maximal absorbance is shown as a function of $s = p/\lambda$ [152]. It is shown that the largest enhancement in A_{\max} , which corresponds to the lowest value in N , is at hand if the period p is slightly smaller than the wavelength ($s < 1$). In this case, the A_{\max} exceeds the Yablonovitch limit significantly by a factor of π and $2\pi/\sqrt{3}$ for a square lattice and a triangular lattice, respectively [152]. Furthermore, as shown in Figure 3.3 (b), for the two-dimensional square lattice grating, there is a broad wavelength range at a fixed period wherein the maximum A_{\max} exceeds the Yablonovitch limit. It shall be noted that these considerations are valid for normal incidence. In fact, the described possible

enhancement of A_{\max} beyond the Yablonovitch limit comes at the cost of a strong angular dependence and cannot outperform the generalized, angular selective Yablonovitch limit [152].

- *Solar cells of wavelength-scale thickness* If the thickness (d) of the solar cells is in the order of the wavelength of incident light, the number of leaky modes which are supported by the solar cell changes discontinuously with d (see Section 2.2.2). In fact, if the thickness d is smaller than half the wavelength a single leaky mode exists [151]. As a result, similar to the case of wavelength-scale periodicity, this discretization allows A_{\max} to be increased beyond the Yablonovitch limit. However, the maximum enhancement depends strongly on the solar cell layer stack and the layer thicknesses required are very small. A detailed derivation is presented by Yu et al. [151].

3.2 State-of-the-Art Light Trapping

The first light-trapping concepts for crystalline silicon solar cells were proposed in the 1970s [153]. Since then, this field of research has raised a strong interest. Initially, the research focused on crystalline silicon solar cells. Today, for state-of-the-art light trapping in crystalline silicon solar cells, inverted or upright pyramids of typical feature size of around 10 μm are induced at the front interface [137, 154]. In mass production of high efficiency crystalline silicon solar cells, upright pyramids are usually prepared by an anisotropic etch of the silicon surfaces. This etching yields square based pyramids which are defined by intersecting crystallographic planes [155]. Inverted pyramids were used in the famous PERL-cell which has yielded up to date the highest efficiency for monocrystalline silicon solar cells of 24.7% under AM1.5 illumination [154, 156]. In this solar cell, light path enhancement factors of up to 40 have been reported, indicating a very good light trapping [156].

State-of-the-Art Light Trapping in Thin-Film Silicon Solar Cells Due to very long process times and a reduction of the light-induced degradation of $a\text{-Si:H}$, in principle, the $a\text{-Si:H}$ and $\mu\text{c-Si:H}$ absorber layers in thin-film silicon solar cells should be as thin as possible [58, 59, 127, 157]. As a consequence, these cells require particularly good light trapping to gain high efficiencies. Qualitatively, this is illustrated in Figure 3.4, where the absorptance is given as a function of the wavelength for a single light pass through an $a\text{-Si:H}$ layer and a $\mu\text{c-Si:H}$ layer of typical thin-film silicon solar cell device thicknesses (250 nm for $a\text{-Si:H}$ and 1.0 μm for $\mu\text{c-Si:H}$) [44].

For both materials below the corresponding band gap, the absorptance is strongly reduced. Despite the afore described limited validity of the Yablonovitch limit for thin-film silicon solar cells, it is used here as a first order approximation to illustrate the significant improvement potential for future thin-film silicon solar cells enabled by applying improved light-trapping concepts. The corresponding maximum short-circuit current density enhancement (ΔJ_{sc}), according to the Yablonovitch limit, is around 10 mA/cm² and 18 mA/cm² for the *a*-Si:H and the μ c-Si:H solar cell, respectively. For light of energy slightly below the band gap (wavelengths of around 1000 nm), a maximum absorptance enhancement factor of 36 is necessary to reach the Yablonovitch limit of the μ c-Si:H solar cell. As shown by Yu et al., when applying wavelength-scale structures for light trapping, one might even increase this potential at the cost of angular selectivity.

The state-of-the-art light trapping in thin-film silicon solar cells makes use of randomly textured front contacts and reflective back contacts, in order to scatter and diffract incident light multiple times within the *a*-Si:H and μ c-Si:H absorber layers. Several types of substrates, materials and processes have been investigated in the past to prepare these random textures on the transparent and conductive front contacts. Prominent examples are wet-chemically etched, sputtered ZnO:Al layers [46–48], as-deposited grown SnO₂ layers [49, 50] or as-deposited grown ZnO:Al layers prepared by low pressure chemical vapor deposition [51]. In this work, wet-chemically etched ZnO:Al front contacts are used for reference state-of-the-art solar cells. These ZnO:Al front contacts are rf-sputtered on a glass substrate. The ZnO:Al layers were wet-chemically etched for around 40 s in 0.5 w/w% HCl [48], which yields a random texture. The resulting surface exhibits a texture of crater-like features of typical lateral dimension of 1-2 μ m and depths of 200-400 nm. The typical root mean square roughness is around 140 nm (see Figure 3.5 (a)) [55].

In order to illustrate the light trapping induced by randomly textured ZnO:Al front contacts in thin-film silicon solar cells, the *EQEs* of μ c-Si:H thin-film solar cells with and without light trapping are compared in Figure 3.5 (b). The state-of-the-art solar cell is deposited on a randomly textured ZnO:Al front contact and applies a highly reflective Ag back contact. The μ c-Si:H solar cell with no light trapping was prepared in the same way but uses a highly absorptive back contact made of a 1 μ m thick n-doped μ c-Si:H layer and a Pt back layer. In the latter solar cell, virtually all light which reaches the rear side of the cell is absorbed after a single pass through the solar cell device. For the solar cell with no light trapping, the *EQE* is significantly reduced for wavelengths between 480 nm and 1100 nm. The corresponding

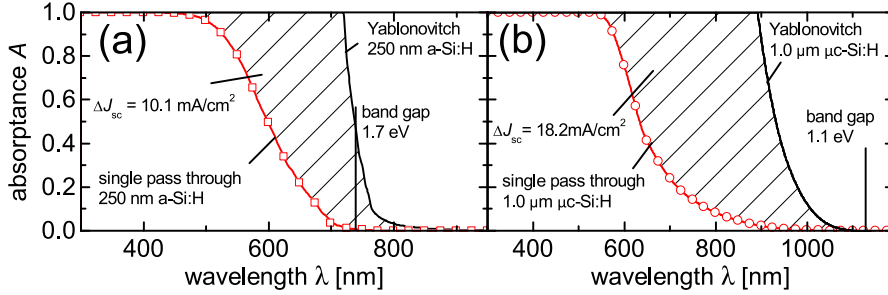


Figure 3.4: Potential for light trapping in (a) a 250 nm thick a -Si:H thin-film solar cells and (b) a 1.0 μm thick μc -Si:H thin-film solar cell. The single light pass absorption, the maximum absorption according to the Yablonovitch limit as well as the corresponding maximum enhancement of the short-circuit current density (ΔJ_{sc}) are given.

J_{sc} enhancement for the reference solar cell is 10 mA/cm². Comparing this with the maximal potential of around 18 mA/cm² (derived from the Yablonovitch limit) the current state-of-the-art light trapping exhibits a large room for improvement. It should be noted that the outcomes presented here on state-of-the-art light trapping are valid in the same way for tandem thin-film silicon solar cells, where light trapping is relevant for the μc -Si:H bottom solar cells. A similar light-trapping effect as presented for thin-film silicon solar cells in p-i-n configuration was observed for solar cells in n-i-p configuration [45, 127, 158].

In the past, several studies have investigated the light propagation in thin-film silicon solar cells with randomly textured transparent front contacts [82, 112, 114, 159–162]. One of the recent important outcomes is that the scattering of incident light at the textured front contact induces only small scattering angles of low importance for light trapping [163]. Instead, large scattering angles in the μc -Si:H absorber layer of the solar cells are induced at the textured back contact of thin film silicon solar cells [160, 164]. In the past decade, several new approaches to further increase the light trapping in thin film silicon solar cells have been investigated. These approaches span over a wide range from geometric light-trapping concepts to wave optic light-trapping concepts. Prominent examples of geometric light-trapping concepts are retroreflectors [165] or directionally selective filters [166, 167]. Examples of light-trapping concepts based on wave optics are photonic crystals [145, 149, 150, 168], grating couplers [147, 148, 158, 169–171] and plasmonics [22, 87, 115, 172] or com-

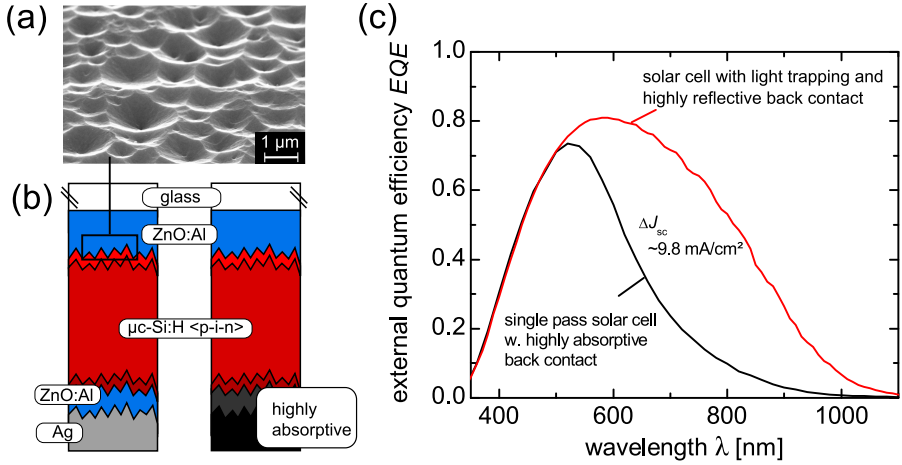


Figure 3.5: State-of-the-art light trapping in a μc -Si:H thin-film solar cell. (a) Scanning electron microscopy image of a wet-chemically etched ZnO:Al surface for light trapping. (b) Schematic cross-section of the μc -Si:H solar cell with reflection back contact and highly absorptive back contact. (c) External quantum efficiency (EQE) of the solar cells.

binations thereof [139, 143, 173]. In this work, plasmonic light trapping for thin-film silicon solar cells has been researched.

3.3 Plasmonic Light-Trapping Concepts

At metal nanoparticles or nanostructured metal layers, light can couple efficiently to plasmonic resonances (see Section 2.3). Due to this coupling, plasmonic modes in metal nanostructure are able to guide and localize incident light in solar cells. The most commonly used metals are Ag and Au as these materials are inert and exhibit strongly pronounced plasmonic resonances. However, Al and Cu nanoparticles also exhibit plasmonic resonances in the ultraviolet and visible regions of the wavelength spectrum [84]. Four fundamentally different approaches for plasmonic light trapping are presented in the following.

Localized Plasmon Induced Light Scattering at Metal Nanostructures A dominant radiative decay of LSP resonances induces very efficient scattering of in-

cident light (c.f. Section 2.3.2). If this LSPP-induced light scattering is directed into the absorber layer of a thin-film silicon solar cell, the metal nanostructures serve as sub-wavelength scattering components that couple incident propagating light into the thin absorber layers of the solar cells. Depending on the position of the metal nanostructures within the layer stack of the solar cell, different concepts have been suggested in the literature. For example, metal nanostructures placed at the front interface of solar cells have been proposed to reduce the initial reflection at the front interface of the solar cell as well as enhancing the light path in the absorber layer [87, 174–177]. In between two component cells in a multijunction solar cell, LSPP-induced light scattering at Ag nanoparticles can be used in an intermediate reflector configuration to match the short-circuit current density of the single component solar cells [141, 178]. At the rear side of the solar cell, non-ordered nanostructures on Ag back contacts as well as Ag nanoparticles placed in front of the back contact have been applied to scatter incident light such that the light is guided in the absorber layers of the solar cell [179–182].

Plasmon-Induced Coupling to Guided Modes In the case of a periodic arrangement of plasmonic nanostructures in the solar cell, the plasmon-induced scattering is able to couple incident light into propagating guided modes within the thin absorbing layer of the solar cell. These propagating guided modes can be either leaky waveguide modes [115, 139, 143, 173, 179] or surface plasmon polariton (SPP) modes [22, 138, 140, 183] as well as combinations thereof. As these modes propagate in plane with the solar cell layer stack, the power of the guided modes is absorbed partially in the semiconductor layer and thereby the J_{sc} is enhanced. In the recent studies by Ferry et al. [115, 179] as well as a publication associated with this work [173], plasmonic light trapping making use of periodic arrangements of Ag nanostructures yielded for the first time J_{sc} comparable to the state-of-the-art light trapping in thin-film silicon solar cells.

Plasmon-Induced Nearfield Enhancement In particular for small metallic nanostructures, the localized plasmon polariton resonances are accompanied by high electric field intensities in the vicinity of the nanostructures. Since the optical absorption is proportional to the square of the electric fields, high electric field enhancements lead to increased absorption. Within a semiconductor, the enhanced local absorption will increase the optical thickness of an optically thin semiconductor layer [184, 185]. This causes a possible J_{sc} enhancement of a solar cell applying small metallic nanostructures. However, LSPP-resonances in small nanostructures are also known to

exhibit very strong parasitic thermal losses [84]. In fact, for thin-film silicon solar cells it was shown that these parasitic losses are likely to be dominant when compared with potential positive effects due to near-field enhancement in the vicinity of the nanostructures [186].

Localized Plasmon Induced Photoelectron Emission for Metal Nanostructures

Incident light which couples to a metal nanostructure, can excite a LSPP resonance. Under certain conditions, this LSPP can decay into single hot electrons which can be injected over a potential barrier at the nanostructure/semiconductor interface [187–189]. As a result, a photocurrent is induced. Making use of this effect, Moulin et al. [189] showed that Ag nanoparticles embedded in *a*-Si:H solar cell devices generate a significant J_{sc} for light of energy below the band gap of *a*-Si:H (i.e., light of wavelengths longer than 750 nm). So far, the J_{sc} enhancement achieved with this effect is very small in comparison with the J_{sc} of a conventional *a*-Si:H solar cell.

Chapter 4

Nanoimprint Lithography - Replication of Light-Trapping Nanotextures

In this chapter, the development of the ultra violet nanoimprint lithography (UV-NIL) as a technology platform for the replication of nanotextures for light trapping is described. In the first section, the UV-NIL technology and the preparation processes are introduced. The replication of two exemplary types of textures is presented. First, the replication of periodic gratings by UV-NIL is studied. Such periodic textures are in the focus of several novel light-trapping concepts for thin-film silicon solar cells [115, 142, 146, 147, 173]. If covered with Ag, these periodic grating textures exhibit plasmonic resonances (see Chapter 5). Solar cells applying such plasmonic reflection gratings back contacts are investigated in Chapter 8. Second, the replication of random textures applied for state-of-the-art light trapping in thin-film silicon solar cells is studied. $\mu\text{c-Si:H}$ thin-film solar cells in p-i-n and n-i-p configuration deposited on these randomly textured substrates are presented. Parts of the results presented in this chapter have previously been published in [190, 191].

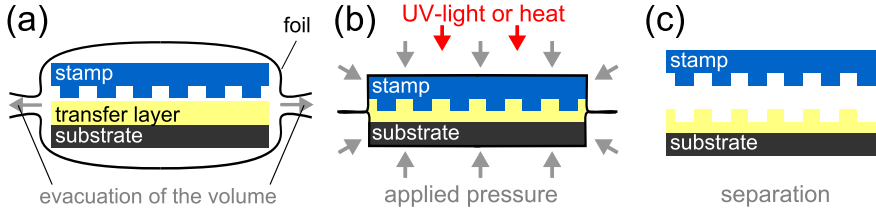


Figure 4.1: Process flow of the nanoimprint lithography with a press based on the air cushion principle.

4.1 Introduction to Nanoimprint Lithography

In the 90's of the last century, the nanoimprint lithography (NIL) as a technology to replicate nanotextured surfaces was introduced [192]. Due to its ability to combine high throughput and high transfer accuracies the nanoimprint technology quickly became a promising technology for the production of next generation integrated circuit designs as well as nano-optical components [193–195]. The NIL was added to the International Technology Roadmap for Semiconductors [196]. In the literature, a replication of nanotextures down to the dimensions of 5 nm was reported [197]. In the Forschungszentrum Jülich GmbH, the nanoimprint technology was established on a laboratory scale through two pioneering works of S. Gilles and M. Meier [198, 199]. The first steps in the adaption of the nanoimprint technology to applications in thin-film silicon solar cells are a part of this work. Other groups have recently developed a comparable process. They presented promising results of the NIL technology for photovoltaic applications [200, 201].

4.2 Nanoimprint Lithography Process

The concept of the nanoimprint process is based on the molding of a stamp texture into a liquid transfer layer on a substrate. The textured stamp is pressed into the soft transfer layer. Depending on the material of the transfer layer, UV light or temperature effects are used for the hardening of the transfer layer to sustain the inverted texture of the stamp. For the nanoimprint processes applied in this study, the commercially available Nanonex NX2000 system was used. This nanoimprint press is based on the air cushion principle. The maximum diameter of the imprint substrates

is 10 cm. In Figure 4.1, the process flow is shown. First, the stamp and the substrate with the transfer layer are placed between two foils and the volume between the foils is evacuated. Second, an air pressure of 40 bar is applied and the stamp is molded into the liquid transfer layer [198, 199]. Since the pressure is homogeneously distributed in the process chamber, the influence of dirt particles and unevenness of the stamp and the substrate of the transfer layer can be compensated. Third, either by UV-illumination of an UV-sensitive transfer layer or by the cooling of a molded soft polymer, the inverse texture of the stamp is sustained in the transfer layer.

Ultra Violet Nanoimprint Lithography If the liquid transfer layer is a UV-sensitive fused silica resist, the nanoimprint process is called UV-nanoimprint lithography (UV-NIL). In this work, two different types of UV-sensitive resists are used. The resist NXR2010 is supplied by Nanonex Cooperation. It was developed for the fabrication of nanoelectronic devices [195]. The resistOrmocomp is supplied by Microresist Technology GmbH and was explicitly designed for opto-electronic devices which require high transparencies [201]. Both resists were spin coated onto the glass substrates (NXR2010 @ 200 rpm, Ormocomp @ 3000 rpm). In addition, in order to enhance the sticking of the resist on the glass substrate, the adhesion promoter Ti-Prime from MicroChemicals GmbH and Ormoprime from Microresist Technology GmbH were deposited on the glass substrate. In order to reduce the sticking between the stamp and the replicated structure of the resist, an anti-adhesion layer is deposited on the surface of the stamp. Therefore, the surface of the stamp was exposed to the vapour of 1H,1H,2H,2H-perfluorodecyltrichlorsilane which reduces the surface free energy. The silane molecules link covalently to surface exposed silano groups. This way, a self-assembled monolayer of hydrophobic silane is formed at the surface of the stamp [198, 199].

Hot Embossing of Polymers An alternative liquid transfer layer, used in this work, is a soft, flexible and UV-transparent polymer (polyolefin plastomer, POP) [199]. During an hot embossing process, the polymer is heated up beyond its transition temperature to 90 °C. At this temperature, the polymer exhibits an enhanced viscosity. For this reason, if pressed against the stamp, the polymer flows into the textures of the stamp. When the textures of the stamp are totally filled, the polymer is hardened again by cooling it below the transition temperature. Afterwards, the textured polymer and original stamp are separated mechanically. The application of an anti-adhesion layer is not necessary for the soft polymer because it is a hydrophobic material which guarantees itself an easy release after the imprint process.

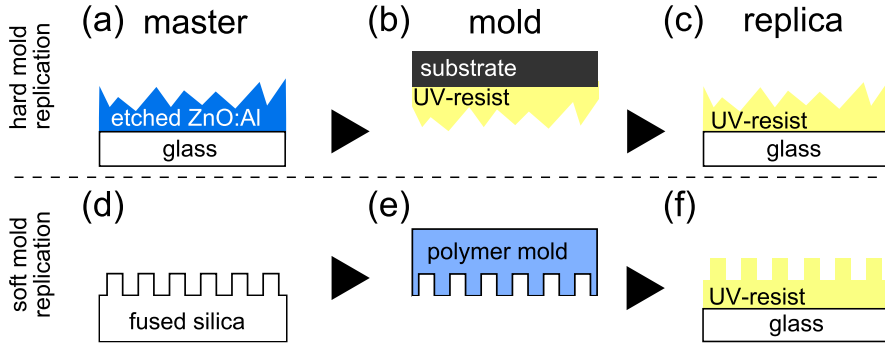


Figure 4.2: Process flows of the replication of light-trapping nanotextures. In (a) the master is made from sputter wet-chemically etched ZnO:Al and in (d) the master is made from a structured fused silica substrate (d). A hard UV-resist mold (b) and soft polymer mold (e) are molded by ultra violet nanoimprint lithography into the UV resist on the replica glass substrate in (c) and (f), respectively.

Process Flow for the Replication of Nanotextures In order to replicate any texture for light trapping, two subsequent nanoimprint steps need to be applied. This can be done, for example, in two subsequent UV-NIL processes (see Figure 4.2 (a)-(c)). In this case, in the first step, the inverted surface texture of the master is sustained in the UV-resist on top of the mold substrate. Afterwards, the original texture is replicated in the UV-resist of the replica. Under UV-illumination, the resist hardens such that the textures of the master mold are transferred onto the replica (see Figure 4.2 (c)). As the mold in this process flow is of hard matter, this replication process is referred to as the hard mold replication process. Alternatively, in the case of a soft mold replication process, the mold is a soft, flexible and UV-transparent polymer. In this case, the inverse texture of the master is sustained via hot embossing in the polymer mold (see Figure 4.2 (e)). In a subsequent UV-NIL step, the transparent polymer mold is pressed onto the UV-resist on the glass substrate of the replica. Again, under UV-illumination, the resist hardens such that the textures of the master mold are transferred onto the replica (see Figure 4.2 (d)-(f)).

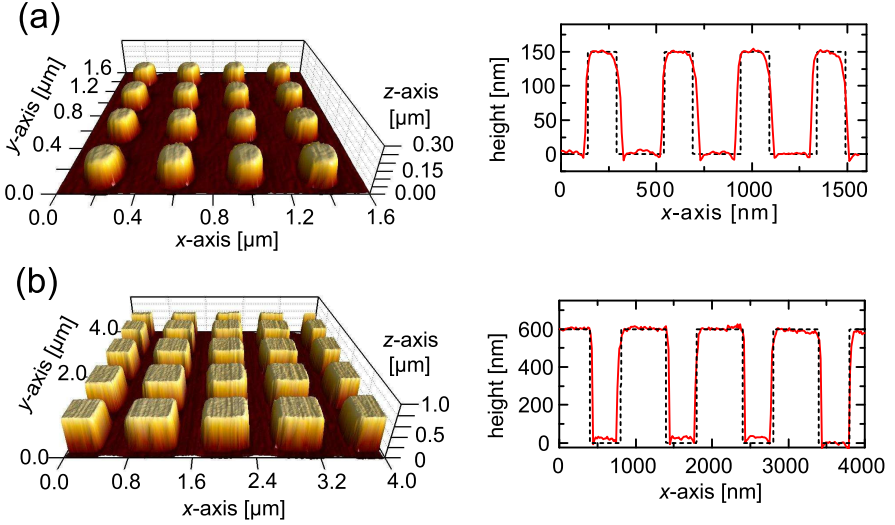


Figure 4.3: Three-dimensional AFM images and line scans of cubic nanostructures arranged in a square lattice. The lateral size of the nanostructures is (a) 150 nm and (b) 600 nm which are arranged square lattice with periods of 400 nm and 1000 nm, respectively. The line scans compare the targeted texture (dashed line) with the measured texture of the replicated structure (solid line).

4.3 Periodic Nanotextures for Light Trapping

Several novel light-trapping concepts in silicon photovoltaics with periodic textures are currently discussed in the literature [139–141, 182]. Much of the potential addressed in these studies has not been investigated experimentally yet. In order to provide a technological platform for the cheap reproduction of these textures, UV-NIL for periodic nanostructures in photovoltaic applications was developed in this work. For the periodic nanotextures of large aspect ratio, the soft mold replication process proved to be suitable. Due to the flexibility of the soft mold, problems with the separation of master and mold as well as mold and replica are avoided.

Replication Precision of Periodic Nanotextures To evaluate the precision of the UV-NIL technology of periodic nanotextures, atomic force microscopy (AFM) images of the targeted imprint nanostructures and the replica are compared. The

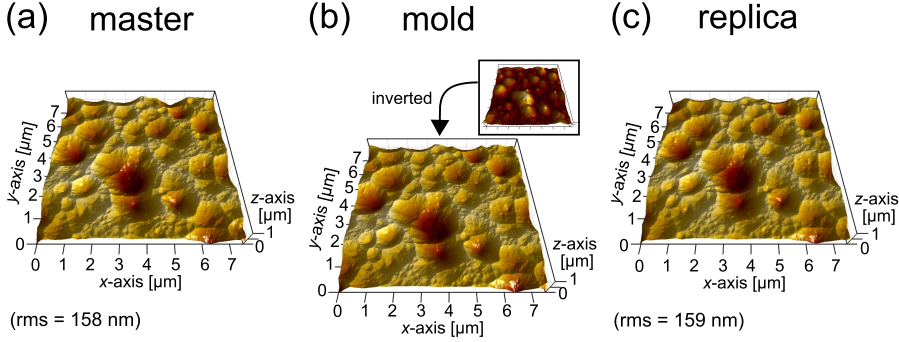


Figure 4.4: Three-dimensional AFM images of (a) the master, (b) the mold and (c) the replica.

texture of the master consists of cubic nanostructures arranged in a square lattice. The side length of the evaluated nanostructures in this work ranges from 150 nm to 600 nm with a square lattice period between 400 nm and 1200 nm. In Figure 4.3, AFM images and line scans of cubic nanostructures with lateral sizes of 150 nm and 600 nm are shown. The nanostructures are arranged in a square lattice with a period of 400 nm and 1000 nm in Figure 4.3 (a) and Figure 4.3 (b), respectively. The line scans compare the targeted and replicated texture. A very high replication accuracy is observed, in particular, for the width and periodicity of the nanostructures. At the top of the nanostructures, a small rounding of the cubic geometry is observed. A small roughness of lateral dimensions of 20 nm to 30 nm is observed in the replica. Overall, the accuracy of the replica prepared by UV-NIL in the replication process with the soft mold is very good. This conclusion holds in particular when considering the large aspect ratio of the nanotexture.

4.4 Random Textures for Light Trapping

One of the major challenges associated with the state-of-the-art light trapping in thin-film silicon solar cells is that this solar cell design demands a very challenging compromise on the transparent front contact. Since the transparent front contact acts simultaneously as the front electrode, the window layer and the light-scattering interface in the solar cells device, the electrical conductivity, the transparency and the

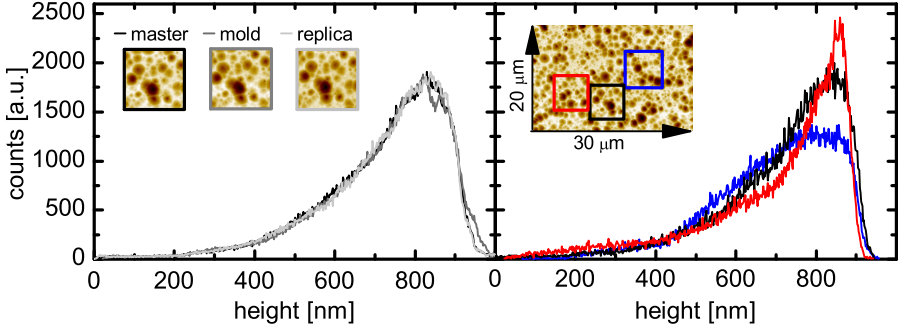


Figure 4.5: (a) Height distribution diagrams of the same position on the master, the mold and the replica. (b) Height distribution of three arbitrarily selected areas of the master ($7.5 \mu\text{m} \times 7.5 \mu\text{m}$).

light-scattering texture must be optimized (see Section 2.1.1 and Section 3.2). All of these properties strongly depend on the deposition techniques, deposition parameters and layer thickness of the front contact. In order to decouple the preparation of the light-scattering texture from the electro-optical properties of the front contact, the UV-NIL process is applied in this section to texture the glass substrate. The master substrate exhibits the state-of-the-art random texture for light trapping which is obtained by wet-chemical etched ZnO:Al layers (see Section 3.2). These textures were replicated, both with the soft mold replication process and the hard mold replication process.

4.4.1 Replication Precision of Random Nanotextures

To evaluate the replication precision of UV-NIL for state-of-the-art random textures, atomic force microscopy (AFM) images at exactly the same position on the etched ZnO:Al master, UV-NIL mold and UV-NIL replica are compared. Both, the UV-nanoimprint of the hard replication mold as well as the UV-nanoimprint replica on the glass substrate were performed with the NXR2010 resist. Figure 4.4 shows the corresponding AFM images of the master, the mold and the replica. As the mold exhibits the inverse texture of the master, the calculated inverse texture of the molds surface is shown for better comparison. In addition, the calculated root mean square values of the surface are given. It is shown that the overall texture of large and very

small features is well replicated from the master to the mold to the replica. In addition, the very similar root mean square values indicate the precise replication of the master texture in the replica. To analyse the replication precision in detail, the height distribution diagrams are shown in Figure 4.5 (a) and Figure 4.5 (b) for the master, mold and replica as well as three different positions on the master, respectively. The height distributions of the master, mold and replica match very well. This result is supported by the significant differences in the height distributions of three different reference positions on the master. Therefore, it is concluded that the replication process of the original master textures is realised at very high precision (see Figure 4.4).

4.4.2 Prototype Thin-Film Silicon Solar Cells

In this section, $\mu\text{c-Si:H}$ thin-film solar cells deposited on textured glass substrates which exhibit the state-of-the-art surface texture for light trapping are studied. The light trapping of these solar cells is compared with solar cells deposited on a ZnO:Al substrate with the same texture. Solar cells in p-i-n and n-i-p configurations were prepared. For the solar cells in n-i-p configuration, the UV-NIL glass substrate induces the texture at the rear side of the solar cell. For the solar cells in the p-i-n configuration, the UV-NIL glass substrate is located at the front side. Thus, incident light travels through the substrate and an additional difficulty associated with the light incoupling arises.

	replica substrate w. ZnO:Al thickness of			etched ZnO:Al
	250 nm	150 nm	60 nm	substrate
J_{sc} [mA/cm^2]	19.5	19.4	20.5	19,6
V_{oc} [mV]	481	484	475	479
FF	63	55	40	68

Table 4.1: Short-circuit current density (J_{sc}), fill factor (FF) and open-circuit voltage (V_{oc}) of $\mu\text{c-Si:H}$ solar cells in p-i-n configuration deposited on substrates prepared by UV-NIL and for comparison on a reference etched ZnO:Al substrate.

Thin-Film Silicon Solar Cells in p-i-n Configuration Thin-film solar cells in p-i-n configuration were fabricated on textured substrates prepared by UV-NIL and, for comparison, on a reference substrate which exhibits a ZnO:Al layer with state-of-the-art random texture for light trapping. Schematic cross-sections of the two solar cell designs are shown in Figure 4.6 (a). For the solar cell deposited on the refer-

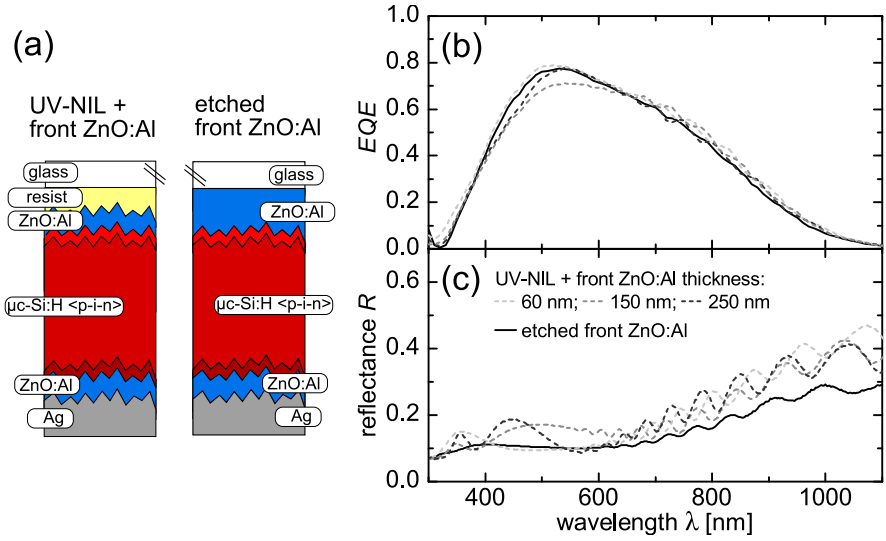


Figure 4.6: (a) Schematic cross section of $\mu\text{c-Si:H}$ solar cells in p-i-n configuration deposited on a state-of-the-art random texture ZnO:Al substrate and a replica substrate. (b) External quantum efficiency (EQE) and total reflectance (R) of $\mu\text{c-Si:H}$ solar cells in p-i-n configuration deposited on a reference etched ZnO:Al substrate and three replica substrates with front ZnO:Al layer thicknesses of 60 nm, 150 nm and 250 nm.

ence substrate, the etched ZnO:Al layer acts as the front electrode. In contrast, the replica substrates prepared by UV-NIL are non-conductive. Therefore, an additional ZnO:Al layer was deposited as the front electrode. Front ZnO:Al layers of three thicknesses were evaluated (60 nm, 150 nm and 250 nm). The EQE and the reflectance of the $\mu\text{c-Si:H}$ thin-film solar cells are compared in Figure 4.6 (b) and in Figure 4.6 (c), respectively. Independent of the thickness of the front ZnO:Al layer, for wavelengths longer than 600 nm, all solar cells deposited on the UV-NIL replica substrates exhibit an increased EQE and an increased reflectance in comparison with the reference solar cell. Thus, the solar cells deposited on the UV-NIL substrates exhibit lower parasitic absorption. The decreased parasitic losses are attributed to the decreased thickness of the ZnO:Al front contact which is known to induce strong optical losses for wavelengths longer than 600 nm [161]. In contrast to the reference solar cell, the solar cells deposited on the textured glass substrates prepared by

UV-NIL show interferences in the reflectance for wavelengths shorter than 600 nm (see Figure 4.6 (c)). These interferences are caused by the conformal layer stack of resist/ZnO:Al/ μ c-Si:H at the front side of the solar cell. They reduce the amount of light which is coupled into the solar cell which results in a decreased EQE . For wavelengths between 400 nm and 600 nm, the maxima in reflectance are associated with the decrease in EQE for the solar cells deposited on substrates prepared by UV-NIL (e.g., at wavelengths of 450 nm and 550 nm for front ZnO:Al layer thicknesses of 250 nm and 150 nm, respectively). For thin front ZnO:Al layers of 60 nm these maxima shift to wavelengths below 400 nm, allowing for a good light-incoupling. In Table 2.1, the J_{sc} , FF and V_{oc} of the solar cells are presented. The J_{sc} is slightly lower for front ZnO:Al layer thicknesses of 250 nm and 150 nm when compared with the reference solar cell. This is attributed to the above explained ZnO:Al layer thickness dependent enhanced reflection at the front side of the solar cells which are deposited on the substrates prepared by UV-NIL. For a front ZnO:Al layer thicknesses of 60 nm, however, an enhanced EQE and J_{sc} in comparison with the conventional etched ZnO:Al substrate is shown for the replica substrate prepared by UV-NIL. Since the ZnO:Al layer thickness is strongly reduced in this solar cell layer stack, the sheet resistance is enhanced. As a result, the FF of the studied solar cells and in turn the efficiency of the solar cell is decreased. Considering the variations of the texture of the substrate, the V_{oc} is comparable. The small deviations in V_{oc} of around 10 mV are associated with deviations in the material quality of the μ c-Si:H absorber layer of the solar cell. A substrate-dependent growth of the μ c-Si:H material has been reported by in the literature [202, 203].

Thin-Film Silicon Solar Cells in n-i-p Configuration In this section, the light trapping of μ c-Si:H solar cells in n-i-p configurations deposited on an inverted and an original state-of-the-art random texture for light trapping are compared. The inverted state-of-the-art random texture for light trapping is prepared by a single UV-NIL process of the original texture. In contrast to the p-i-n configuration, for the n-i-p configuration, the μ c-Si:H layers are deposited on the textured ZnO:Al/Ag back contact. Thus, the textured substrates induce the random texture for light trapping in solar cells, but the light does not propagate through the textured resist. A schematic cross-section of the complete solar cell layer stack is shown in Figure 4.7 (a). All solar cells compared in this section were deposited in the same deposition run.

Figure 4.7 (b) shows the EQE of the solar cells deposited on the reference substrate and the substrate prepared by UV-NIL with the inverted texture. In the wavelength range from 450 nm to 550 nm, the solar cell with the inverted back contact textures

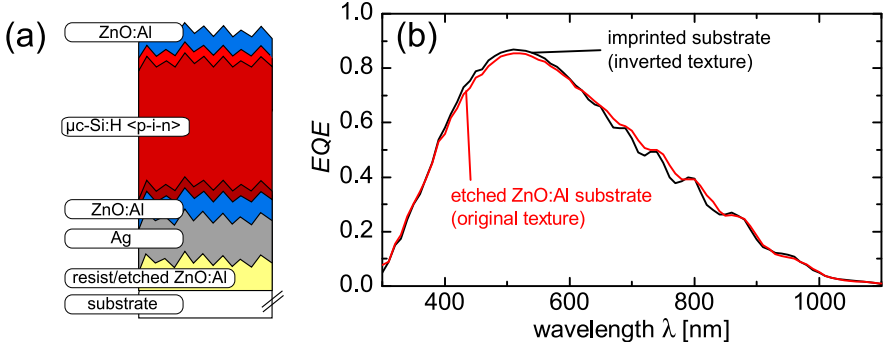


Figure 4.7: External quantum efficiency (EQE) of $\mu\text{c-Si:H}$ solar cells in n-i-p configuration deposited on a master type etched ZnO:Al substrate and a substrate prepared by UV-NIL, which exhibits the inverse texture.

shows a slightly increased EQE in comparison with the solar cells with the original back contact textures. In the wavelength range from 660 nm to 830 nm, the solar cell with the inverted back contact shows a slightly decreased EQE compared with those cells with the original back contact textures. Due to these differences in EQE , the J_{sc} differs for the solar cell deposited on the inverted and original texture at the back contact (see Table 2.2). This difference is ascribed to the different in light trapping by the original random texture and the inverted texture. However, for a detailed understanding of the effect, future experimental studies and optical simulations are required. Considering the experimental variations, the V_{oc} and FF are comparable. This indicates that the material properties of the deposited $\mu\text{c-Si:H}$ are comparable and not affected significantly by an inversion of the surface texture at the back contact. The efficiencies of the solar cells are comparable as the observed difference in J_{sc} is small.

4.5 Conclusion and Discussion

Status of the UV-Nanoimprint In this chapter, it was demonstrated that the UV-NIL technology is capable of replicating light-trapping nanotextures for thin-film silicon solar cells at high precision. Two types of texture were studied, randomly textured ZnO:Al substrates and periodic nanotextures. The successful fabrication

	nanoimprint substrate (inverse texture)	etched ZnO:Al substrate (original texture)
J_{sc} [mA/cm ²]	20.38	21.02
V_{oc} [mV]	506	505
FF	0.715	0.716

Table 4.2: Short-circuit current density (J_{sc}), fill factor (FF) and open-circuit voltage (V_{oc}) of μc -Si:H thin-film solar cells in n-i-p configuration deposited on a UV-NIL substrate (inverse texture) and an etched ZnO:Al substrate (original texture).

of μc -Si:H thin-film solar cells on replicas of randomly textured ZnO:Al surfaces demonstrated that the UV-nanoimprint process can be integrated into the conventional thin-film silicon solar cell preparation. Both, in n-i-p and p-i-n configuration, μc -Si:H thin-film solar cells deposited on the substrates prepared by UV-NIL showed a good light trapping in comparison with solar cells deposited on the original texture. For the n-i-p configuration, very similar FF and V_{oc} data were found for the solar cells grown on the original etched ZnO:Al substrate and the substrate prepared by UV-NIL. However, for the solar cells in p-i-n configuration, the modification of the dielectric layer stack at the front contact induces difficulties with the incoupling of incident light in the solar cell. An efficient incoupling was observed only for a thin and low conductive front contact. Due to the low conductivity, the FF of these solar cell is decreased. For future work, there are two strategies to tackle this problem: (i) by decreasing the sheet resistance of the front contact layer of thickness of around 60 nm and (ii) by modifying the texture, such that the incoupling of incident light via the conformal resist/ZnO:Al/ μc -Si:H front contact is enhanced even for ZnO:Al films thicknesses with reasonable conductivity. For the latter approach, new random textures should be used at the front contact which exhibit a combination of small and large features in comparison with the wavelength [204].

Relevance of UV-NIL for Photovoltaic Industries The first industrial implementation of the UV-NIL technology was realized in 2008 by scientists of Hewlett-Packard [205]. They demonstrated that NIL is, in principle, compatible with commercial integrated circuit fabrication process without changing the current infrastructure in IC industry. In particular, so-called 'Roll-to-Roll' nanoimprint is promising for industrial applications as it guarantees a high volume throughput in industrial assembly lines. However, for the photovoltaic industry, where NIL could replace the current ways to induce textures for light trapping, new challenges arise. On the one hand,

for industrial application, the NIL must be adapted to much larger areas. On the other hand, the production costs must be competitive with standard approaches. For both aspects, a polymer mold as used in this chapter for the replication of the periodic textures would be the better choice. The material is flexible and convenient for the application in a high throughput roll-to-roll mass production on large substrates. Additionally, the costs of a polymer mold are moderate compared with many other technologies for nanopatterning such as e-beam lithography. In addition, the polymer mold has a long life time, due to its low fragility [206].

Prospects of UV-NIL for the Prototyping of Novel Textures for Light Trapping

As described previously, light trapping remains one of the key challenges which need to be tackled to ensure the prospects of several emerging photovoltaic technologies. In order to design and realize novel nanotextures for light trapping, UV-NIL is a very useful technology. Examples of such textures are grating textures, two dimensional photonic crystals and plasmonic devices [115, 139, 173]. In Chapter 8, the application of nanoimprint for the fabrication of μc -Si:H thin-film solar cells incorporating a plasmonic light-trapping nanotexture is demonstrated.

Chapter 5

Design of Plasmonic Back Contacts for Light Trapping

In this chapter, the plasmon-induced light scattering at nanostructured Ag back contacts for light trapping in thin-film silicon solar cells is investigated. The electromagnetic coupling of incident light, localized surface plasmon polariton resonances in nanostructured Ag back contacts and the scattered propagating light were simulated with a three-dimensional numerical solver of Maxwell's equations. The design of the nanostructures was optimized regarding their ability to scatter incident light at low optical losses into large angles in the silicon absorber layers of the thin-film silicon solar cells. Geometrical parameters as well as the embedding material of single and periodic nanostructures on Ag layers were varied. This chapter is based on a previous publication [173].

5.1 Light Trapping with Plasmonic Back Contacts

Incident light couples efficiently to LSPP resonances in Ag nanoparticles or nanostructures on Ag layers (see Section 2.3.2). For certain geometries, a radiative decay of these resonances causes a very efficient scattering of the incident light. This way, Ag nanostructures which carry LSPP resonances serve as sub-wavelength scattering components that couple incident light into the a -Si:H or μ c-Si:H absorber layers of a thin-film silicon solar cell. Depending on the position of the Ag nanostructures

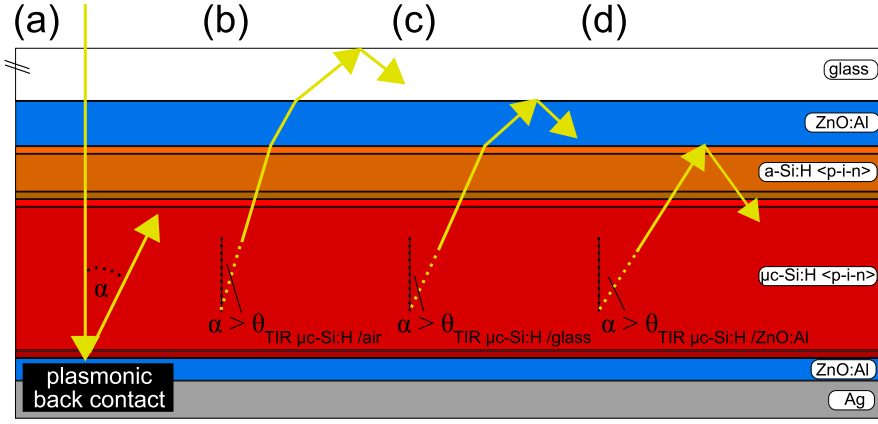


Figure 5.1: Illustration of the light path enhancement via light scattering at plasmonic back contacts of tandem thin-film silicon solar cells. The reflection at the front interface in the case of scattering angle (α) larger than the total internal reflection angle (Θ_{TIR}) of the front interfaces is illustrated.

inside the layer stack of the solar cell, different concepts to make use of the LSPP-induced scattering have been suggested in the literature (see Section 3.3). In this work, LSPP-induced light scattering by nanostructured Ag back contacts in thin-film silicon solar cells is studied. There are some advantages for the positioning of the Ag nanostructures at the rear side of the solar cell. In contrast to nanoparticles, which are often researched, nanostructured Ag back contacts are investigated as their preparation and implementation into the rear side of the solar cell is less complex. In particular, the recent progress in nanoimprint technologies offers exciting perspectives to prepare nanostructured substrates [190,201]. Second, nanostructured Ag back contacts are not in contact with the absorber layer. Thus, no additional recombination losses are expected when comparing with the state-of-the-art random textures for light trapping in thin-film silicon solar cells. Most importantly, by locating the plasmonic scattering nanostructures at the rear side of the solar cell, the operating spectral range of the plasmonic scattering nanostructures is limited to a smaller wavelength range of $500 \text{ nm} < \lambda < 1100 \text{ nm}$. In typical thin-film silicon solar cells, due to the high absorption in the $a\text{-Si:H}$ and $\mu\text{c-Si:H}$ layers, only light of wavelengths above 500 nm reaches the rear side (see Section 2.1). For wavelengths longer than 1100 nm and 750 nm, the absorption vanishes due to the band gaps of the materials $\mu\text{c-Si:H}$ and

α -Si:H, respectively. The reduction of the operational spectral range of the plasmonic back contact releases the requirements on the design of the nanostructures. In particular, potential plasmon-induced absorption losses can be reduced by shifting them out of the operational wavelength region.

Light Trapping via Light Scattering at Plasmonic Back Contacts For μ c-Si:H thin-film solar cells as well as tandem thin-film silicon solar cells with a μ c-Si:H bottom solar cell, the intrinsic μ c-Si:H absorber layer is many wavelengths thick, such that the front and rear interface of the μ c-Si:H p-i-n diode are evanescently decoupled. The introduction of Ag nanostructures on the back contact of a μ c-Si:H thin-film solar modifies the light absorption profile for wavelengths longer than 500 nm. First, due to light scattering at the Ag nanostructures on the back contact, the light path is enhanced by $1/\cos(\alpha)$, with α being the scattering angle (see Figure 5.1 (a)). Second, for scattering angles larger than the total internal reflection angle of a flat μ c-Si:H/air interface the scattered light is totally reflected at its incidence on the front interface. Following Snell's law of diffraction along presumably flat interfaces of the materials in the solar cell, it is found that light which is scattered at the back contact beyond the total internal reflection angle of μ c-Si:H/air will be totally reflected back into the solar cell, at the latest, at the glass/air front interface (see Figure 5.1 (b)). As a result, the light path of the light scattered at the back contact of the solar cells beyond the total internal reflection angle of the μ c-Si:H/air interface is significantly enhanced. The same argument applies for scattering angles α beyond the total internal reflection angle of the μ c-Si:H/glass and μ c-Si:H/ZnO:Al interface (see Figure 5.1 (c) and Figure 5.1 (d), respectively). In the latter case, the scattered light does not propagate in the front ZnO:Al layer, avoiding parasitic optical losses due to absorption in the front ZnO:Al layer. It should be noted that for solar cells with textured front contacts, due to the variation of surface angles at the front interfaces, the application of the total internal reflection angle criteria is not exact (Figure 5.1 (b)-(d)). However, as a figure of merit to evaluate the scattering angles of a plasmonic back contact, the total internal reflection criteria of the flat μ c-Si:H/air interface and the flat μ c-Si:H/ZnO:Al interface are very useful.

In conclusion, in order to achieve a good light trapping, the nanostructured Ag back contacts need to show efficient scattering of incident light into large angles in the μ c-Si:H layer of the thin-film silicon solar cell at low optical losses. Of particular relevance are those scattering angles beyond the total internal reflection angle of a flat μ c-Si:H/air and μ c-Si:H/ZnO:Al interface.

5.2 Plasmonic Light Scattering of Nanostructures on Ag Back Contacts

5.2.1 Ag Nanoparticles vs. Nanostructures on Ag Back Contacts

Isolated Ag nanoparticles are well-known for their strong LSPP-induced light scattering. For this reason, several authors have investigated them for the application as light-scattering components in solar cells [20, 22, 174, 175, 180, 181, 207]. In order to evaluate the LSPP-induced light scattering at nanostructured Ag back contacts, the Q_{abs} and Q_{sca} of isolated Ag nanostructures are compared with those calculated by the Mie theory for isolated Ag nanoparticles. The embedding medium is set to ZnO:Al as this dielectric material is commonly used at the rear side of a thin-film silicon solar cell to separate the silicon absorber layers and the Ag back layer. In Figure 5.2, the Q_{abs} and Q_{sca} of isolated Ag nanoparticles and isolated hemispherical nanostructures of Ag interfaces are shown. The radius of the Ag nanostructure is varied from 25 nm to 200 nm and the radius of the nanoparticle is varied from 20 nm to 100 nm. Values of Q_{abs} and Q_{sca} larger than unity express that the investigated Ag nanostructures and Ag nanoparticles scatter and absorb more light intensity than irradiated on their cross-section (Eq. (2.17)). Values of Q_{abs} and Q_{sca} above unity are a clear indication for LSPP resonances, where incident electromagnetic energy from the surrounding space couples to the coherent oscillation of the free electron gas in the Ag nanostructure and Ag nanoparticle [84, 86].

For Ag nanoparticles of small radii and nanostructures on Ag surfaces of small radii, the Q_{abs} is dominant. With an increasing radius, the Q_{sca} increases and for radii above 50 nm and 40 nm, the Q_{sca} is dominant for the Ag nanostructure and Ag nanoparticle, respectively. In addition, with an increasing radius of the two geometries, the dominant LSPP resonance, which is associated with the dipolar resonance, broadens spectrally and shifts to longer wavelengths. Additional LSPP multipole resonances appear at shorter wavelengths for both geometries. Thus, the LSPP resonances in the nanoparticle and the LSPP resonances in nanostructures on Ag back contacts have several similarities. However, when comparing the LSPP resonances of hemispherical Ag nanostructures and Ag nanoparticles of the same radius, with increasing radius, the LSPP resonance of Ag nanoparticles significantly shifts to longer wavelengths. For this reason, the choice of radius which results in a dominant light scattering at low absorption in the operational wavelength range of the back contact

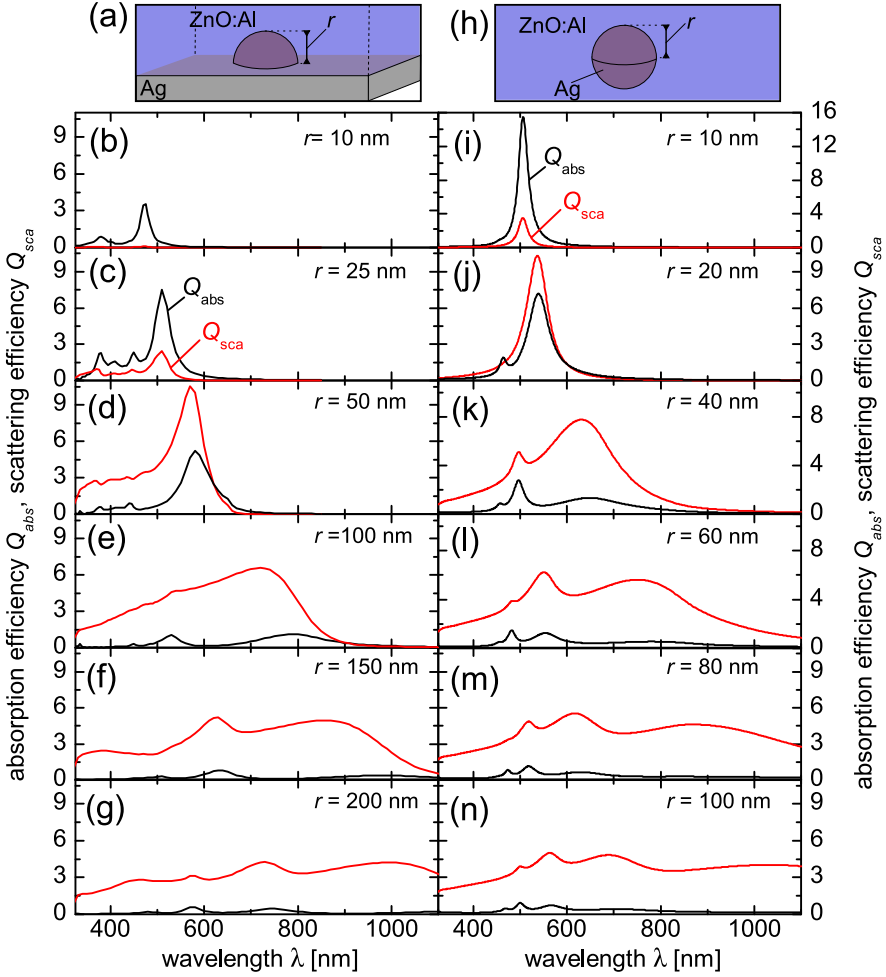


Figure 5.2: Simulated absorption efficiency (Q_{abs}) and scattering efficiency (Q_{sca}) of (a)-(g) isolated hemispherical Ag nanostructures on Ag surfaces embedded in ZnO:Al and (h)-(n) isolated spherical Ag nanoparticles embedded in ZnO:Al. The radius of the nanoparticles and nanostructures is varied.

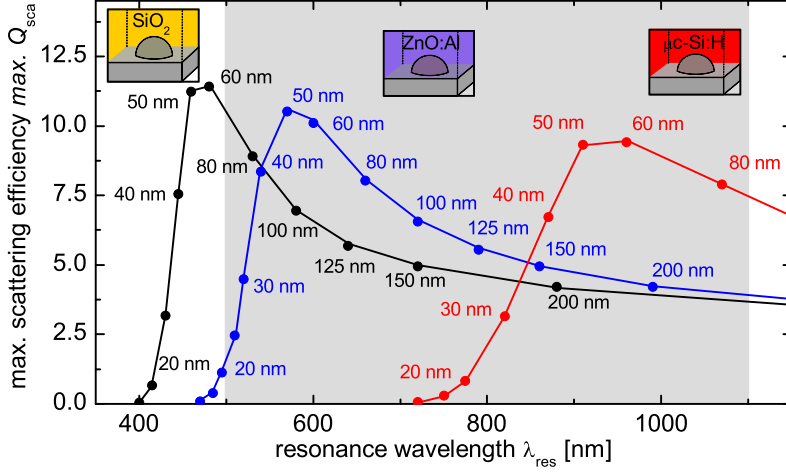


Figure 5.3: Simulated maximum scattering efficiency ($max. Q_{sca}$) of the dominant LSPP resonance of hemispherical Ag nanostructures as a function of the resonance wavelength (λ_{res}). The radius of the nanostructure is varied from 10 nm to 200 nm and the embedding material is set to SiO₂, ZnO:Al and μ c-Si:H. The gray region indicates the operational spectral range of a plasmonic back contact.

(wavelengths between 500 nm and 1100 nm) differs between the Ag nanoparticle and Ag nanostructure. For the hemispherical Ag nanostructure, an efficient light scattering at low optical losses in this spectral range is found for radii larger than 100 nm.

5.2.2 Embedding Material of Nanostructures on Ag Back Contacts

In addition to the size of the nanostructure, the shape and the embedding material influence the LSPP resonance. In order to simplify the illustration, in Figure 5.3, instead of full spectral information, only the maximum values of the scattering efficiency ($max. Q_{sca}$) at the dominant LSPP resonance of hemispherical Ag nanostructures embedded in different materials are plotted against the resonance wavelength. The embedding material of the hemispherical Ag nanostructure is varied from SiO₂ ($n_{SiO_2} \approx 1.45$) to ZnO:Al ($n_{ZnO:Al} \approx 1.6-2.0$) and to μ c-Si:H ($n_{\mu c-Si} \approx 3.5$). With an increasing refractive index n of the embedding material, a general increase of the

dominant LSPP resonance wavelength is observed. If the embedding material is set to $\mu\text{c-Si:H}$, the LSPP resonances of hemispherical nanostructures shift significantly to longer wavelengths in comparison with ZnO:Al and SiO_2 . In this case, only the LSPP resonances of small nanostructures (radius < 80 nm) embedded in $\mu\text{c-Si:H}$ are located within the operating spectral range of the back contact ($500 \text{ nm} < \lambda < 1100 \text{ nm}$). However, for these sizes of nanostructures, the LSPP resonances show strong optical losses (see Figure 5.2). Therefore, regarding the light scattering at the back contact of solar cells, $\mu\text{c-Si:H}$ is not a favorable embedding material. Instead, an embedding material of lower refractive index like ZnO:Al ($n_{\text{ZnO:Al}} \approx 1.6\text{--}2.0$) or SiO_2 ($n_{\text{SiO}_2} \approx 1.45$) is favorable for plasmonic light trapping with nanostructured Ag back contacts. If embedded in a low refractive index material, the LSPP resonances of large and efficiently scattering nanostructures (radius > 100 nm) are located in the operating spectral range of the back contact.

5.2.3 Shape of Nanostructures on Ag Back Contacts

In addition to the embedding material and the size of the Ag nanostructure the shape of the nanostructures influences the LSPP resonances [84]. For this reason, isolated conical, cylindrical and hemispherical nanostructures on Ag layers embedded in ZnO:Al were studied. In Figure 5.4, the *max.* Q_{sca} and the *max.* Q_{abs} values of the dipolar LSPP resonance of these nanostructures are shown as a function of the resonance wavelength (λ_{res}). For all geometries, the height of the nanostructure is set equal to the radius of the cross-section of the nanostructure. It is shown that the LSPP resonances of cylindrical nanostructures are shifted to longer wavelengths and the LSPP resonance of conical nanostructures are shifted to shorter wavelengths in comparison with hemispherical Ag nanostructures. Regarding light trapping in solar cells, high scattering efficiencies at low optical losses are required in the operational spectral range of the back contact. For conical nanostructures, the Q_{sca} values are lowest. Thus, this shape is not a favorable geometry to efficiently scatter incident light at the rear side of the solar cell. The highest *max.* Q_{sca} but also the highest *max.* Q_{abs} are found for cylindrical nanostructures. For example, for a radius of 80 nm, the investigated cylindrical nanostructures show a *max.* Q_{sca} at the dipolar LSPP resonance of 13.8 and a *max.* Q_{abs} of 3.1. In order to identify nanostructures which scatter incident light at comparably low absorption losses, the fraction (*max.* Q_{abs})/(*max.* Q_{sca}) is a suitable figure of merit. For the cylindrical nanostructure of radius of 80 nm, a (*max.* Q_{abs})/(*max.* Q_{sca}) value of 22.2% is calcu-

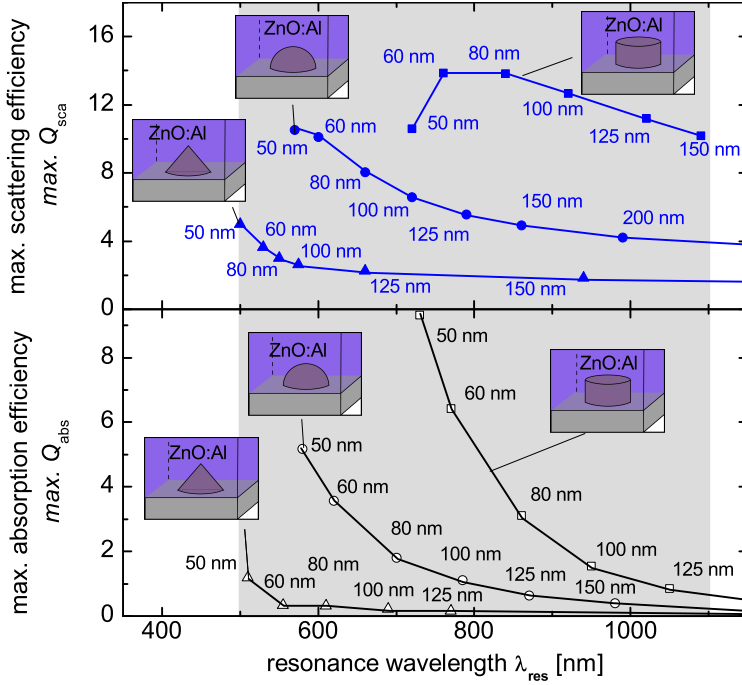


Figure 5.4: (a) Simulated maximum scattering efficiency ($\max. Q_{\text{sca}}$) and (b) simulated maximum absorption efficiency ($\max. Q_{\text{abs}}$) at the dominant LSPP resonance of Ag nanostructures embedded in ZnO:Al as a function of the resonance wavelength λ_{res} . The radius and shape of the nanostructure is varied. The gray region indicates the operational spectral range of a plasmonic back contact.

lated. A quite similar relative ($\max. Q_{\text{abs}}/(\max. Q_{\text{sca}})$) value of 22.3% is observed for the hemispherical nanostructure of the same radius at a relatively large Q_{sca} of 8.1. Thus, hemispherical and cylindrical nanostructures of the same radius scatter incident light at similar radiative efficiencies. However, for hemispherical nanostructures, LSPP resonances of larger nanostructures (e.g., radii of around 150 nm) are located in the operational wavelength range of the back contact. For these nanostructures, the ratio ($\max. Q_{\text{abs}}/(\max. Q_{\text{sca}})$) is much smaller (for radius of 150 nm ($\max. Q_{\text{abs}}/(\max. Q_{\text{sca}}) = 7.6\%$) allowing a more efficient scattering of incident light at comparably lower optical losses at the back contact of the solar cell.

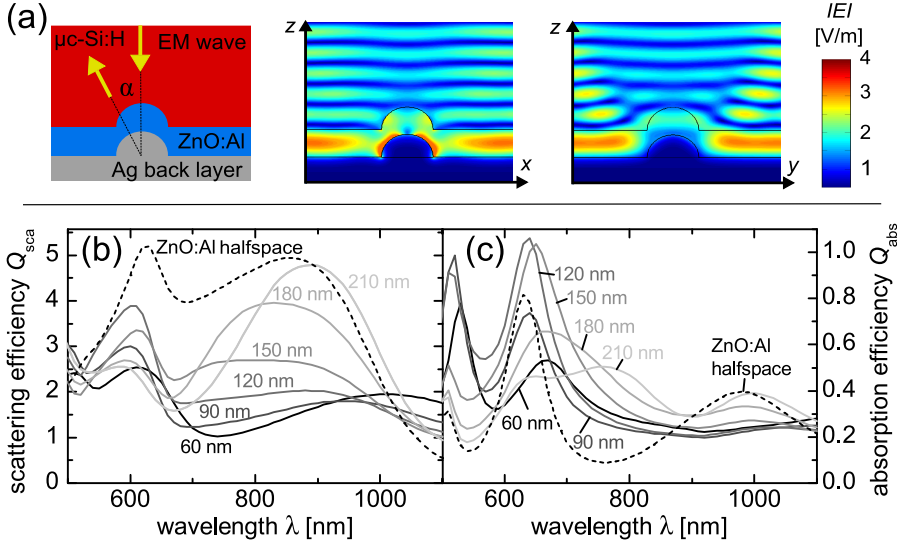


Figure 5.5: (a) Schematic cross-section and absolute electric field in the planes parallel and perpendicular to the polarization of the incident electromagnetic wave (radius of 150 nm, ZnO:Al layer thickness of 180 nm, wavelength of 850 nm). (b) Simulated scattering efficiency (Q_{sca}) and (c) simulated absorption efficiency (Q_{abs}) of Ag nanostructures (radius of 150 nm) embedded conformally in a ZnO:Al/ $\mu\text{c-Si:H}$ layer stack. The thickness of the ZnO:Al layer is varied from 60 nm to 210 nm.

5.2.4 Light-Trapping with Plasmonic Light Scattering

Impact of the Thickness of the ZnO:Al Intermediate Layer on the LSPP Resonance of Isolated Hemispherical Nanostructures on Ag Back Contacts In the previous sections, solely isolated nanostructures on Ag surfaces embedded in dielectric half-space were investigated. In thin-film silicon solar cells, the Ag back contact is covered conformally by a ZnO:Al/ $\mu\text{c-Si:H}$ layer stack (see Figure 5.5 (a)). In particular, when evaluating the angular information of the light scattering of nanostructures on Ag back contacts, the Ag/ZnO:Al/ $\mu\text{c-Si:H}$ layer stack needs to be considered. In Figure 5.5 (b) and Figure 5.5 (c), the Q_{abs} and Q_{sca} of an isolated hemispherical Ag nanostructure (radius = 150 nm) on the Ag surface of the back contact is shown. The thickness of the ZnO:Al interlayer is varied from 60 nm to 210 nm. Over the total spectral range, the Q_{sca} values are larger than unity. This indicates an efficient

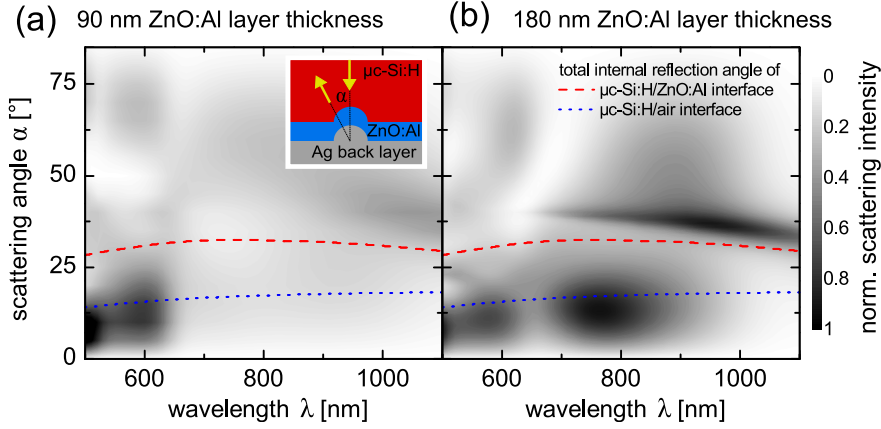


Figure 5.6: Normalized intensity distribution of the scattered light of hemispherical Ag nanostructures (radius of 150 nm) embedded conformally in ZnO:Al and $\mu\text{c-Si:H}$. The thickness of the ZnO:Al layer is 90 nm and 180 nm in (a) and (b), respectively.

coupling of incident light to LSP resonances in hemispherical Ag nanostructures on the back contact of thin-film silicon solar cells. Similarly to the nanostructures embedded in a dielectric half-space, the nanostructures on the back contact are able to scatter a multiple of the light intensity irradiated on their cross-section into the $\mu\text{c-Si:H}$ absorber layer. Yet, the spectral scattering characteristic is strongly influenced by the Ag/ZnO:Al/ $\mu\text{c-Si:H}$ layer stack. By introducing the ZnO:Al/ $\mu\text{c-Si:H}$ interface, the system induces additional interferences which are superimposed on the LSP resonances of the isolated hemispherical nanostructure embedded in a ZnO:Al half-space (c.f. Figure 5.2). Depending on the spatial position of these interferences, the LSP resonances observed in a ZnO:Al half-space are enhanced or attenuated. For example, for ZnO:Al thicknesses smaller than 120 nm, the dipolar LSP resonance around 870 nm is suppressed and for ZnO:Al layer thicknesses above 120 nm, the LSP resonance around 630 nm is suppressed. Overall, the Q_{abs} and Q_{sca} spectral characteristics are strongly modified in comparison with a single nanostructure embedded in a ZnO:Al half-space.

Scattering Characteristics of LSP Resonances of Isolated Hemispherical Nanostructures on Ag Back Contacts

In order to assess the scattering characteristics of LSP resonances in nanostructures on Ag back contacts, the intensity distribution

of the scattered light in the farfield is calculated from the simulated three-dimensional electromagnetic field. Therefore, a farfield expansion of the electric field was used to calculate the intensity distribution of scattered light at a distance of 1 m away from the nanostructure. In Figure 5.6, the normalized intensity distribution of the scattered light is shown as a function of the scattering angle in the $\mu\text{c-Si:H}$ layer and the wavelength. The scattering angle is defined as the difference in angle to the axis of incidence (see the inset of Figure 5.6). For the shown exemplary cases, the radius of the nanostructure is set to 150 nm and the thickness of the conformal ZnO:Al layer is 90 nm and 180 nm. The considered wavelength range is set to the operating spectral range of the back contact ($500 \text{ nm} < \lambda < 1100 \text{ nm}$). For both ZnO:Al layer thicknesses, in the wavelength range between 550 nm and 900 nm, the maxima of the scattering intensity are located at around 15° . These scattering angles are located below the angle of total reflection (red dashed line) of a flat ZnO:Al/ $\mu\text{c-Si:H}$ interface. Such scattering angles of the scattered light in the $\mu\text{c-Si:H}$ layer are caused by the coupling of the LSPP resonance to propagating modes in the ZnO:Al layer. At the ZnO:Al/ $\mu\text{c-Si:H}$ interface, these propagating modes are then refracted according to geometrical optics. In addition, a substantial amount of the light is scattered beyond the angle of total reflection at the ZnO:Al/ $\mu\text{c-Si:H}$ interface. For a ZnO:Al layer thickness of 180 nm, a strongly pronounced maximum is located at wavelengths of around 1000 nm. Such scattering angles beyond the angle of total reflection at a flat ZnO:Al/ $\mu\text{c-Si:H}$ interface would be prohibited in geometrical optics. As this effect was identified also for perfectly flat ZnO:Al/ $\mu\text{c-Si:H}$ interfaces, it is explained by a near-field coupling of the plasmonic resonance in the Ag nanostructure to propagating modes in the $\mu\text{c-Si:H}$ layer. The effect disappears with increasing ZnO:Al layer thickness which is an additional indication of a near-field coupling effect. In essence, for thin ZnO:Al layers, near-field coupling of LSPP resonances in the Ag nanostructures to propagating modes in the $\mu\text{c-Si:H}$ absorber layer allows the scattering of light into large angles in the $\mu\text{c-Si:H}$ layer.

Evaluation of Light Scattering of Single Nanostructures on Ag Back Contacts in Terms of Light Trapping

In Section 5.1, it was shown that an efficient plasmonic light trapping requires the scattering of incident light at the back contact into large angles in the $\mu\text{c-Si:H}$ absorber layer. First, the light path in the $\mu\text{c-Si:H}$ layer is simply enhanced by the scattering angle (see Figure 5.1). Second, light scattered to angles beyond the angle of total reflection of a flat $\mu\text{c-Si:H/ZnO:Al}$ and/or $\mu\text{c-Si:H/air}$ interface will more probably be guided in the silicon absorber layers (see Figure 5.1 (a) and Figure 5.1 (c) for a flat $\mu\text{c-Si:H/air}$ and $\mu\text{c-Si:H/ZnO:Al}$ front inter-

face, respectively). In order to compare the light-trapping potential of various ZnO:Al layer thickness, the average absorption efficiency (\bar{Q}_{abs}) and average scattering efficiency (\bar{Q}_{sca}) values averaged over the operating spectral range of the back contact are shown for hemispherical nanostructures on Ag back contacts as a function of the ZnO:Al layer thickness in Figure 5.7. The radius of the nanostructures is set to 150 nm. In addition, two fractions of \bar{Q}_{sca} are presented which quantify the amount of light scattered beyond the total internal reflection angle of the $\mu\text{c-Si:H/air}$ interface and beyond the total internal reflection angle of the $\mu\text{c-Si:H/ZnO:Al}$ interface. The thickness of the ZnO:Al layer was varied from 15 nm to 500 nm. Devices with ZnO:Al layer thickness larger than 500 nm suffer from either poor conductivity or large optical losses. Furthermore, ZnO:Al layers of thicknesses smaller than 15 nm are difficult to deposit uniformly. For all thicknesses of the ZnO:Al layer investigated, the LSPP-induced optical losses of the Ag nanostructure are low. The \bar{Q}_{abs} is always smaller than 10% of the \bar{Q}_{sca} . However, a significant variation of the \bar{Q}_{sca} is observed by changing the thickness of the ZnO:Al layer. The highest total \bar{Q}_{sca} values are observed for large thicknesses of the ZnO:Al layer (> 500 nm) or small thicknesses (< 45 nm). The smallest values of the total \bar{Q}_{sca} of around 1.85 are observed for the conventional thickness of the back ZnO:Al layer of around 80 nm. However, in this configuration, the relative amount of light scattered to large angles beyond the angle of total reflection at the $\mu\text{c-Si:H/ZnO:Al}$ interface (50%) as well as the $\mu\text{c-Si:H/air}$ interface (70%) are highest. With increasing thickness, the total \bar{Q}_{sca} increases, but the relative amount of light scattered to large angles decreases. For the application of LSPP-induced light scattering at nanostructured Ag back contacts, both aspects are important: Larger values of \bar{Q}_{sca} allow a smaller surface coverage of nanostructures at high diffuse reflectance and large scattering angles are important for an enhanced light-trapping effect in the solar cells. A reasonable compromise is found for ZnO:Al thicknesses of around 180 nm, where a \bar{Q}_{sca} value of 2.7 is found and 43% and 60% of all incident light is scattered to angles larger than the total internal reflection angle of $\mu\text{c-Si:H/ZnO:Al}$ and $\mu\text{c-Si:H/air}$, respectively.

Outlook on Light Trapping with Nanostructured Ag Back Contacts In this section, it was demonstrated that incident light couples very efficiently to LSPP resonances in Ag nanostructures on the back contact of thin-film silicon solar cells. Due to LSPP resonances, nanostructures on Ag back contacts are found to scatter a multiple of the light irradiated on their cross-section at low optical losses into the $\mu\text{c-Si:H}$ layer of the solar cell. Even if averaged over the operating spectral range, depending on the ZnO:Al thickness, between 1.8 and 4 times of the light irradiated on the cross-

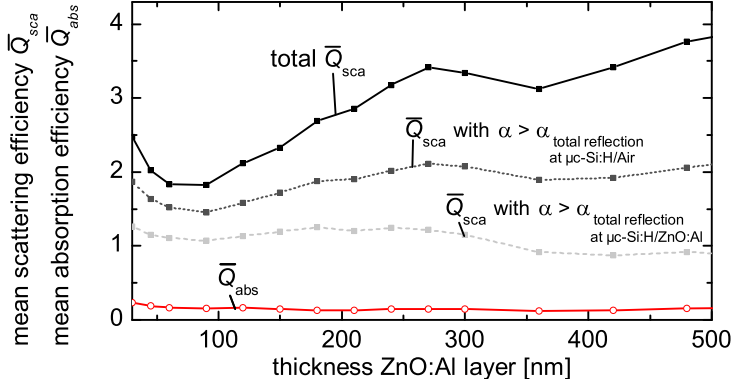


Figure 5.7: Averaged scattering efficiency (\bar{Q}_{sca}) and absorption efficiency (\bar{Q}_{abs}) of isolated hemispherical nanostructures on Ag back contacts (radius = 150 nm). The data is averaged over the operational wavelength range of the back contact ($500 \text{ nm} < \lambda < 1100 \text{ nm}$). Two subdivisions of \bar{Q}_{sca} are given for such light scattered beyond the total internal reflection angle at a flat $\mu\text{c-Si:H/ZnO:Al}$ interface and a flat $\mu\text{c-Si:H/air}$ interface.

section of the nanostructures can be scattered. For an optimized ZnO:Al thickness, up to 70% of the light scattered can be scattered to angles larger than the total internal reflection angle of the $\mu\text{c-Si:H/air}$ interface and is, in turn, reflected at the front side. Up to 50% of the scattered light is scattered to angles larger than the total internal reflection angle of the $\mu\text{c-Si:H/ZnO:Al}$ interface. This light is very likely reflected back into the solar cell. As a result, the absorption of the incident light in the absorber layer of the solar cell is enhanced. Thus, nanostructures on Ag back contacts which carry LSPP resonances offer a great potential for light trapping in thin-film silicon solar cells. If the interaction between the nanostructures is neglected, the presented findings on isolated nanostructures on the Ag back contact of thin-film silicon solar cells can be used to calculate, in first approximation, the optical parameters like haze, absorptance and scattering angle distribution of stochastic arrangements of Ag nanostructures (see Chapter 7). It is important to note that the LSPP resonances are found to scatter a multiple of the irradiated light on the nanostructures cross-section. Thus, realistic stochastic surface coverages below 50% are sufficient to scatter almost all incident light at the rear side of the solar cell.

5.3 Light Scattering at Plasmonic Reflection Grating Back Contacts

Periodically arranged nanostructures on Ag back contacts form two-dimensional reflection gratings (see Figure 5.8). The scattering angles of these gratings are determined by discrete diffraction orders. The scattering centers of the reflection gratings are the plasmonic Ag nanostructures. For this reason, in this work, this device is called a *plasmonic reflection grating back contact*. In Figure 5.8 (a), the electric field of a plasmonic reflection grating back contact in the planes parallel and perpendicular to the polarization of the incident electromagnetic wave is presented. For the plane parallel to the polarization of the incident electromagnetic wave, strong enhancements of the electric field in the vicinity of the nanostructures indicate the plasmonic resonances at the hemispherical nanostructures of radius of 150 nm. The existence of the plasmonic resonances for these nanostructures has been extensively discussed in the previous sections.

In the case of a square lattice of the nanostructure array and normal incidence of the impinging light, the diffraction angles of the plasmonic reflection grating back contact are given by [78]:

$$\sin(\alpha) = \frac{N_{xy} \cdot \lambda}{p \cdot n_{\mu\text{c-Si:H}}} \quad \text{with } N_{xy} = \sqrt{m_x^2 + m_y^2} \quad \text{and } m_x, m_y = 0, \pm 1, \pm 2, \dots \quad (5.1)$$

where λ is the wavelength in air, p is the grating period, m_x and m_y are the diffraction orders, α is the diffraction angle relative to the surface normal direction and $n_{\mu\text{c-Si:H}}$ is the refractive index of $\mu\text{c-Si:H}$. Equation 5.1 indicates that, by varying the period of a grating, the scattering angle is changed, thus allowing the scattering angles at nanostructured Ag back contacts to be controlled. Figure 5.8 (b)-(e) shows the simulated absorptance, the specular reflectance and non-specular reflectance as well as normalized intensity distribution of scattered light in $\mu\text{c-Si:H}$ of square lattice Ag reflection gratings on the back contact of a thin-film silicon solar cell. The radius of the periodically arranged Ag nanostructures is 150 nm and the period is set to 400 nm and 600 nm. The nanostructured Ag back contacts are covered conformally by a 180 nm thick ZnO:Al layer and a $\mu\text{c-Si:H}$ half-space. In Figure 5.8 (d) and Figure 5.8 (e), it is shown that the plasmonic reflection grating back contacts under study scatter the incident light into the corresponding diffraction orders following Eq. (5.1). With increasing period, the scattering angles of the diffraction orders decrease and additional

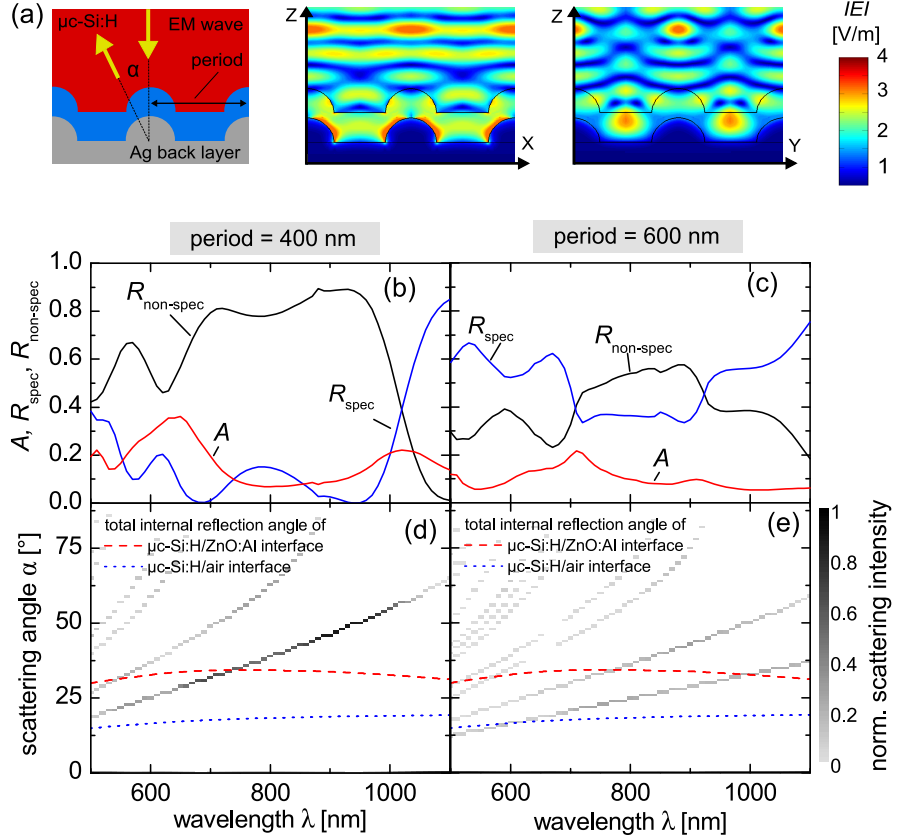


Figure 5.8: (a) Schematic cross-section of the plasmonic reflection grating back contact. The absolute electric field in the planes parallel and perpendicular to the polarization of the incident electromagnetic wave is shown (radius of hemispherical nanostructure 150 nm, ZnO:Al layer thickness of 180 nm, wavelength of 850 nm). Simulated absorptance (A), specular reflectance (R_{spec}) and non-specular reflectance ($R_{\text{non-spec}}$) of plasmonic reflection grating back contacts of square lattice period of (b) 400 nm and (c) 600 nm. (d) and (e) Corresponding normalized intensity distribution of scattered light at the plasmonic reflection grating back contacts. For comparison, the total internal reflection angle at a flat $\mu\text{c-Si:H/ZnO:Al}$ front interface (red dashed dotted line) and a flat $\mu\text{c-Si:H/air}$ front interface (blue dotted line) are shown.

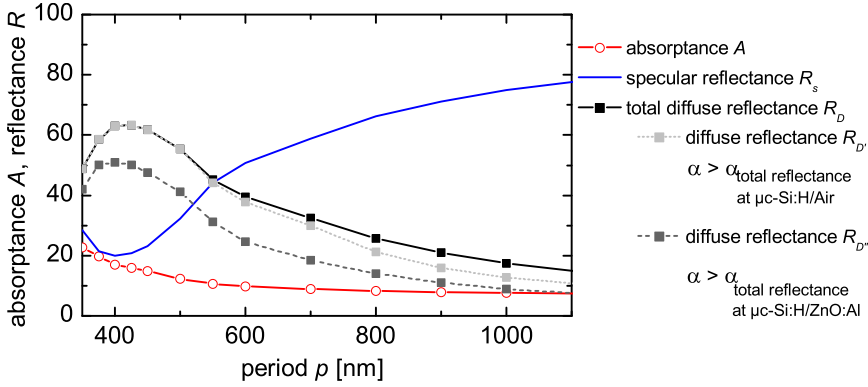


Figure 5.9: Simulated absorbance (A), specular reflectance (R_{spec}) and non-specular reflectance ($R_{\text{non-spec}}$) of plasmonic reflection grating back contacts (radius of 150 nm; ZnO:Al thickness of 180 nm). The data is averaged over the operational wavelength range of the back contact. The period of the plasmonic reflection grating back contact is varied from 350 nm to 1100 nm.

diffraction orders appear at shorter wavelengths. Thus, with regard to the application in solar cells, the advantage of smaller periods is the larger minimum scattering angle. For both periods studied in Figure 5.8, light scattering to angles below 11° is prohibited. However, only for a period of 400 nm, even scattering to angles smaller than the total internal reflection angle of the $\mu\text{c-Si:H/air}$ interface (blue dotted line) is prohibited in the operating spectral range of the back contact. For wavelengths longer than 750 nm, even scattering to angles smaller than the total internal reflection angle of the $\mu\text{c-Si:H/ZnO:Al}$ interface (red dashed line) is prohibited. In addition, the specular reflectance, which induces no light trapping, is reduced for the reflection grating with a period of 400 nm in comparison with a period of 600 nm. Thus, following the arguments on the scattering angles in $\mu\text{c-Si:H}$ presented in Section 5.1, all light scattered at the back contact with a lattice period of 400 nm is efficiently trapped in the $\mu\text{c-Si:H}$ absorber layer of the solar cell.

Variation of the Period of the Plasmonic Reflection Grating Back Contacts

In Figure 5.9, the simulated absorbance, specular reflectance and non-specular reflectance of various square lattice reflection gratings are shown. The values are averaged over the operating spectral range of the back contact in a $\mu\text{c-Si:H}$ thin-film solar cell. The optimal light-trapping texture is expected to exhibit the lowest losses, low-

est specular reflection and highest non-specular reflection to large angles (i.e., above the total internal reflection angle at the $\mu\text{c-Si:H/ZnO:Al}$ interface). For the studied geometry, this is fulfilled for periods of around 450 nm. For these periods, up to 63% and 50% of the incident light is scattered at the nanostructured Ag back contact to angles larger than the total internal reflection angle of the $\mu\text{c-Si:H/air}$ and the $\mu\text{c-Si:H/ZnO:Al}$ interface, respectively. Only 20% of the light is reflected specularly. For an isolated Ag nanostructure on the back contact of similar geometry (radius = 150 nm, ZnO:Al thickness = 180 nm), we find that 63% and 42% of the light is scattered to angles larger than the total internal reflection angle of the $\mu\text{c-Si:H/air}$ and the $\mu\text{c-Si:H/ZnO:Al}$ interface, respectively. Thus, comparing the isolated and periodic case, it is shown that the grating arrangement of the Ag nanostructures on the back contact increases the relative amount of light scattered to larger angles. This is particularly interesting, as one might expect that the dense arrangement of the nanostructures in the periodic case disturbs or attenuates the LSPP resonances.

5.4 Conclusion

In this chapter, LSPP-induced light scattering at nanostructured Ag back contacts of thin-film silicon solar cells was investigated numerically with a three-dimensional numerical solver of Maxwell's equations. Both, single nanostructures and reflection gratings formed by the arrangements of plasmonic Ag nanostructures in a square lattice on the back contact of a thin-film silicon solar cell were found to carry LSPP resonances. For both configurations, a large fraction of incident light is scattered at low optical losses. The calculated angular intensity distributions of the light scattered at nanostructured Ag back contacts show that a significant amount of the incident light is scattered into large angles in the $\mu\text{c-Si:H}$ absorber layer of the solar cell. Thus, nanostructured Ag back contacts carrying LSPP resonances are very promising for improving the light trapping in thin-film silicon solar cells. Very critical for the LSPP-induced scattering, and consequently the light trapping, are the geometrical parameters of the Ag nanostructures and the embedding dielectric materials. Throughout this study, various geometrical parameters of the nanostructures were varied and optimized with regard to the ability of the nanostructures to scatter incident light into large angles in the silicon absorber layers at low optical losses. Implementations of optimized Ag nanostructures are presented in the following chapters.

Chapter 6

Plasmon-Induced Optical Losses at Textured Ag Back Contacts

In order to trap incident light, state-of-the-art thin-film silicon solar cells employ random textures at their reflective back contacts and their transparent front contacts (see Section 3.2). Textured back contacts made of Ag yield a particularly good light scattering with regard to light trapping [160]. However, plasmon-induced optical losses at the surface of these back contacts are known to decrease their reflectance. Of particular interest are LSPP-induced optical losses which appear in nanostructures of the randomly textured surface of the Ag back contact. These LSPP-induced optical losses have not been considered in previous contributions to this problem [208–210]. In the first section, measured absorptance spectra of textured Ag back contacts embedded in various dielectrics are shown. The contribution of optical losses induced by either SPPs or LSPPs to the absorptance spectra of these back contacts is discussed. In the second section, the impact of the plasmon-induced losses on the performance of thin-film silicon solar cells is studied. The importance of a ZnO:Al interlayer of low refractive index between the silicon layers and the Ag back contact is demonstrated. Furthermore, the potential for increasing the reflection at the back contact by applying dielectric interlayers of refractive index lower than ZnO:Al is evaluated. Parts of the results presented in this chapter have been published previously [211–213].

6.1 Optical Losses at Textured Ag Surfaces

In order to study the plasmon-induced absorption of incident light at textured surfaces of Ag back contacts, the absorptance of optically thick Ag layers in contact with air or covered by SiO_2 and ZnO:Al are studied. The investigated Ag surfaces exhibit textures ranging from perfectly flat to the state-of-the-art random texture for light trapping in thin-film silicon solar cells.

6.1.1 Preparation of Textured Ag Surfaces

Four types of textured Ag surfaces were investigated (see Figure 6.1). The texture Type D is the reference texture of state-of-the-art thin-film silicon solar cells. It is prepared by depositing a 250 nm thick Ag layer on top of a ZnO:Al substrate which was wet-chemical etched for 40 s in a 0.5 (w/w)% HCl solution [45, 157]. After the etching, the surface texture is covered by crater-like features which induce a root means square roughness of 130 nm. The texture Type C is prepared in the same way, applying a shorter etching time of 5 s. Due to the shorter etching time, smaller and less surface features are formed, resulting in a smaller root mean square roughness of around 80 nm. The texture Type B is prepared by depositing a 250 nm thick Ag layer on top of a glass substrate. Due to the irregular growth of small Ag crystallites, the surface texture exhibits shallow features with a height in the ten nanometer range and lateral sizes up to around 100 nm [73]. These unintentional features lead to a small root mean square roughness of a few nanometers. The fourth Ag surface, Type A, is almost perfectly flat. It was prepared by template stripping a 250 nm thick Ag layer from a silicon wafer substrate. Due to the very conformal growth of the Ag at the silicon interface, the stripped Ag surface shows almost no surface roughness [73].

6.1.2 Discussion of Plasmon-Induced Optical Losses

In Figure 6.1 (b), Figure 6.1 (c) and Figure 6.1 (d), the absorptance spectra of Ag surfaces in contact with air or covered with SiO_2 and ZnO:Al are shown, respectively. The SiO_2 layer was prepared by thermal evaporation and the ZnO:Al layer was rf-sputtered. For all surface textures, except the flat Ag surface of Type A, distinct maxima in the absorptance are found at wavelengths of 345 nm, 370 nm and 430 nm for the Ag surface in direct contact with air and for the Ag surface covered with SiO_2

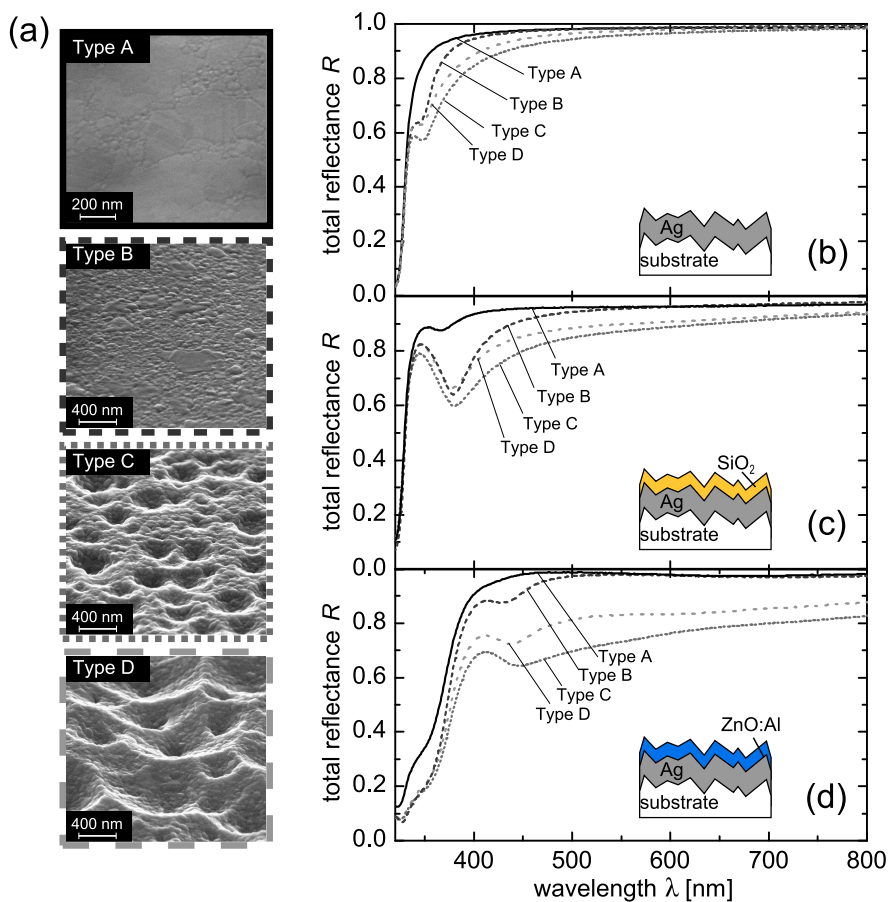


Figure 6.1: (a) Scanning electron microscopy images of the four Ag textures. Total absorbance (A) measured at Ag surfaces in air (b) and covered by 60 nm of SiO_2 (c) and 80 nm of ZnO:Al (d).

and ZnO:Al, respectively. These maxima are accompanied by an absorption tail that extends to longer wavelengths. For those Ag surfaces of rough texture (Type C and Type D) which are covered by ZnO:Al and SiO₂, the absorption tails extend significantly into the operational wavelength range of the back contact of thin-film silicon solar cells ($500 \text{ nm} < \lambda < 1100 \text{ nm}$), where a high reflectance is required. More general, a very strong dependence of the absorptance on the texture of the Ag surfaces is shown in Figure 6.1. In the following paragraphs the origin of this dependence is investigated. Optical losses induced by dissipative SPP modes at the dielectric/Ag interface and dissipative LSPP resonances at Ag nanostructures are discussed.

Propagating Surface Plasmon Polariton Resonance Propagating SPPs are electromagnetic eigenmodes which are bound to the interface of a metal and a dielectric (see Section 2.3). As illustrated in Figure 6.2 (a), the SPP modes propagate along the metal/dielectric interface with a wavevector ($k_{||}$) parallel to the interface. The impact of dissipative SPP modes at the randomly textured Ag surfaces on the absorptance is discussed in this section on the basis of the dispersion relations of the SPP eigenmodes at flat air/Ag, SiO₂/Ag, ZnO:Al/Ag and $\mu\text{c-Si:H/Ag}$ interfaces. The dispersion relations were calculated according to Eq. (2.16).

As light at normal incidence exhibits no component of the wavevector parallel to the Ag surface, the dispersion relation of incident light and SPP eigenmodes do not intersect (see Figure 6.2 (b)). For this reason, in order to allow a coupling of incident light and SPP modes at the Ag surface, an additional wavevector component ($\Delta k_{||}$) must be provided by diffraction at the grating components of the randomly textured Ag surface [84,85]. As shown in Figure 6.2 (b), at the resonance wavelength (λ_{SPP}), the density of suitable wavevector components ($\Delta k_{||}$) per wavelength interval is strongly enhanced. Thus, the excitation of propagating SPP modes is much more probable. Due to the damping of the SPP modes, the enhanced excitation of SPP modes leads to an enhanced absorptance of incident light at randomly textured Ag surfaces at λ_{SPP} [85,86]. From Eq. (2.16), the λ_{SPP} is determined to 340 nm, 364 nm and 415 nm for Ag surfaces in direct contact with air and for the Ag/SiO₂ and Ag/ZnO:Al layer stacks, respectively. Considering experimental variations in the optical data, the calculated λ_{SPP} correspond very well to the measured absorptance maxima at 345 nm, 370 nm and 430 nm for the Ag surface in direct contact with air and for the Ag surface covered with SiO₂ and ZnO:Al, respectively (see Figure 6.1). Thus, the spectral position of the maxima in absorptance of the randomly textured Ag surfaces can be explained by coupling of light to SPP modes at the randomly textured Ag surfaces.

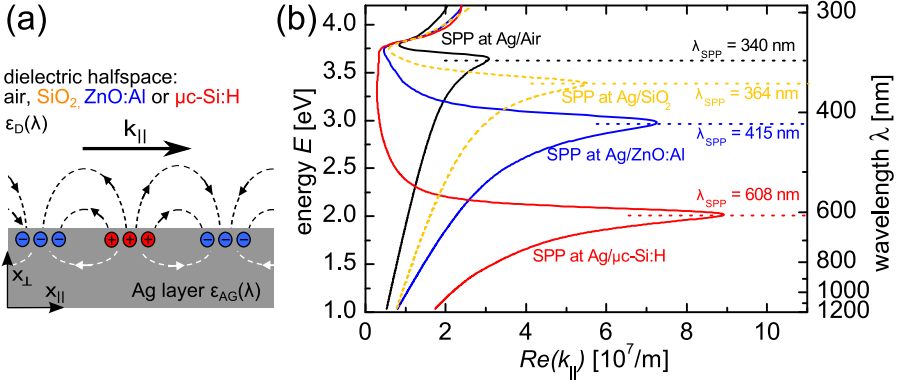


Figure 6.2: (a) Illustration of a SPP mode propagation along a flat Ag surface. (b) Calculated SPP dispersion relations of a flat Ag surface covered by air, ZnO:Al or $\mu\text{-Si:H}$. The energy E of the SPP modes is shown as a function of the real part of the wavevector parallel to the surface (k_{\parallel}).

From Figure 6.2 (b), the required maximum in Δk_{\parallel} at λ_{SPP} for the coupling of SPP modes to light at normal incidence can be derived. As for light of normal incidence k_{\parallel} is zero, the required maximum in Δk_{\parallel} at λ_{SPP} for the coupling is around $3 \cdot 10^7 \text{ m}^{-1}$ and $7 \cdot 10^7 \text{ m}^{-1}$ for the Ag surface in contact with air and embedded in ZnO:Al , respectively. Considering in first approximation a dominant coupling by light diffraction in the first order of grating components of the rough texture, this maximum Δk_{\parallel} can be converted into a lateral feature size of around 200 nm and 100 nm at the Ag surface in contact with air and embedded in ZnO:Al , respectively. Since such features are present for the texture Type B, Type C and Type D an enhanced absorption due to the excitation of SPP modes is possible (see Figure 6.2). For the flat Ag surface of Type A, almost no surface texture is present and almost no enhanced absorption at λ_{SPP} was measured (c.f. Figure 6.1 (b) to Figure 6.1 (d)). Thus, in addition to the spectral position of the measured absorption maxima presented in Figure 6.1, the dependence of these absorption maxima on the type of texture at the Ag surface can be explained well by light coupling to dissipative SPP modes.

The absorption maxima in Figure 6.1 are accompanied by an absorption tail that extends, for Ag surfaces embedded by ZnO:Al or SiO_2 , partly into the operational wavelength range of the back contact of thin-film silicon solar cells ($500 \text{ nm} < \lambda < 1100 \text{ nm}$). As discussed above, an excitation of SPP modes can

explain the enhanced parasitic absorption of light at λ_{SPP} . In the same way, for wavelengths of the absorption tail, a coupling of incident light to SPP modes is possible. However, due to the decrease of Δk_{\parallel} for the coupling of light and SPP modes at wavelengths longer than λ_{SPP} (see Figure 6.2 (b)), the maximum lateral size of the surface features required for the first-order light coupling increases to around 200 nm to 800 nm. Such large features are present for the Type C and Type D Ag surface which show also the largest absorptance for the above described absorption tails. As the density of suitable wavevectors per wavelength interval is decreased at the wavelengths of the absorption tail, a coupling to SPP modes is less probable in comparison to λ_{res} .

In conclusion, the excitation of dissipative SPP modes at randomly textured Ag surfaces can explain well the enhanced absorption presented in Figure 6.1 for the various Ag textures in air, covered by SiO_2 and covered by ZnO:Al .

Localized Surface Plasmon Polaritons An alternative explanation for the decreased absorptance of the randomly textured Ag surfaces presented in Figure 6.1 are LSPP-induced optical losses at small Ag nanostructures. In the previous Section 5.2, it was shown that LSPP resonances in small isolated Ag nanostructures induce a very strong absorption. In Figure 6.3, the simulated maximum values of the absorption efficiency ($\max. Q_{\text{abs}}$) at the dominant LSPP resonance of hemispherical Ag nanostructures embedded in air, SiO_2 , ZnO:Al and $\mu\text{c-Si:H}$ are shown. Values of $\max. Q_{\text{abs}}$ above unity indicate that the absorbed power of small Ag nanostructures of radius below 80 nm can be a multiple of the power irradiated on the nanostructures cross-section. A similar strong absorption at a variation of the resonance wavelength was observed also for other geometries of the nanostructures as well as coupled nanostructures [211, 214]. For this reason, considering the broad distribution of shapes, sizes and arrangements of Ag nanostructures at the randomly textured Ag surfaces shown in Figure 6.1 (a), LSPP-induced optical losses are expected to enhance significantly the absorptance at these Ag surfaces. Even for a comparably low surface coverage of Ag nanostructures the LSPP-induced optical losses result in an enhanced absorptance as the absorbed power by the nanostructure can exceed the power irradiated on its cross-section (see Figure 6.3). In particular, in the wavelength regions where an enhanced absorption tail was measured for the randomly textured Ag surfaces in direct contact with air or covered with SiO_2 and ZnO:Al , a particularly high LSPP-induced absorption for hemispherical Ag nanostructures was identified in Figure 6.3. It is important to note that the position of the LSPP resonances shifts to longer wavelengths with increasing refractive index of the dielectric in contact with

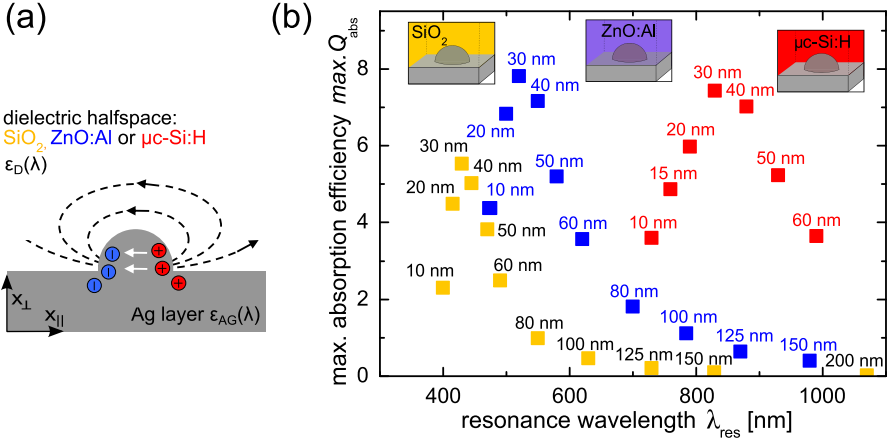


Figure 6.3: (a) Illustration of a LSPP mode in an hemispherical nanostructure on a flat Ag surface. (b) Maxima in simulated absorption efficiency ($\max. Q_{\text{abs}}$) of LSPP resonances in hemispherical Ag nanostructures as a function of the resonance wavelength (λ_{res}) covered by SiO_2 , ZnO:Al or $\mu\text{c-Si:H}$. The radius of the hemispherical nanostructure is varied from 10 nm to 200 nm.

Ag (from $n_{\text{air}} = 1$ to $n_{\text{SiO}_2} \approx 1.45$ and $n_{\text{ZnO:Al}} \approx 1.6-2.0$). In the case of $\mu\text{c-Si:H}$ as embedding material, the LSPP-induced decrease in absorptance is located in the center of the operational wavelength range of the back contact of thin-film silicon solar cells ($500 \text{ nm} < \lambda < 1100 \text{ nm}$).

Plasmonic Losses at Ag Back Contacts In the previous paragraphs, it was discussed that both LSPP resonances and SPP resonances can be excited by incident light on randomly textured Ag surfaces such as the Ag back contacts of thin-film silicon solar cells with the state-of-the-art random texture for light-trapping. The agreement of the calculated λ_{SPP} with the spectral position of the absorptance maxima of the randomly textured Ag surfaces indicates that these absorptance maxima are likely caused by SPP-induced optical losses. However, the enhanced absorption at longer wavelengths at the surface of Ag back contacts with the state-of-the-art random texture (Type D) can be explained both by LSPP-induced as well as SPP induced optical losses. For future studies it is suggested that the effect of LSPP and SPP-induced optical losses at the Ag surfaces can be separated by correlating the angular dependent absorptance of the surfaces to the dispersion relations of the SPP and LSPP modes. At

this stage, it is concluded that for incident light of wavelengths longer than 500 nm, both types of plasmonic effects can be responsible for the enhanced absorptance of strongly textured Ag back contacts (Type C and Type D) covered with SiO_2 , ZnO:Al and $\mu\text{c-Si:H}$. It was shown that, both, the SPP-induced optical losses and the LSPP-induced optical losses shift to shorter wavelengths with decreasing refractive index of the embedding material. Therefore, the highest reflection at textured Ag back contacts in thin-film silicon solar cells is expected for the lowest refractive index of the dielectric interlayer. In the following section this hypothesis will be tested in thin-film silicon solar cell devices.

6.2 Avoiding Plasmon-Induced Optical Losses at Ag Back Contacts

Relevance of the Dielectric Interlayers at Ag Back Contacts For thin-film silicon solar cells, highly reflective Ag back contacts are essential for good light trapping. An additional ZnO:Al interlayer between the thin-film silicon absorber layers and the Ag back contact is generally applied, as it strongly increases the reflectance for wavelengths longer than 500 nm where incident light reaches the back contact. In Figure 6.4, this effect is shown for a 1 μm thick $\mu\text{c-Si:H}$ solar cell in p-i-n configuration. The *EQE* of a solar cell under variation of the back contact is shown. For the first *EQE*, the solar cell was prepared with a 700 nm thick Ag back contact. Afterwards, the Ag back contact was removed by template stripping and a ZnO:Al/Ag back contact was deposited on exactly the same position. The ZnO:Al interlayer thickness is 80 nm. For wavelengths longer than 550 nm, the $\mu\text{c-Si:H}$ solar cell prepared with the ZnO/Ag back contact shows a strongly enhanced *EQE* when compared with the *EQE* measured on the same solar cell applying a Ag back contact. This effect is associated with an additional reflection at the $\mu\text{c-Si:H/ZnO:Al}$ interface as well as reduced plasmon-induced optical losses at textured ZnO:Al/Ag surfaces in comparison with $\mu\text{c-Si:H/Ag}$ surfaces (c.f. previous Section). In the case of a $\mu\text{c-Si:H/Ag}$ interface, both the SPP and LSPP-induced optical losses, which exist at textured Ag surfaces of Type D, are located in the operational wavelength range of the back contact ($500 \text{ nm} < \lambda < 1100 \text{ nm}$). For the $\mu\text{c-Si:H/ZnO/Ag}$ back contact layer stack, the SPP and LSPP-induced optical losses are shifted significantly to shorter wavelengths where less incident light reaches the back contact. The difference in *EQE* corres-

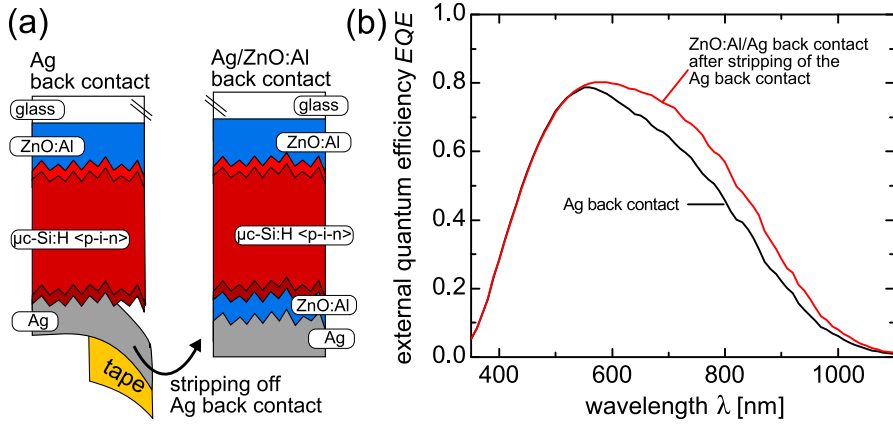


Figure 6.4: (a) Schematic cross-section of a μc -Si:H thin-film solar cell in p-i-n configuration with Ag back contact as well as ZnO:Al/Ag back contact. (b) External quantum efficiency (EQE) of the same μc -Si:H solar cell measured first with the Ag back contact and afterwards with the ZnO:Al/Ag back contact after stripping off the Ag back contact.

ponds to 2.0 mA/cm^2 in J_{sc} which is around 10% of the total J_{sc} . Thus, the dielectric interlayer between the silicon absorber layer of the solar cell and the Ag back contact is of high relevance.

Potential of Dielectric Interlayers of Low Refractive Index In Section 6.1.2, it was demonstrated that the SPP-induced and LSPP-induced optical losses at randomly textured Ag surfaces shift to shorter wavelengths with decreasing refractive index of the covering dielectric. In addition, the reflection at the μc -Si:H/dielectric interface at the rear side increases with decreasing refractive index. In order to assess the resulting potential for thin-film silicon solar cells, the EQE of μc -Si:H solar cells prepared with SiO_2 ($n_{\text{SiO}_2} \approx 1.45$) and air ($n_{\text{air}} = 1.0$) as interlayers between the Ag back contact and the μc -Si:H absorber layers are compared with co-deposited solar cells which apply a ZnO:Al interlayer (Figure 6.5). In order to allow the use of non-conductive dielectric interlayers such as SiO_2 and air, an n-doped μc -Si:H layer is applied in combination with local Ag contacts separated from each other by a few millimeters. Although the FF of these devices decreases strongly due to a reduced conductivity at the rear side of the solar cell, these devices allow a detailed optical analysis by measuring the EQE and the reflectance. In Figure 6.5 (a) and

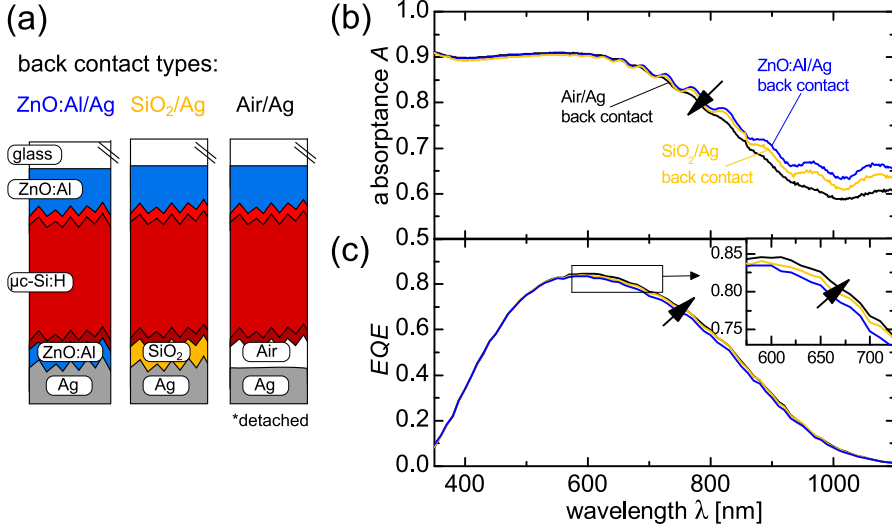


Figure 6.5: (a) Schematic cross-section of a $\mu\text{c-Si:H}$ thin-film solar cell in p-i-n configuration with ZnO:Al/Ag back contact, SiO_2 /Ag back contact and air/Ag back contact. (b) Absorptance (A) and (c) external quantum efficiency (EQE) of the $\mu\text{c-Si:H}$ solar cell with the three types of back contact.

Figure 6.5 (b), it is shown that the absorptance of the solar cells decreases strongly with decreasing refractive index of the interlayer. At the same time, the EQE of the solar cells prepared with a SiO_2 interlayer and an air interlayer is slightly increased when compared with the reference solar cell prepared with a ZnO/Ag back contact layer stack. The overall J_{sc} enhancement is 0.3 mA/cm^2 and 0.5 mA/cm^2 for the solar cell applying the SiO_2 interlayer and the air interlayer, respectively. In comparison with the total J_{sc} of 22.7 mA/cm^2 of the solar cell with the ZnO:Al interlayer, this increase is small and cannot compensate for the significantly lower electrical performance of the devices. Due to comparably low absorption of the $\mu\text{c-Si:H}$ material, for wavelengths longer than 550 nm , a significant portion of increased reflection of light at the back contact simply induced an enhanced reflectance of the total solar cell (see decreased absorptance in Figure 6.5 (b)).

6.3 Conclusion

In this chapter, the impact of plasmon-induced optical losses on the reflectance of textured Ag back contacts in thin-film silicon solar cells was investigated. First, the absorptance spectra of textured and flat Ag back contacts covered with various dielectrics were studied. Both, propagating SPPs as well as LSPPs were identified as possible sources for the optical losses at these textured Ag back contacts.

A particular focus was set on the discussion of LSPP-induced optical losses in nanostructures on the Ag back contact. These losses have not been considered in the literature to this problem. In this chapter, it is shown that even for a comparably low surface coverage of small hemispherical Ag nanostructures (radius < 100 nm), the LSPP-induced optical losses can decrease strongly the reflectance of textured Ag back contacts. Furthermore, the simulated wavelength range of LSPP-induced enhanced absorption matches the wavelength range of enhanced absorptance of the textured Ag back contacts covered with ZnO:Al, SiO₂ or air.

Most relevant for solar cells is the dependence of the LSPP-resonances and SPP-resonances at the textured Ag back contact on the refractive index of the embedding dielectric. It is shown that both resonances shift to shorter wavelengths with decreasing refractive index of the embedding dielectric. For this reason, in state-of-the-art solar cells, the plasmon-induced optical losses are shifted out of the relevant wavelength range by incorporating a ZnO:Al interlayer of low refractive between the silicon layers and the Ag back contact. The effect was demonstrated in this chapter for μ c-Si:H thin-film solar cell. Furthermore, the additional but small potential for increasing the reflection at the back contact with dielectric interlayers of even lower refractive index, such as SiO₂ and air, was demonstrated in solar cell devices.

Chapter 7

Plasmonic Back Contacts with Non-Ordered Ag Nanostructures

In this chapter, the light trapping in thin-film silicon solar cells which apply plasmonic back contacts with non-ordered Ag nanostructures is investigated. In the first section, the preparation, geometrical characterization as well as the reflectance spectra of Ag back contacts with various distributions of non-ordered Ag nanostructures are presented. In the second section, the measured reflectance spectra of the plasmonic back contacts in air are compared with reflectance spectra calculated from optical simulations of LSPP resonances in isolated nanostructures on Ag back contacts. Furthermore, based on optical simulations, the light scattering at plasmonic Ag back contacts into the $\mu\text{c-Si:H}$ layer of a thin-film silicon solar cell is evaluated with regard to light trapping. In the third section, the light trapping of $\mu\text{c-Si:H}$ solar cell prototypes in n-i-p configuration deposited on one of the most promising type of Ag back contact with non-ordered nanostructures is studied. Parts of the results, presented in this chapter, have previously been published in [215].

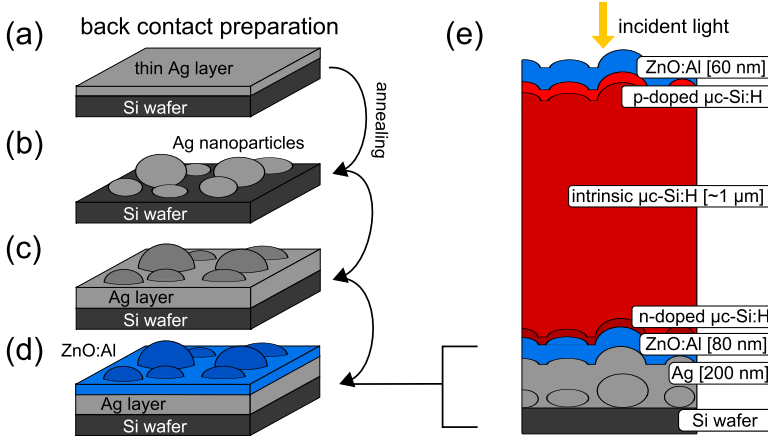


Figure 7.1: (a)-(d) Illustration of the preparation steps of the Ag back contacts with non-ordered nanostructures. (e) Schematic cross-section of a $\mu\text{c-Si:H}$ solar cell in n-i-p configuration deposited on a plasmonic back contact with non-ordered Ag nanostructures.

7.1 Preparation of Back Contacts with Non-Ordered Ag Nanostructures

In this section, the preparation of Ag back contacts with non-ordered Ag nanostructures is presented. The nanostructures on the Ag back contact were prepared by coating the Ag nanoparticles with a 200 nm thick dc-sputtered Ag layer and an 80 nm thick rf-sputtered ZnO:Al layer. The preparation steps from the Ag nanoparticles to the Ag back contacts with non-ordered nanostructures are shown in Figure 7.1 (a)-(d). The Ag back contacts are prepared for the subsequent deposition of a $\mu\text{c-Si:H}$ thin-film solar cell in n-i-p configuration (see Figure 7.1 (e)).

Nanoparticle Formation by the Annealing of Thin Ag Films Ag nanoparticle arrangements on silicon wafer substrates were prepared by the annealing of thermally evaporated Ag films (see Figure 7.1 (a)-(b)). The Ag films were annealed at a temperature of 500 °C for six hours in a nitrogen atmosphere. Due to the surface tension, the Ag films agglomerated into non-ordered arrangements of nanoparticles. In Figure 7.2, SEM images of Ag nanoparticle distributions are shown. The initial Ag film thickness is varied from 5 nm to 30 nm. It is observed that the average size of

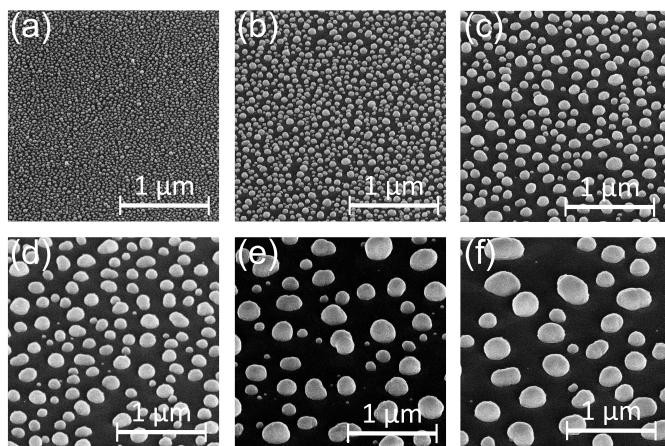


Figure 7.2: SEM images of Ag nanoparticles prepared by the annealing of thin Ag films. The thickness of the initial Ag film was 5 nm, 10 nm, 15 nm, 20 nm, 25 nm and 30 nm in (a)-(f), respectively.

the Ag nanoparticles increases gradually with increasing thickness of the initial Ag layer [216]. For initial Ag layer thicknesses larger than 25 nm, nanoparticles of radii above 100 nm are observed. Such radii are particularly important. The optical simulations of hemispherical nanostructures on Ag back contacts, presented in Chapter 5, point out that radii above 100 nm are needed for an efficient LSPP-induced light scattering at the back contact of thin-film silicon solar cells.

Ag Back Contacts with Non-Ordered Nanostructures For the back contact preparation, the silicon wafer substrates with the Ag nanoparticles were covered with a 200 nm thick dc-sputtered Ag layer and a 80 nm thick rf-sputtered ZnO:Al layer (see Figure 7.1 (c)-(d)). In Figure 7.3 (a)-(e), AFM images of the Ag back contact surface prior to the ZnO:Al deposition are shown for five types of nanostructure distributions on Ag back contacts. The five back contacts are referred to as Type A, Type B, Type C, Type D and Type E, respectively. They were prepared on non-ordered nanoparticle arrangements which were obtained by the annealing of Ag films of thickness of 10 nm, 15 nm, 20 nm, 30 nm and 40 nm. The AFM images show that the surface texture of the Ag back contacts prior to the ZnO:Al deposition reveals non-ordered nanostructures. These nanostructures are created by the conformal deposition of the

Ag layer onto the Ag nanoparticles. The average size of the nanostructures on the Ag back contact correlates to the average size of the Ag nanoparticles which, in turn, correlate with the initial thickness of the thin Ag film prior to the annealing step. In Figure 7.3 (f)-(j), the measured diffuse and total reflectance spectra of the five types of back contacts in air are shown. With increasing average size of the nanostructures, the diffuse reflectance increases from the Type A back contact to the Type E back contact. In addition, the wavelength range of enhanced diffuse reflectance shifts to longer wavelengths. For example, the maximum in diffuse reflectance is 45% at a wavelength of 586 nm for the back contacts of Type B and 55% at a wavelength of 765 nm for the back contacts of Type D.

7.2 Optical Simulation of the Back Contacts

In the previous section it was shown that non-ordered nanostructures on Ag back contacts in air induce a size-dependent diffuse reflectance spectrum. A similar size-dependent increase of scattering efficiency as well as a size-dependent increase of the LSPP resonance wavelength was described in the previous Section 5.2 for LSPP-induced light scattering at isolated hemispherical Ag nanostructures. In this section, this correlation is investigated in more detail. The light scattering of five types of plasmonic back contacts with non-ordered Ag nanostructures is studied with three-dimensional electromagnetic simulations. In the first part, simulated diffuse and total reflectance spectra calculated from optical simulations of isolated nanostructures on Ag back contacts in air are compared with measured reflectance spectra. In the second part, the simulated reflectance spectra of the Ag back contacts with non-ordered nanostructures within μc -Si:H thin-film solar cells are presented. Furthermore, the five types of back contacts are evaluated regarding their ability to scatter incident light at low optical losses into large angles in the μc -Si:H absorber layers of the thin-film silicon solar cells.

7.2.1 Reflectance of the Back Contacts in Air

The measured diffuse and total reflectance spectra of the nanostructured back contacts with non-ordered Ag nanostructures are compared with simulated reflectance spectra. The optical simulations were performed with the three-dimensional electromagnetic solver introduced in Section 2.4.3. Due to the required high resolution of the simula-

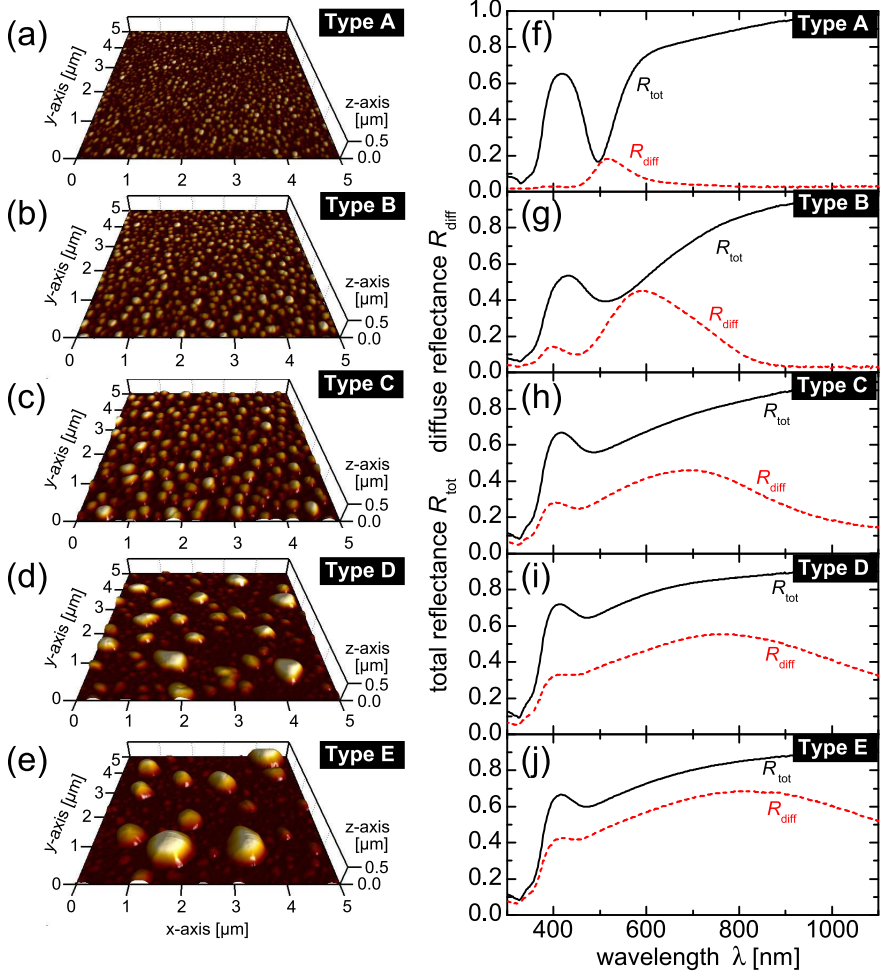


Figure 7.3: (a)-(e) AFM images of five types of plasmonic back contacts with non-ordered Ag nanostructures. (f)-(j) Total reflectance (R_{tot}) and diffuse reflectance (R_{diff}) of plasmonic back contacts with non-ordered Ag nanostructures.

tion grid at metal surfaces, it is not possible to simulate a representative surface area of the plasmonic Ag back contacts with non-regular Ag nanostructures in a single simulation. Instead, the simulated reflectance spectra of the plasmonic back contacts with Ag surfaces were calculated as an area weighted superposition of the simulated reflectance spectra of isolated nanostructures on Ag back contacts.

Shape and Size Distribution of the Nanostructures on the Back Contact In order to allow an in-depth analysis of the LSPP-induced light scattering at the various distributions of nanostructures on the five types of back contacts, a detailed analysis of the shape and size distribution of the nanostructures was performed. The AFM images of the five back contacts were analyzed with the Advanced Threshold Algorithm of the Particle and Pore Analysis module of the SPIP software, version 5.1.6 (Image Metrology A/S, Horsholm, Denmark) [71]. The detection level for the algorithm was set to the mean level of plane-fitted AFM data. It is important to note that the choice of detected level is a sensitive setting. For this reason, the results and trends presented in this chapter, which are based on the detected nanostructure distribution, have been verified for other detection levels of the nanostructure distribution. From the detected nanostructure distribution, the area-weighted base radius and the corresponding height of the nanostructures was derived for each of the five types of the plasmonic back contacts. Additionally, in order to stabilize the detection algorithm and to avoid the inclusion of very small and shallow nanostructures, those nanostructures with an height to radius aspect ratio below 0.5 and a radius below 3 nm have been excluded. In Figure 7.4 (a), the detected area-weighted base radius distributions of the five types of back contact are shown. A continuous increase of the base radius of the nanostructures is presented for increasing average radius of the underlying Ag nanoparticles which corresponds to an increasing initial thickness of the thin Ag film prior to the annealing step. A very broad range of nanostructure distributions exists for the various types of back contacts. For the Type A back contact, which was deposited on the smallest Ag nanoparticles, the maximum of the base radius distribution is located around 30 nm. For the Type E back contact, which is deposited on the largest Ag nanoparticles, the maximum in base radius distribution is located around 530 nm. In addition, Figure 7.4 (b) shows the height of each nanostructure plotted against the base radius for the nanostructures detected from the AFM images. For all types of back contact, the height to radius aspect ratio of the nanostructures is located around 0.75 (indicated by the dashed line). Thus, for future analysis, it is reasonable to approximate the nanostructures by half-ellipsoids of height to base radius aspect ratio of 0.75.

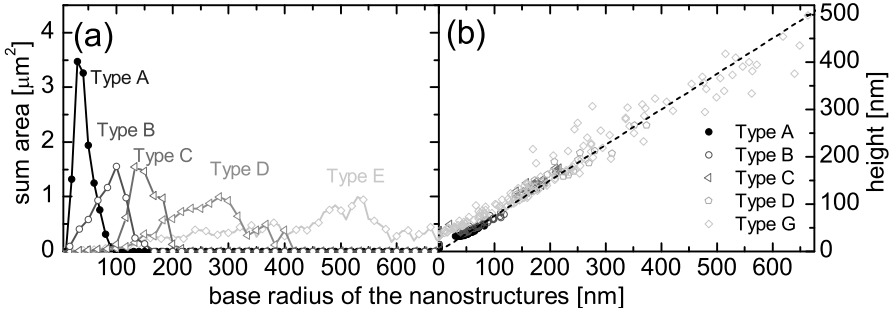


Figure 7.4: (a) Area-weighted base radius distribution (sum area) and (b) height as a function of the radius of each nanostructure derived from the AFM images of five types of Ag back contacts with non-ordered nanostructures (presented in Figure 7.3 (a)-(e)).

Plasmonic Light Scattering of Isolated Half-Ellipsoidal Nanostructures on Ag Back Contacts Covered by 80 nm of ZnO:Al in Air

In the previous section, it was shown that the five types of Ag back contacts with non-ordered Ag nanostructures exhibit half-ellipsoidal nanostructures of various base radius distributions (see Figure 7.4). In order to represent these nanostructures, optical simulations of isolated half-ellipsoidal nanostructures on Ag back contacts were performed under variation of the base radius from 10 nm to 700 nm. The half-ellipsoidal nanostructures are covered by ZnO:Al and the height to base radius ratio was set to 0.75. A schematic cross-section of the structure is shown in the inset in Figure 7.5. In Figure 7.5 (a) and Figure 7.5 (b), the scattering efficiency and absorption efficiency are shown for wavelengths from 300 nm to 1100 nm. Values of Q_{sca} and Q_{abs} above unity indicate the appearance of LSPP resonances. For small radii, only a dipolar LSPP resonance is exhibited, which shifts to longer wavelengths with increasing base radius of the nanostructures. For radii smaller than 50 nm, the Q_{abs} dominates and for wavelengths larger than 50 nm, the Q_{sca} clearly dominates. For radii from 10 nm to 100 nm, the maximum in Q_{sca} increases and for larger radii, it decreases gradually while additional multipolar LSPP resonances appear at shorter wavelengths. In addition, with increasing radius, the LSPP resonances shift to longer wavelengths. Overall, the identified radius-dependent trends of the simulated Q_{sca} and Q_{abs} are similar to the trends of hemispherical Ag nanostructures embedded in a ZnO:Al half-space (see Section 5.2).

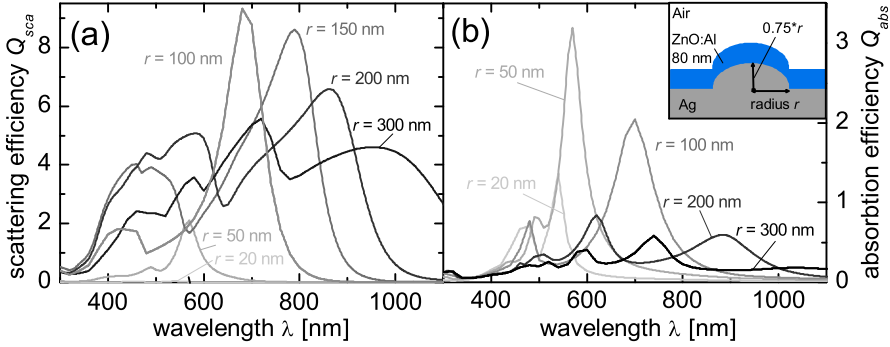


Figure 7.5: (a) Simulated scattering efficiency (Q_{sca}) and (b) absorption efficiency (Q_{abs}) of isolated ellipsoidal Ag nanostructures on Ag surfaces covered by an 80 nm thick ZnO:Al layer. The radius of the nanostructure is varied from 20 nm to 300 nm and the height is set to 75% of the corresponding radius.

Simulated Reflectance Spectra vs. Measured Reflectance Spectra of Back Contacts with Non-Ordered Plasmonic Nanostructures in Air

In order to derive the diffuse reflectance and the total reflectance spectra from the above presented simulations, the simulated spectra of Q_{sca} and Q_{abs} of the half-ellipsoidal nanostructures were weighted with an area-weighted base radius distribution of each type of plasmonic back contact (c.f. Figure 7.3 and Figure 7.3). The resulting simulated diffuse reflectance spectra are shown for wavelengths from 300 nm to 1100 nm in Figure 7.6 (a). For comparison, the measured diffuse reflectance spectra of the five types of Ag back contacts are replotted in Figure 7.6 (c). It is shown that both the simulated and measured diffuse reflectance spectra increase gradually over the total wavelength range with increasing average base radius of the nanostructures on the back contacts (indicated by the arrow). The shift of the maxima of the measured diffuse reflectance to longer wavelengths with increasing base radius of the nanostructures is reproduced in the simulated data. Since the simulated diffuse reflectance spectra are calculated from spectra of LSPP resonances, the enhanced diffuse reflectance of the Ag back contact is attributed to an enhanced LSPP-induced scattering of incident light at the nanostructures. Furthermore, the simulated shift of the LSPP-induced light scattering with increasing radius of the Ag nanostructure correlates well with the shift of the measured diffuse reflectance maxima to longer wavelengths (see Figure 7.5). The deviation in the total values of the measured and simulated diffuse reflectance as well

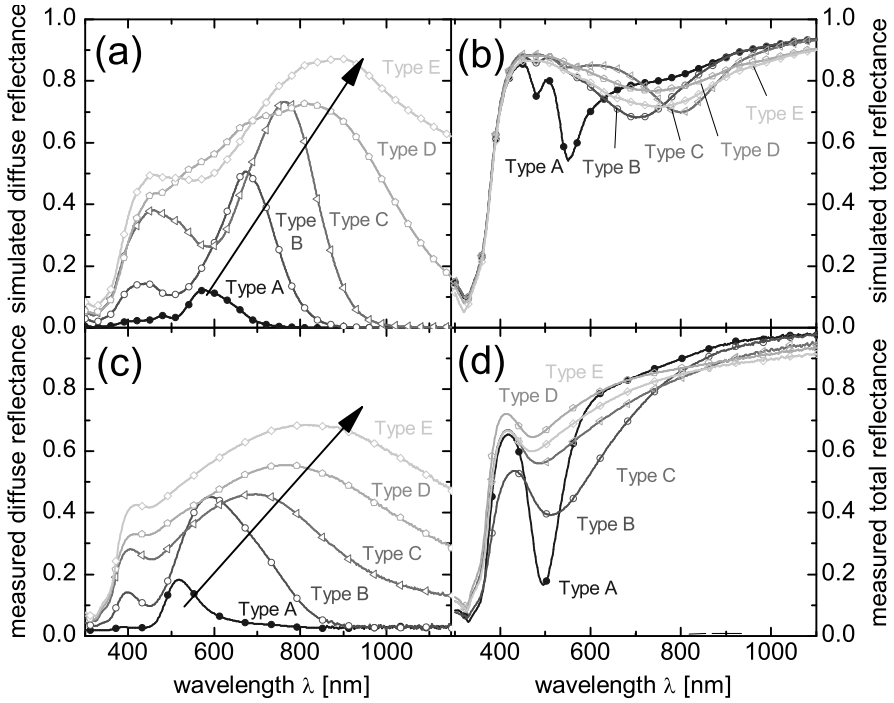


Figure 7.6: (a) Simulated diffuse reflectance, (b) simulated total reflectance, (c) measured diffuse reflectance and (d) measured total reflectance of five types of Ag back contacts with various distributions of non-ordered nanostructures.

as the redshift of the simulated spectra are attributed to the strong simplifications applied to derive the simulated diffuse reflectance spectra. Of particular relevance in this regard are the strong assumptions regarding the shape of the nanostructures and the neglected coupling between adjacent nanostructures.

The simulated and measured total reflectance of the five types of Ag back contacts with non-ordered nanostructures are shown in Figure 7.6 (b) and Figure 7.6 (d), respectively. For all measured total reflectance spectra, a prominent minimum is located at wavelengths around 500 nm. In addition, these minima exhibit an absorption tail that ranges into the long wavelength range. With increasing average base radius of the nanostructures of the five types of back contact (from Type A to Type E) the minimum at wavelengths around 500 nm decreases in the measured data. For the simulated total

reflectance spectra, this minimum is only weakly pronounced for the Type A, Type B and Type C back contact where it is shifted to longer wavelengths. The corresponding deviation between simulated and measured total reflectance is attributed to the fact that the SPP-induced optical losses are underrated in the simulated total reflectance spectra. In fact, the simulated total reflectance spectra are derived from simulations of isolated half-ellipsoidal Ag nanostructures. For isolated Ag nanostructures, a very efficient coupling of light to LSPs was shown (see Figure 7.5). However, the coupling of incident light to SPPs is not efficient. Thus, the SPP-induced optical losses for textured Ag surfaces covered by ZnO:Al at wavelengths between 400 nm and 550 nm (see Section 6.1.2) are not considered in the simulated total reflectance spectra.

7.2.2 Light Scattering into the $\mu\text{c-Si:H}$ Absorber Layer

The diffuse reflectance spectra and angular scattering intensity distributions of Ag back contacts with non-ordered nanostructures within $\mu\text{c-Si:H}$ thin-film solar cells are to be determined for the understanding of the light-trapping effect. Since it is not possible to measure the scattering angles or scattering intensity of scattered light within the $\mu\text{c-Si:H}$ absorber layer itself, three-dimensional electromagnetic simulations were applied. Due to the reasonable agreement between measured and simulated diffuse reflectance of the plasmonic back contacts in air, it is expected that the simulations of Ag back contacts within the $\mu\text{c-Si:H}$ absorber layer provide realistic scattering and diffuse reflectance.

Similar to the previous section, the simulated Q_{sca} and the angular scattering intensity distributions of isolated Ag nanostructures on Ag back contacts are weighted with the area-weighted base radius distribution of each type of plasmonic back contact (presented in Figure 7.4 (a)). The simulated half-ellipsoidal Ag nanostructures are covered with an 80 nm thick ZnO:Al layer and a $\mu\text{c-Si:H}$ half-space, representing the layer stack at the rear side of a $\mu\text{c-Si:H}$ thin-film solar cell (c.f. Figure 7.1 (e)). The height to radius aspect ratio of the nanostructure is 0.75.

Simulated Diffuse Reflectance Spectra of Back Contacts with Non-Ordered Plasmonic Nanostructures Covered with 80 nm ZnO:Al in $\mu\text{c-Si:H}$

In Figure 7.7, the simulated diffuse reflectance spectra of the five types of plasmonic Ag back contacts with non-ordered plasmonic nanostructures are shown for wavelengths from 300 nm to 1100 nm. It is observed that the diffuse reflectance increases over the total wavelength range with increasing average base radius of the nanostructures. The av-

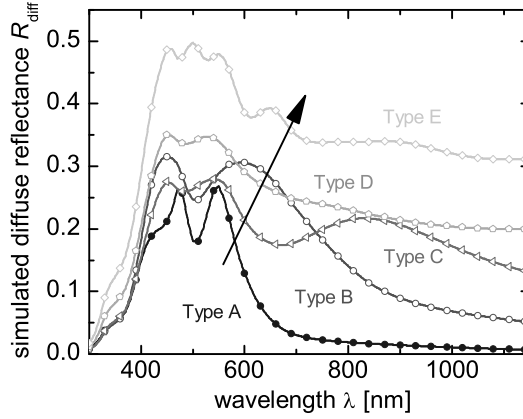


Figure 7.7: Simulated diffuse reflectance of the five types of Ag back contacts at the rear side of a thin-film silicon solar cell.

erage base radius is smallest for the Type A back contact and largest for the Type E back contact (see Figure 7.4 (a)). Aside from the Type A back contact, incident light is scattered within the total operational wavelength range of the back contact of a $\mu\text{c-Si:H}$ thin-film solar cell ($500 \text{ nm} < \lambda < 1100 \text{ nm}$). The Type A back contact and the Type B back contact exhibit Ag nanostructures of radii smaller than 150 nm (c.f. Figure 7.4). For these radii, the LSPP-induced light scattering at half-ellipsoidal Ag nanostructures covered by ZnO:Al exists only for wavelengths smaller than 900 nm (c.f. Figure 7.5 (a)).

Similar to the diffuse reflectance spectra of the plasmonic Ag back contacts in air (c.f. Section 7.2.1), the highest diffuse reflectance is found for the Type D back contact and the Type E back contact. However, the absolute values of simulated diffuse reflectance of the plasmonic back contacts covered by the $\mu\text{c-Si:H}$ layer are much smaller than those in air. In Section 5.2.4, it was shown that the dielectric layer stack at the rear side of the $\mu\text{c-Si:H}$ solar cell, i.e. the thickness of the ZnO:Al layer, strongly influences the Q_{sca} of half-spherical nanostructures on Ag back contacts. In particular, for ZnO:Al thicknesses of around 80 nm, the Q_{sca} was strongly reduced for wavelengths between 700 nm and 1100 nm in comparison with larger ZnO:Al thicknesses. It shall be noted that the evaluation of the diffuse reflectance of plasmonic Ag back contacts in air can be very misleading. The diffuse reflectance and scattering angle distribution, which are determined by LSPP-induced light scatter-

ing, strongly depend on the dielectric material in the vicinity of the nanostructures (see Section 5.2). As a result, the simulated diffuse reflectance of the back contacts in a thin-film silicon solar cell is strongly reduced when compared with the diffuse reflectance simulated for the back contacts in air (c.f. Figure 7.6 (a) and Figure 7.7).

Simulated Angular Scattering Intensity Distribution of Ag Back Contacts with Non-Ordered Nanostructures

In Section 5.1, it was shown that an efficient light trapping via plasmonic back contacts requires the scattering of incident light into large angles in the $\mu\text{c-Si:H}$ absorber layer of $\mu\text{c-Si:H}$ thin-film solar cells. From the simulated data, the angular scattering intensity distribution of the Ag back contacts with non-ordered Ag nanostructures is evaluated. To give an example, in Figure 7.8 (a), the normalized scattering intensity distribution of light scattered at the Type D back contact is shown as a function of the scattering angle in the $\mu\text{c-Si:H}$ layer and the wavelength. The considered wavelength range is set to the operating spectral range of the back contact ($500 \text{ nm} < \lambda < 1100 \text{ nm}$). It is shown that the incident light at the back contact is scattered into a broad angle distribution in the $\mu\text{c-Si:H}$ absorber layer of the thin-film silicon solar cell (see Figure 7.8 (a)). A substantial amount of the scattered light is scattered to large angles. In order to compare the light scattering at the five types of plasmonic Ag back contacts with non-ordered Ag nanostructures, in Figure 7.8, the average absorption, diffuse reflectance and specular reflectance are shown for the five types of back contacts with non-ordered nanostructures. The fractions of the diffusively reflected light which are scattered beyond the total internal reflection angle of a flat $\mu\text{c-Si:H/ZnO:Al}$ interface and a flat $\mu\text{c-Si:H/air}$ interface are given. The data was averaged over the operational wavelength range of the back contact in a $\mu\text{c-Si:H}$ thin-film solar cell ($500 \text{ nm} < \lambda < 1100 \text{ nm}$). For all back contacts investigated, a large amount of incident light is reflected specularly. This is an indication for a low light trapping in solar cells with these back contacts. The amount of diffusively reflected light at the back contacts increases from the Type A back contact to the Type E back contact. Moreover, the amount of incident light which is scattered beyond the critical total internal reflection angles at a flat $\mu\text{c-Si:H/air}$ or $\mu\text{c-Si:H/ZnO:Al}$ interface, increases from the Type A back contact to the Type E back contact. Consequently, we expect the best light trapping for the back contact of Type E and Type D. To give an example, for the Type D back contact 24% of the incident light are reflected diffusively, whereof 15% and 10% of the incident light are scattered to angles beyond the total internal reflection angle of a flat $\mu\text{c-Si:H/air}$ and $\mu\text{c-Si:H/ZnO:Al}$ interface, respectively. Thus, the relative amount of diffusively reflected light which is reflected to large angles is significant. Nevertheless, due to

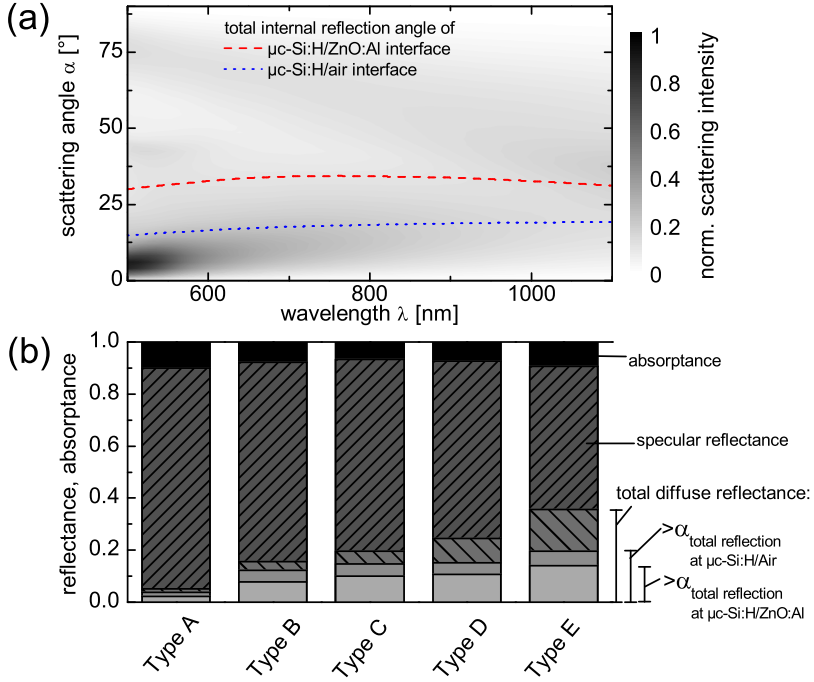


Figure 7.8: (a) Angular scattering intensity distribution into $\mu\text{c-Si:H}$ of the Type D Ag back contact with non-ordered nanostructures. (b) Simulated diffuse reflectance of the Type D back contact. Total diffuse reflectance and the fraction thereof indicating the amount of the light scattered beyond the total internal reflection angle of a flat $\mu\text{c-Si:H/ZnO:Al}$ interface and a flat $\mu\text{c-Si:H/air}$ interface.

the low total diffuse reflectance, it is shown that the overall light trapping of the solar cells with the five back contacts with non-ordered Ag nanostructures is low.

Simulated Absorptance of Ag Back Contacts with Non-Ordered Nanostructures

In addition to the specular and diffuse reflection, the average absorptance of incident light in the five types of plasmonic Ag back contacts with non-ordered Ag nanostructures is shown in Figure 7.8 (b). While the fraction of diffusively reflected light is smallest for the Type A back contact, the average absorptance is maximal for this back contact. Due to the small radius of the Ag nanostructures at the Type A back contact, the LSPR resonances in these nanostructures induce strong absorption losses

as explained in Section 5.2. For nanostructures of radii smaller than around 80 nm which are mostly existent for the Type A back contact, the highest values of Q_{abs} are shown in Figure 7.6 (b). With increasing radius of the nanostructures on the back contacts, the absorptance decreases from the Type A back contact to the Type C back contact. As the radius of the nanostructures on these types of back contacts increases, the Q_{abs} of these nanostructures decreases (see Section 5.2). For the Type D and Type E back contacts, the absorptance increases with respect to the Type C back contact. These back contacts are most promising for light trapping as they exhibit the highest diffuse reflection. The increase in absorption of the Type D and Type E back contact is attributed to the increase in surface coverage of nanostructures on these back contacts as well as the appearance of absorptive multipolar resonances for radii larger than 150 nm at wavelengths larger than 500 nm.

7.3 Prototype $\mu\text{c-Si:H}$ Thin-Film Solar Cell

The light trapping of $\mu\text{c-Si:H}$ solar cells in n-i-p configuration deposited on the Type D Ag back contact with non-ordered nanostructures is studied. The Type D back contact exhibits an average nanostructure base radius of around 300 nm and a strongly enhanced diffuse reflectance for wavelengths longer than 500 nm. For these wavelengths incident light reaches the rear side of a thin-film silicon solar cell (see Figure 7.7). An approximately 1.1 μm thick $\mu\text{c-Si:H}$ solar cell in n-i-p configuration was deposited by plasma enhanced chemical vapor deposition on the Type D Ag back contact and, for comparison, on a flat back contact and a randomly textured Ag back contact. For details on the preparation of the solar cells and the randomly textured back contact, see Section 2.1.1 and [45]. A schematic cross-section of the complete solar cell design is shown in Figure 7.1 (e). All solar cells shown here were deposited in the same deposition run.

In Figure 7.9 (a), the measured EQE spectra of the three $\mu\text{c-Si:H}$ solar cells deposited on the flat back contact, the random texture back contact, and the Type D Ag back contact with non-ordered nanostructures are shown. For wavelengths from 520 nm to 1100 nm, the EQE of the solar cell deposited on the Type D back contact is significantly enhanced in comparison with the EQE of the solar cell deposited on the flat back contact. This enhancement shows that due to LSPP-induced light scattering at the Ag back contact with non-ordered nanostructures, a substantial amount of incident light is guided inside the $\mu\text{c-Si:H}$ absorber layer of the solar cell. This leads to

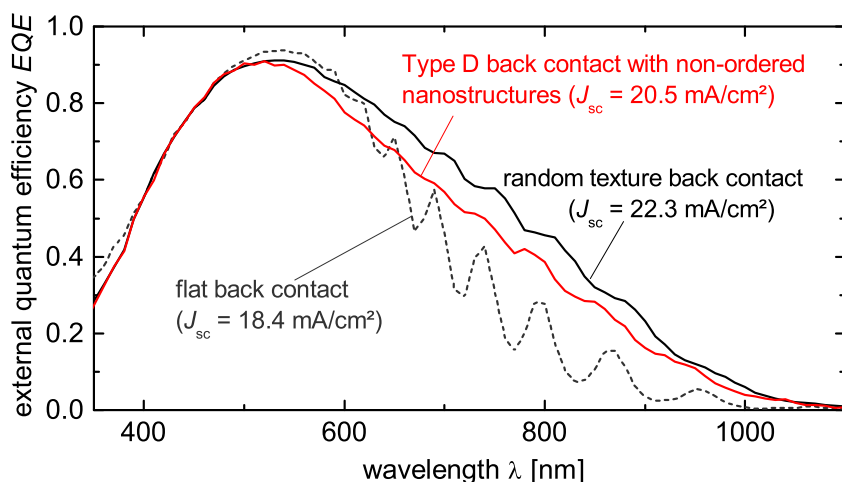


Figure 7.9: External quantum efficiency (EQE) of three $\mu\text{c-Si:H}$ solar cells in n-i-p configuration codeposited on the flat back contact, the random texture back contact, and the Type D back contact with non-ordered Ag nanostructures.

an enhanced generation of charge carriers and, in turn, an enhancement of J_{sc} from 18.4 mA/cm^2 to 20.5 mA/cm^2 . However, the EQE as well as J_{sc} of the solar cell applying the state-of-the-art random texture for light trapping is even larger. Thus, for the given nanostructure distributions at the Type D back contact, the light trapping is not competitive with the state-of-the-art texture for light trapping. Similar results have been reported in the literature for textured Ag back contacts [181, 216]. However, in this study very regular shapes of nanostructures have been investigated which allowed an in-depth analysis of the LSPP-induced light scattering. Most important, for the first time, it was shown that the enhanced diffuse reflectance of the Ag back contacts in air correlates well to LSPP-induced light scattering at the non-ordered Ag nanostructures. The low light-trapping effect of the solar cells with Ag back contacts with non-ordered nanostructures is attributed to the low diffuse reflectance of incident light at the Type D back contact into the $\mu\text{c-Si:H}$ absorber layer of the solar cell (c.f. Section 7.2.2).

7.4 Conclusion

In this chapter, the light trapping of plasmonic back contacts with non-ordered Ag nanostructures in a $\mu\text{c-Si:H}$ thin-film solar cell prototype was studied. A simple way of fabricating non-ordered plasmonic nanostructures on Ag back contacts was presented. Non-ordered Ag nanoparticles, which were prepared via thermally-induced agglomeration of Ag films, were coated with a Ag layer and an 80 nm thick ZnO:Al layer. Back contacts with various Ag nanostructure distributions were prepared. Their Ag nanostructures exhibited half-ellipsoidal shape with base radii between 10 nm and 700 nm.

Three-dimensional electromagnetic simulations were applied to study the reflectance spectra of five types of Ag back contacts with non-ordered nanostructures. Measured reflectance spectra of the back contacts in air were compared with reflectance spectra calculated from optical simulations of LSPP resonances in isolated nanostructures on Ag back contacts. Due to a qualitatively good agreement between the measured and simulated reflectance spectra of the various types of Ag back contacts with non-ordered nanostructures, the enhanced diffuse reflectance of the back contacts was attributed to LSPP-induced light scattering at the nanostructures on the back contact. In addition, based on optical simulations, the light scattering at the plasmonic Ag back contacts into the $\mu\text{c-Si:H}$ absorber layer of a thin-film silicon solar cell was discussed. The diffuse reflectance of the plasmonic back contacts covered with $\mu\text{c-Si:H}$ was below 35% for all types of realized back contacts.

A $\mu\text{c-Si:H}$ solar cell in n-i-p configuration fabricated on one type of plasmonic Ag back contact showed a significantly enhanced *EQE* for wavelengths longer than 500 nm when compared with a flat solar cell. The corresponding light-trapping effect was attributed to LSPP-induced light scattering at nanostructures on the back contact. However, in comparison with the random texture back contacts, the light trapping produced by the Ag back contact with non-ordered nanostructures was low. Most probably due to the low diffuse reflection of light at the Ag back contacts with non-ordered nanostructures, the overall light trapping was low. Based on future simulation-based optimizations of the shape, size as well as embedding layer stack of the Ag nanostructures, an additional improvement potential of the light-trapping effect should be researched.

Chapter 8

Plasmonic Reflection Grating Back Contacts

This chapter reports on the prototyping and the optical simulation of $\mu\text{c-Si:H}$ thin-film solar cells applying plasmonic reflection grating back contacts. The plasmonic reflection grating back contacts are formed by Ag nanostructures which are arranged in a square lattice at the back contact of the solar cell. In the first section, the electrical and optical characteristics of prototype $\mu\text{c-Si:H}$ solar cells deposited on the plasmonic reflection grating back contacts are compared with reference solar cells deposited on flat back contacts and on randomly textured back contacts. Based on the optical simulations of plasmonic reflection grating back contacts, the light trapping is explained from the perspective of geometrical optics. In the second section, full three-dimensional electromagnetic simulations of entire solar cell prototypes applying plasmonic reflection grating back contacts are presented. An excellent agreement between simulated and measured spectral response of the prototype solar cells is presented. This agreement allowed a simulation based optimization of the geometric parameters of the plasmonic reflection grating back contact. In the last section, the light-trapping effect caused by the plasmonic reflection grating back contact is explained from the perspective of leaky waveguides. Parts of the results presented in this chapter have previously been published in [173, 217].

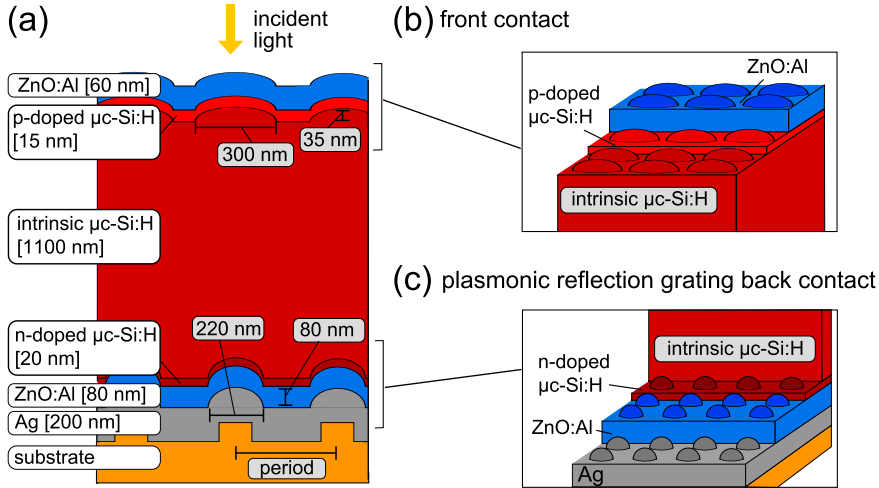


Figure 8.1: (a) Schematic cross-section of $\mu\text{c-Si:H}$ type solar cells in n-i-p configuration deposited on a plasmonic reflection grating back contact. The three-dimensional layer stack of the front contact and reflection grating back contact is shown schematically in (b) and (c), respectively.

8.1 Prototype $\mu\text{c-Si:H}$ Thin-Film Solar Cell

In order to demonstrate the light trapping caused by plasmonic reflection grating back contacts, $\mu\text{c-Si:H}$ solar cells in n-i-p configuration with an active cell area of 0.25 cm^2 were fabricated (see Figure 8.1). The performance of the solar cells deposited on a flat reference substrate, a randomly textured substrate and nano-imprinted patterned substrates with square lattice arranged nano-cubes are compared. The flat solar cell serves as a reference solar cell without light trapping. The solar cell deposited on the randomly textured back contact is the best reference solar cell which applies the state-of-the-art random texture for light trapping (see Section 3.2 and [45, 158, 160]).

8.1.1 Back Contact and Solar Cell Preparation

Preparation of the Plasmonic Reflection Grating Back Contact The patterned substrates with square lattice arranged nano-cubes are formed by a nanoim-

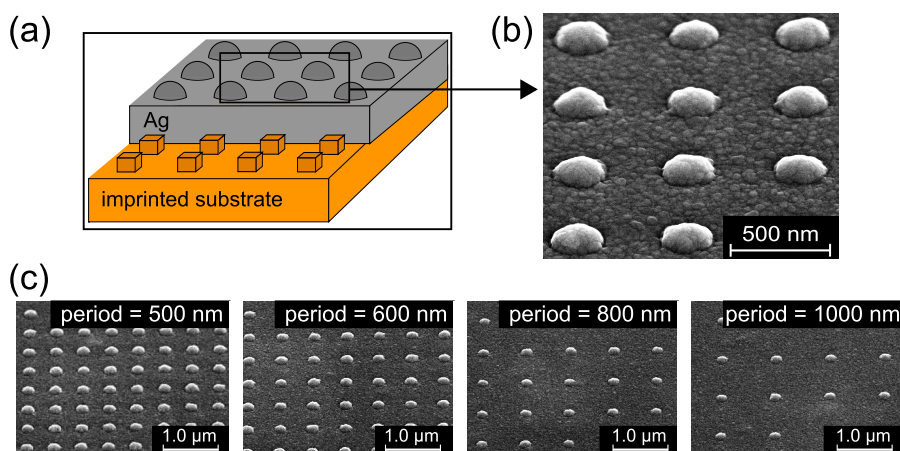


Figure 8.2: (a) Schematic figure of the nanoimprinted substrate with square lattice arranged cubic nanostructures as well as the Ag surface. (b)-(c) Scanning electron microscopy image of the surfaces of the plasmonic reflection gratings of various periods.

print process using a soft polymer mold (see Section 4). On top of the substrates, a 200 nm thick Ag layer and a 80 nm (± 5 nm) thick ZnO:Al layer was deposited at room temperature by rf-sputtering. Due to the nearly conformal deposition of Ag, the Ag surface reveals half-ellipsoidal nanostructures of radii of around 110 nm and height of around 80 nm, forming the plasmonic reflection grating back contact surface. In Figure 8.2, the Ag surface of the plasmonic reflection grating back contacts prior to the deposition of the ZnO:Al is shown for various periods. For the reference solar cells, a flat Ag/ZnO:Al back contact and a Ag/ZnO:Al back contact with the state-of-the-art random texture for light trapping was prepared. The reference substrate with the randomly textured back contact was prepared by wet-chemical etching of rf-sputtered ZnO:Al for 40 s in 0.5 w/w% HCl, resulting in a root mean square roughness of 139 nm (see Section 3.2).

Preparation of $\mu\text{c-Si:H}$ Thin Film Solar Cell On top of the three types of back contacts, a $\mu\text{c-Si:H}$ thin-film solar cell in n-i-p configuration was deposited by plasma enhanced chemical vapor deposition (for details see Section 2.1.1) The thicknesses of the n-doped, intrinsic and p-doped $\mu\text{c-Si:H}$ layer are around 15 nm (± 5 nm),

1100 nm (± 20 nm) and 20 nm (± 5 nm), respectively. As front contact, an approximately 60 nm to 70 nm thick ZnO:Al layer in combination with Ag finger electrodes were deposited. A schematic cross-section of the complete solar cell is shown in Figure 8.1. The geometrical data therein is taken from scanning electron microscopy images of the solar cell cross-section (prepared by focused ion beam) as well as atomic force microscopy measurements of the interfaces in between different preparation steps. Due to the non-conformal growth of the $\mu\text{c-Si:H}$ layers, the nanostructure of the substrate is leveled and broadened significantly at the front side of the solar cell. Thus, instead of protrusions of radius of 110 nm and height of 80 nm, at the front side of the solar cell the periodic half-ellipsoidal structures have a radius of around 300 nm and height of around 35 nm.

8.1.2 Results of the Prototype Solar Cells

External Quantum Efficiency and Short-Circuit Current Density In Figure 8.3 (a), the measured *EQE* spectra of the three $\mu\text{c-Si:H}$ solar cells deposited in the same conditions on a flat back contact, a back contact with the state-of-the-art random texture for light trapping, and a plasmonic reflection grating back contact with square lattice period of 500 nm are shown. For wavelengths from 550 nm to 950 nm, the *EQE* of the solar cell deposited on the plasmonic reflection grating back contact is significantly enhanced in comparison with the *EQE* of the solar cell deposited on the flat back contact. This enhancement shows that the plasmonic reflection grating back contact is capable of guiding a substantial amount of incident light inside the $\mu\text{c-Si:H}$ absorber layer of the solar cell, leading to an enhanced generation of charge carriers. This corresponds to a J_{sc} enhancement from 17.7 mA/cm² to 21.0 mA/cm². As a comparison, the highest J_{sc} measured at a reference solar cell deposited on the randomly textured back contact is only 20.8 mA/cm². Particularly in the wavelength range from 580 nm to 800 nm, the solar cell applying the plasmonic reflection grating back contact exhibits a strongly enhanced averaged *EQE* which indicates an enhanced light trapping in comparison with the solar cell applying the state-of-the-art random texture.

A qualitatively similar enhancement in *EQE* as described for the plasmonic reflection grating period of 500 nm was found for plasmonic reflection grating back contact of larger periods of 600 nm, 800 nm and 1000 nm. In Table 8.1, the corresponding J_{sc} are shown. The largest enhancement of J_{sc} for the given solar cell structures is found for a period of 500 nm. Only for this period, an enhancement of J_{sc} in compar-

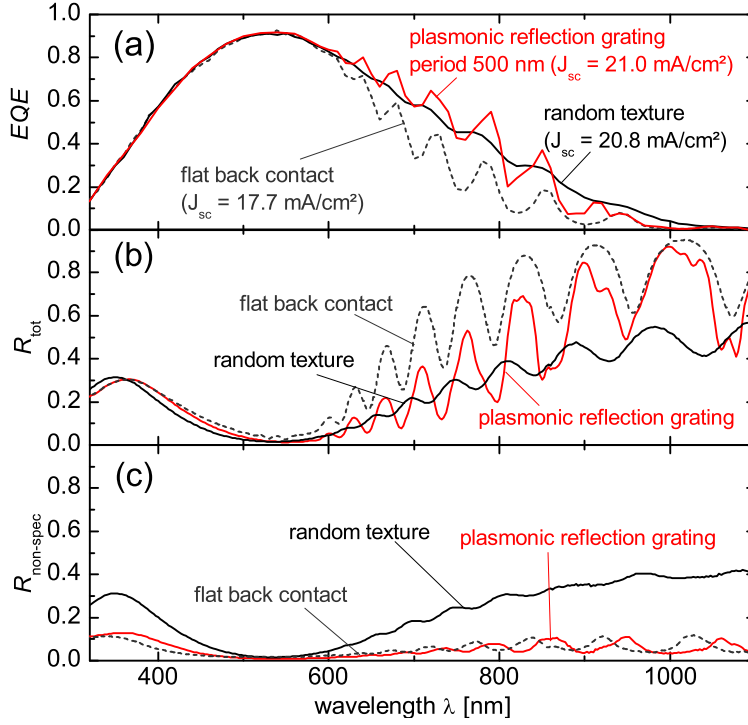


Figure 8.3: (a) External quantum efficiency (EQE), (b) total reflectance (R_{tot}) and (c) non-specular reflectance ($R_{\text{non-spec}}$) of $\mu\text{c-Si:H}$ solar cells in n-i-p configuration applying a flat back contact, a back contact with the state-of-the-art random texture for light trapping and a plasmonic reflection grating back contact (period of 500 nm).

ison with the solar cells deposited in the same conditions on the back contact with the state-of-the-art random texture for light trapping is observed. With increasing period, the measured J_{sc} decreases. This decrease is attributed to two reasons. First, the surface coverage of the scattering Ag nanostructures decreases with increasing period. Second, the angles of the diffraction orders of the plasmonic reflection grating decrease with increasing period, resulting in less efficient light trapping. This trend has been described in detail in Section 5.3.

Reflectance In order to investigate the light trapping in the solar cells deposited on the plasmonic reflection grating back contact and the randomly textured back

contact, the measured total and non-specular reflectance of the corresponding solar cells are compared in Figure 8.3 (b) and Figure 8.3 (c), respectively. For the solar cell deposited on the randomly textured back contact, most of the reflected light is diffusively reflected. For this solar cell, the light trapping is caused by light scattering at the randomly textured interfaces into broad angle distributions in the μc -Si:H absorber layer. Consequently, the *EQE* exhibits much less pronounced interference fringes than the flat solar cell and the light reflected from the solar cell is mostly reflected diffusively (i.e., the light is reflected non-specularly). In contrast, the light reflected at the solar cell deposited on the plasmonic reflection grating back contact is mostly reflected specularly. Similar to the flat solar cell, the *EQE* exhibits well-pronounced interference for wavelengths larger than 500 nm. In conclusion, the *EQE* and reflectance clearly show that the light trapping effect caused by the plasmonic reflection grating back contact differs conceptually from the light trapping effect caused by random textures.

Open-Circuit Voltage and Fill Factor Although the interest in plasmonic reflection grating back contact has arisen primarily from the light trapping effect and possible enhancement of J_{sc} , it needs to be ensured that the other solar cell parameters are not affected. Other than the J_{sc} , the *FF* and the V_{oc} are directly proportional to the efficiency of a solar cell. A substrate dependent change in the growth of the μc -Si:H material that affects in particular the *FF* and V_{oc} was reported in the literature [202, 203]. In Table 8.1, all solar cell parameters for the solar cells investigated in this section are shown. The flat reference solar cell and the solar cell deposited on the plasmonic reflection grating back contact have been co-deposited. Due to the very similar V_{oc} of these solar cells, it is evidenced that the electric characteristics and, in turn, the material properties of the μc -Si:H absorber layer of these solar cells are comparable. This has been confirmed additionally by Raman measurements which showed very similar crystallinities for the μc -Si:H materials. The differences in the surfaces of the flat and plasmonic reflection grating back contacts are small, as the nanostructures are flat when compared with the randomly textured back contact. For this reason, the growth and material quality of the μc -Si:H layers is comparable in the solar cell deposited on the flat back contact and plasmonic reflection grating back contacts. However, for the reference solar cell deposited on the randomly texture back contact, the V_{oc} is enhanced by around 15 mV. This enhancement of V_{oc} can be observed for all reference solar cells. It is expected that the growth of the μc -Si:H material on the back contacts differs for the random texture and the flat texture of the back contact. This results in a change of V_{oc} of the solar cell [202, 203].

Several of the solar cells deposited on the plasmonic reflection grating back contact suffer from shunts and, in turn, a decreased shunt resistance. As a result, for most of the solar cells deposited on the plasmonic reflection grating back contact, the FF is decreased in comparison with the flat solar cell. However, for the solar cell deposited on the plasmonic reflection grating of a period of 500 nm, a similar FF is observed as measured for the flat reference solar cell. In conclusion, the electrical properties of the solar cells deposited on the plasmonic reflection gratings did not deteriorate significantly. $\mu\text{c-Si:H}$ solar cells with enhanced J_{sc} , high FF and high V_{oc} on plasmonic reflection grating back contacts were prepared.

Reproducibility of the Results All trends and outcomes of solar cell prototypes presented in this subsection have been verified in two independent series of $\mu\text{c-Si:H}$ solar cells. In order to avoid an overestimation of the light trapping caused by the plasmonic reflection grating back contact, the EQE and J_{sc} shown in this chapter are compared with the best results measured for solar cells with a back contact with the state-of-the-art random texture for light trapping (deposited at the same conditions).

type of back contact	plasmonic reflection grating with period:				flat	random texture
	500 nm	600 nm	800 nm	1000 nm		
J_{sc} [mA/cm ²]	21.0	19.9	18.66	18.28	17.7	20.8
V_{oc} [mV]	486	485	481	487	486	498
FF	0.715	0.658	0.661	0.639	0.714	0.696

Table 8.1: Short-circuit current density (J_{sc}), open-circuit voltage (V_{oc}) and fill factor (FF) of $\mu\text{c-Si:H}$ solar cells in n-i-p configuration with integrated plasmonic reflection grating back contacts of various periods and for comparison with a flat back contact and a back contact with the state-of-the-art random texture for light trapping.

8.1.3 Geometrical Optics Perspective on the Light-Trapping Effect

In Figure 8.4 (a) and in Figure 8.4 (b), SEM images of cross-sections of the two solar cells deposited on a back contact with the state-of-the-art random texture for light trapping and a plasmonic reflection grating back contact of period of 500 nm are shown, respectively. The cross-sections have been prepared with a focused ion beam. Due to the material dependent interaction of the incident electron beam with the specimen, the SEM images show a layer dependent material contrast. From the

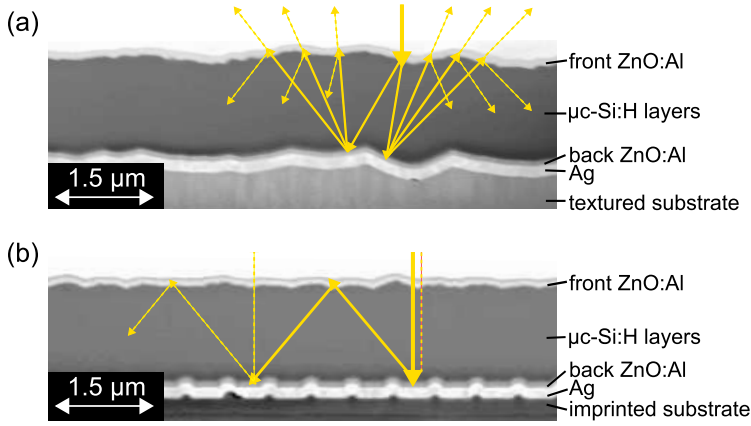


Figure 8.4: Scanning electron microscopy image of a cross-section of $\mu\text{c-Si:H}$ solar cells in n-i-p configuration applying (a) a back contact with the state-of-the-art random texture for light trapping and (b) a plasmonic reflection grating back contact (period of 500 nm). The cross-section was prepared by focused ion beam. In addition, the light propagation in the solar cell is illustrated.

cross-section images, two-dimensional information on the growth of the solar cell layers on the different types of back contact is derived. Comparing the solar cell deposited on the randomly textured back contact and the plasmonic reflection grating back contact, the difference in the geometrical structure is observed. The Ag nanostructures of the plasmonic reflection grating back contact are arranged periodically and they are relatively small compared with the large structures of the randomly textured back contact.

Light Propagation in the Prototype Solar Cells In Figure 8.4, the light propagation is illustrated by light rays for both types of solar cells. Although near-field effects are a constitutive element of light-scattering interfaces in the solar cells under study, it is possible to explain the fundamentals of the light trapping by light propagation in the solar cell with geometrical optics. For the solar cells deposited on the randomly textured back contact, light trapping is caused by the scattering of incident light off the randomly textured interfaces into broad angle distributions in the $\mu\text{c-Si:H}$ absorber layer [160]. The light scattering occurs both at the front and back contact of the solar cell resulting in a light path enhancement in the $\mu\text{c-Si:H}$ absorber layer of

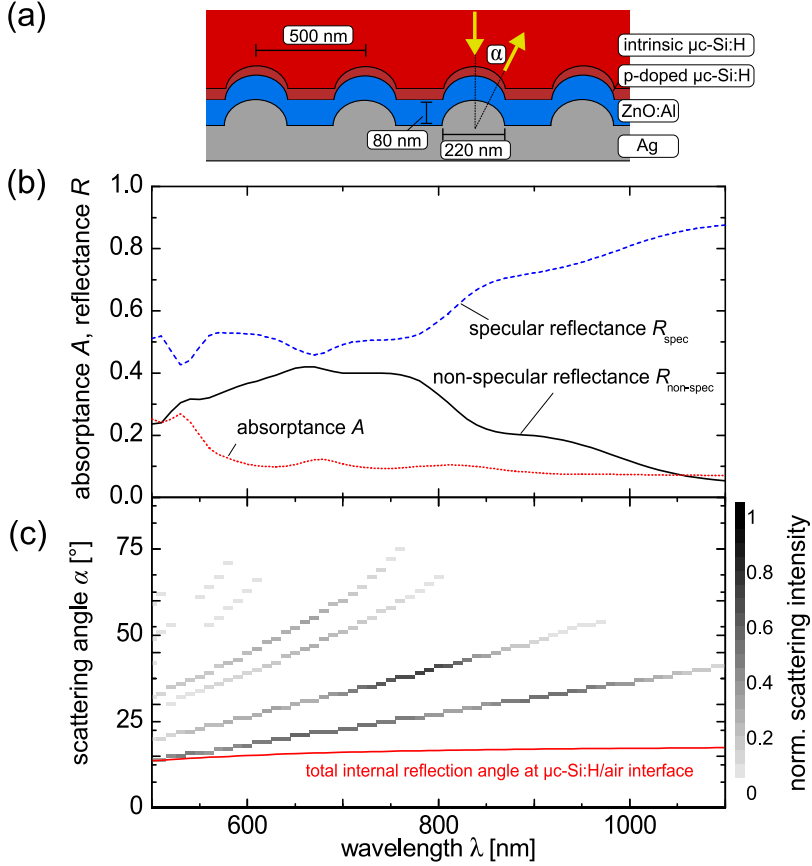


Figure 8.5: (a) Schematic cross-section of the simulated layer stack representing the plasmonic reflection grating back contact. (b) Non-specular reflectance ($R_{\text{non-spec}}$), specular reflectance (R_{spec}) and absorbance (A) calculated from three-dimensional simulations of the plasmonic reflection grating back contact. (c) Scattering intensity distribution of the diffracted light at the plasmonic reflection grating as a function of the scattering angle and the wavelength. Light scattered beyond the total internal reflection angle of $\mu\text{c-Si:H}$ /air (red line) will be reflected totally at a perfectly flat front side of the solar cell.

the solar cell. As a result, the EQE and, in turn, the J_{sc} of the solar cell are enhanced. For the solar cell deposited on the plasmonic reflection grating, only a small portion of incident light is scattered at the front interface. Light trapping in these devices is exhibited by the scattering of incident light at the plasmonic reflection grating back contact. In Section 5.3, it was shown that plasmonic reflection gratings diffracts incident light with high efficiency at the back contact of a thin-film silicon solar cell into large angles in the silicon absorber layers. These simulations have been repeated for the geometry realized in the prototype under study.

In Figure 8.5, the simulated absorptance, specular reflectance and non-specular reflectance as well as the simulated scattering intensity distribution of the non-specularly reflected light of the plasmonic reflection grating back contact in the above investigated prototypes is shown. The period is set to 500 nm. Figure 8.5 (b) shows that in the entire wavelength range of interest from 500 nm to 1100 nm, a substantial amount of incident light at the back contact is reflected non-specularly. This non-specularly reflected light is diffracted into diffraction orders of the grating. In particular, for wavelengths between 580 nm and 800 nm more than 35% of incident light is reflected non-specularly and the absorption at the back contact is less than 12% for all wavelengths. In the same spectral range, the solar cell applying the plasmonic reflection grating back contact exhibits an enhanced EQE in comparison with the solar cell applying the state-of-the-art random texture (see Figure 8.3 (a)). Due to the grating, the scattering angles of the back contact are defined by the diffraction orders. In Figure 8.5 (c), the normalized scattering intensity into these diffraction orders is shown as a function of the wavelength and scattering angle. For wavelengths longer than 500 nm, the minimum scattering angles of all diffraction orders are larger than the total reflection angle of a flat μc -Si:H/air interface.

As a result, the light path of the light scattered into the diffraction orders in the intrinsic μc -Si:H layer of a thin-film silicon solar cell is enhanced twofold. First, the light path is simply enhanced by the scattering angle. Second, considering the nearly flat front interface of the solar cell, incident light which is diffracted at the plasmonic reflection grating back contact to angles beyond the angle of total reflection of the μc -Si:H/air interface will be reflected totally at the front side. The resulting enhanced light path leads to an enhanced EQE and J_{sc} . Furthermore, due to the reciprocity of all light paths, such light reflected totally at the front side will be either reflected or diffracted antiparallel to normal incidence at its second incidence on the plasmonic reflection grating back contact (see Figure 8.4). For this reason, the reflected and reemitted light from the solar cell deposited on a plasmonic reflection back contact

must be specular. This finding correlates well with the measured reflectance spectra of both types of solar cells, shown in Figure 8.3. For the solar cells deposited on the plasmonic reflection grating back contact almost no non-specular reflectance is found, which is in contrast to the state-of-the-art light trapping.

8.2 Optical Simulations of the Solar Cells

In the previous section, prototypes of $\mu\text{c-Si:H}$ solar cells in n-i-p configuration applying plasmonic reflection grating back contacts were shown. An introduction into the simulation method was presented in Section 2.4.2. In this section, full three-dimensional electromagnetic simulations of entire solar cell prototypes applying plasmonic reflection grating back contacts are presented. An excellent agreement between simulated and measured spectral response of the prototype solar cells is presented. This agreement allowed a simulation based optimization of the geometric parameters of the plasmonic reflection grating back contact.

8.2.1 Optical Simulations of the Prototype Solar Cells

Two types of $\mu\text{c-Si:H}$ prototype solar cells in n-i-p configuration are simulated: (i) flat solar cells and (ii) solar cells applying plasmonic reflection grating back contacts. Cross-sections of these solar cell designs are shown in Figure 8.6 (a) and Figure 8.6 (d), respectively. The geometrical data therein is taken from the prototype preparation, SEM images of the prototypes cross-sections as well as AFM measurements of the interfaces in between different preparation steps of the solar cell. Within the geometrical uncertainties described in Section 8.1.1, the layer thicknesses have been set such that the simulated *EQE* fits best to the experimental *EQE* of the flat solar cell.

In order to illustrate the simulated electric field, the absolute electric field is given in a cross-section of a solar cell applying a flat back contact in Figure 8.6 (b)-(c) and a plasmonic reflection grating back contact of 500 nm period in Figure 8.6 (e)-(f). For both solar cells, the absolute electric field is shown in a plane parallel and a plane perpendicular to the polarization of the incident electromagnetic wave at normal incidence. This electromagnetic wave is polarized parallel to the grating vector of the square lattice unit cell of the plasmonic reflection grating back contact. It has a wavelength of 720 nm and an electric field strength of 1 V/m. For the flat solar cell

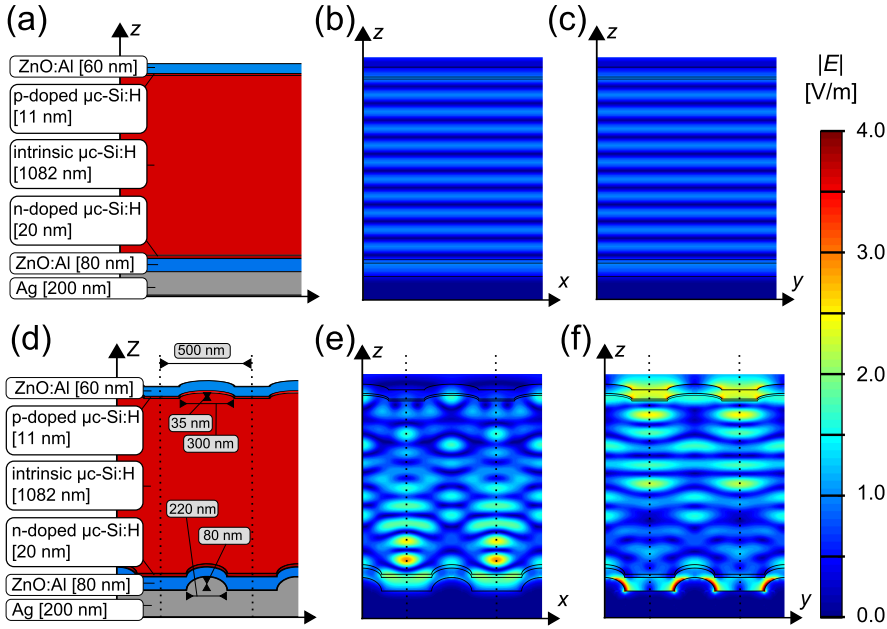


Figure 8.6: Schematic cross-section of the $\mu\text{c-Si:H}$ solar cell deposited on (a) a flat back contact and (d) a plasmonic reflection grating back contact of 500 nm period. Simulated absolute electric field in the plane perpendicular and the plane parallel to the polarization of the incident electromagnetic wave in (b),(c) and (e),(f), respectively. The incident electromagnetic wave has a wavelength of 720 nm and is polarized parallel to the grating vector of the square lattice unit cell of the grating.

the electric field is identical in both planes. It is solely determined by the Fabry-Perot interferences created by the dielectric layer stack of the solar cell and the highly reflecting Ag back contact. In contrast, for the solar cells deposited on the plasmonic reflection grating back contact, the electric field exhibits a three dimensional pattern due to the diffraction of incident light at the grating. It shall be noted that for the plane parallel to the polarization of the incident light, the enhanced electric-fields in the vicinity of the nanostructure indicate the LSPP resonance of the nanostructure (see Section 5.3 and Section 5.1). As expected, for the plane perpendicular to the polarization of the incident electromagnetic wave, this enhancement of the electric

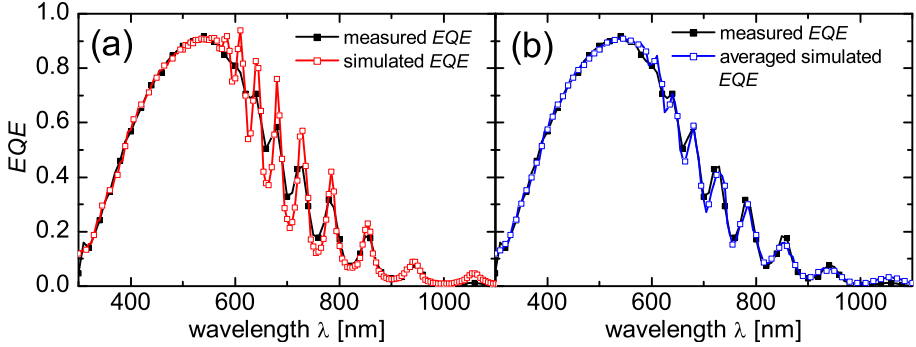


Figure 8.7: Simulated (red or blue line, open squares) and measured (black line) external quantum efficiency (EQE) of a μc -Si:H solar cell in n-i-p configuration deposited on a flat substrate. (a) The simulated EQE is shown for a single solar cell layer stack. (b) The simulated EQE is shown for a simple moving average with a final resolution of 10 nm of three solar cell layer stacks. The intrinsic μc -Si:H layer thickness of 1082 nm is varied by ± 25 nm.

field is not existing as the plasmonic resonance oscillates in plane with the exciting electric field of the incident electromagnetic wave.

Simulated vs. Measured EQE of the Flat Solar Cell The external quantum efficiency of the solar cells is calculated from the three-dimensional layer specific absorption profiles assuming a perfect collection of the generated charge carriers in the intrinsic μc -Si:H layer and collection efficiency of 50% in the n-doped μc -Si:H layer. In Figure 8.7 (a), the simulated EQE data of a single flat μc -Si:H solar cell is compared with experimental EQE data. The data is shown for wavelengths from 300 nm to 1100 nm. A very good agreement between the experimental EQE and the simulation of a single solar cell is shown for the EQE in the wavelength range from 300 nm to 550 nm. For longer wavelengths, due to the lower absorption in μc -Si:H, incident light reaches the back contact and interferences appear in the EQE due to the flat solar cell layer stack. In the simulated data, only the spectral position of the interferences is comparable with the experimental EQE . The modulation depth of the interferences in the simulated EQE data strongly exceeds the modulation depth of the interferences in the experimentally measured EQE . There are three reasons for this deviation: Firstly, the spectral resolution of the EQE measurement setup used

in this work is around 10 nm (see Section 2.1.3). Thus, the very steep modulations of bandwidth of similar size than the resolution of the measurement setup can not be resolved accurately. Secondly, the deposition of the dielectric layers in the $\mu\text{c-Si:H}$ solar cell layer stack is inhomogeneous. As the maximum spot diameter of the *EQE* measurement setup is of around 3 mm, a modulation of the layer thicknesses over the spot size needs to be considered when comparing simulated *EQE* data with experimental values. Thirdly, due to a residual roughness of the flat ZnO:Al substrate and a growth-induced roughness of the $\mu\text{c-Si:H}$ layer, the solar cell deposited on a flat substrate is not perfectly flat. The residual roughness in the 10 nm range reduces the modulation depth of the interference fringes in the *EQE*. One way to compensate for the deviation between the simulated and experimental *EQE* is to average the simulated *EQE* data of the flat solar cells of various layer thicknesses. For this reason, the simulated *EQE* data of three *EQE* spectra of flat $\mu\text{c-Si:H}$ solar cells with i-layer thicknesses of $1082 \text{ nm} \pm 25 \text{ nm}$ is averaged. In addition, a simple moving average of 10 nm spectral width was applied to consider the resolution of the *EQE* measurement setup. The resulting averaged simulated *EQE* is in excellent agreement with the measured *EQE* over the entire wavelength range (see Figure 8.7 (b)).

Simulated vs. Measured *EQE* of the Prototype Solar Cell with Plasmonic Reflection Grating Back Contact

In Figure 8.8, the simulated *EQE* data of $\mu\text{c-Si:H}$ solar cell in n-i-p configuration deposited on a plasmonic reflection grating back contact is compared with experimental data (schematic cross-section in Figure 8.6). Except for the change in the surface texture the same geometrical parameters and optical data were applied as used for the flat solar cell. In Figure 8.8 (a), the *EQE* data of a single simulation at a fixed intrinsic $\mu\text{c-Si:H}$ layer thickness of 1082 nm is shown. Similarly to the simulated *EQE* data of flat solar cells, a very good agreement between simulated and experimental *EQE* data is shown for wavelengths smaller than 550 nm. For longer wavelengths, the positions of the interferences are reproduced in the simulations. In contrast to the flat solar cell, the simulated *EQE* data of the solar cell applying a plasmonic reflection grating back contact reveals very sharp resonances. For these resonances, high enhancements of the electric field are observed in the intrinsic $\mu\text{c-Si:H}$ layer, which are attributed to the resonant coupling of incident light into waveguide modes of the periodic solar cell design. In the case of a plasmonic reflection grating back contact, the grating at the back contact allows the incident light to couple to the waveguide modes of the solar cell layer stack. A detailed analysis of these modes is the subject of the following Section 8.3. As the bandwidth of these modes is very narrow (from 2 nm to 6 nm), they cannot

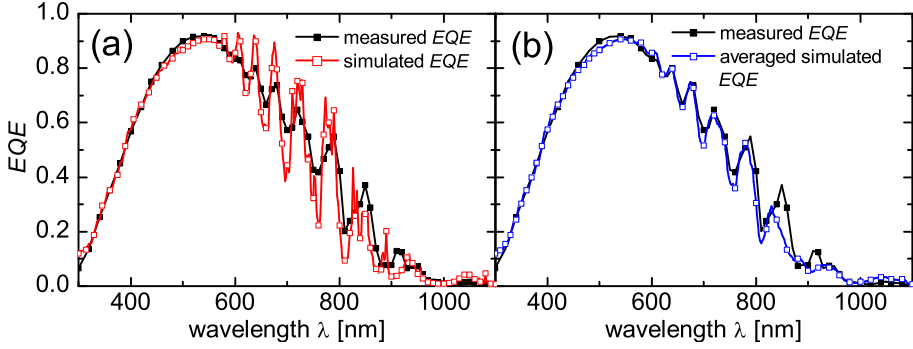


Figure 8.8: Simulated (red or blue line, open squares) and measured (black line) external quantum efficiency (EQE) of a μc -Si:H solar cell in n-i-p configuration deposited on a plasmonic reflection grating back contact of period of 500 nm. (a) The simulated EQE is shown for a single solar cell layer stack. (b) The simulated EQE is shown for a simple moving average with a final resolution of 10 nm of three solar cell layer stacks. The intrinsic μc -Si:H layer thickness of 1082 nm is varied by ± 25 nm.

be resolved in the measured EQE data. Thus, in order to compensate for the experimental imprecisions, similarly to the case of the flat solar cell, a simple moving average of averaged EQE spectra of three simulated solar cells is applied. This way, for the solar cell applying a plasmonic reflection grating back contact, a very good fit between simulations and experimental EQE is shown for the total wavelength range of interest (see Figure 8.8 (b)).

In summary, the comparison of simulated EQE data and measured EQE data of the prototype solar cells showed an excellent agreement when taking into account experimental variations such as the variation of the thickness of the layers in the solar cell. Thus, the light trapping effect caused by the plasmonic reflection grating is quantified very well in the simulations. As a consequence, the simulations of solar cells deposited on a plasmonic reflection grating back contact have a predictive power when optimizing geometrical parameters of these solar cells.

Simulated and Experimental J_{sc} of the Prototype Solar Cells with Plasmonic Reflection Grating Back Contacts In Figure 8.9, the simulated and experimental J_{sc} of μc -Si:H prototype solar cells deposited on plasmonic reflection grating back

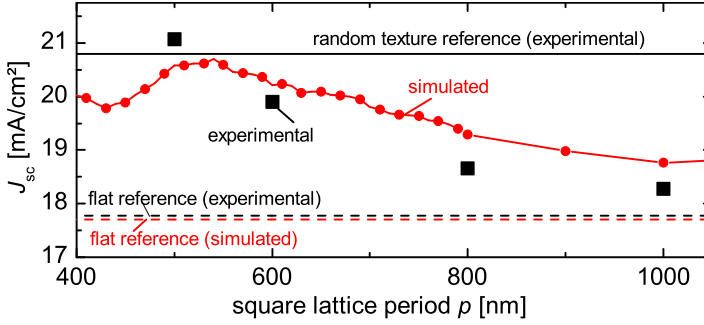


Figure 8.9: Comparison of the simulated and the measured short-circuit current density (J_{sc}) of μc -Si:H solar cells in n-i-p configuration deposited on plasmonic reflection grating back contacts of periods ranging from 500 nm to 1000 nm. The Ag nanostructures are of half-ellipsoidal shape (radius of around 110 nm and height of around 80 nm). They are arranged in square lattice.

contacts of square lattice periods between 500 nm and 1000 nm are compared. As a comparison, the J_{sc} of flat solar cells and randomly textured solar cells is shown. For all periods, qualitatively similar *EQE* enhancements are found in the wavelength range from 550 nm to 1000 nm (not shown). Both in the simulated and experimental results, the largest enhancement of J_{sc} for the given solar cell structures is found for a period of 500 nm. With increasing period, the measured J_{sc} decreases. A similar decrease in J_{sc} is calculated from the three-dimensional simulations. Overall, for all periods, the simulated absolute values of J_{sc} agree well with the measured values, allowing a future optimization of geometrical parameters such as the size and shape of the nanostructures.

Evaluation of the Parasitic Losses in the Prototype Solar Cells From the electromagnetic simulations of μc -Si:H solar cells in n-i-p configuration, three-dimensional absorption profiles were calculated allowing a layer specific evaluation of the absorption. It shall be noted that this information is not accessible with experimental techniques. In Figure 8.10, this layer specific absorption is shown for wavelengths from 500 nm to 1100 nm. In this wavelength range, both solar cells differ in their light trapping and consequently the *EQE* differs (c.f. Section 8.1). For both solar cells, most of the absorbed light is absorbed in the intrinsic μc -Si:H layer which contributes completely to the J_{sc} of the solar cell. For the n-doped and p-doped

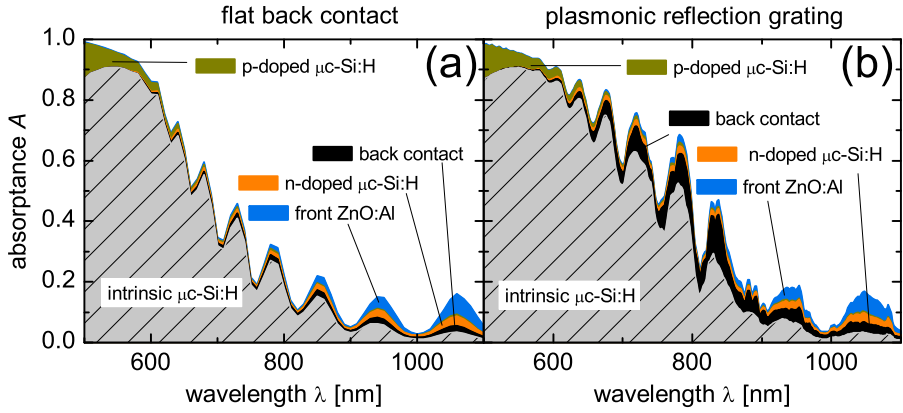


Figure 8.10: Simulated absorbance (A) differentiated for each layer of the flat solar cell (a) and the solar cell deposited on a plasmonic reflection grating back contact (b).

layers the charge carrier collection efficiencies are not known. They were treated as free parameters. A good agreement between simulated EQE and experimental EQE of the $\mu\text{c-Si:H}$ thin-film solar cells in the previous sections was obtained for collection efficiencies of 0%, 100% and 50% in the p-doped, intrinsic and n-doped $\mu\text{c-Si:H}$ layer, respectively. Based on these estimates, the parasitic losses in the solar cells can be identified. For wavelengths up to 550 nm, most of the parasitic absorption losses appear in the p-doped $\mu\text{c-Si:H}$ layer of the solar cells. For longer wavelengths, the absorption in the ZnO:Al front contact, the n-doped $\mu\text{c-Si:H}$ layer and the back contact, consisting of the Ag layer, and the back ZnO:Al layer gains relevance.

As reported in the previous section, the light trapping found for the solar cells deposited on the plasmonic reflection grating back contact enhances the absorption in the intrinsic $\mu\text{c-Si:H}$ layer. This enhancement results in an increase in J_{sc} of around 3.3 mA/cm^2 . The parasitic losses in the back contact and the n-doped $\mu\text{c-Si:H}$ layer increase strongly as shown in Figure 8.10 (b). For wavelengths longer than 750 nm, 33% of the light absorbed in the solar cell is absorbed by either the n-doped $\mu\text{c-Si:H}$ layer or the back contact. By comparing the EQE data of the solar cells presented in Figure 8.10 (a) and Figure 8.10 (b), an increase in the parasitic losses in Ag by a factor of 4.3 is identified. Thus, the enhanced light trapping found for the solar cells deposited on the plasmonic reflection grating comes at the cost of an enhanced ab-

sorption in the Ag layer. The LSPP resonances in the nanostructured Ag layer scatter incident light but also induce losses, leading to an enhanced absorption. In addition, due to the light trapping, light is guided in the solar cell layer stack and will interact more often with the plasmonic reflection grating back contact, leading to a further increase of the absorption in the Ag layer. Consequently, in order to improve the performance of the plasmonic reflection grating back contact, it is important to increase the diffraction-induced light trapping and to decrease the optical losses in the back contact. For further optimizations, the enhanced absorption in the Ag layer might become a limiting factor.

8.2.2 Optimization of the Light-Trapping Effect

A very good agreement between simulated EQE and measured EQE of the prototype solar cell applying a plasmonic reflection grating back contact was demonstrated in the previous Section 8.2.1. This agreement allows a realistic simulation based optimization of the geometrical parameters of the plasmonic reflection grating back contact. In order to identify the potential of the plasmonic reflection grating back contact for light trapping in μc -Si:H solar cells, three-dimensional electromagnetic simulations are applied in this section. The simulations are based on the same solar cell layer thicknesses and the same optical data as previously applied for the simulation of the solar cell prototypes.

Optimization of J_{sc} In Figure 8.11 (a), a schematic cross-section of the solar cell design under study is shown. In this optimization, both the radius and the period of plasmonic reflection grating back contacts are varied. For simplification, half-spherical Ag nanostructures are investigated. The solar cell layer stack configuration is assumed to be perfectly conformal. In Figure 8.11 (b), the simulated J_{sc} of the solar cells applying plasmonic reflection gratings of radii ranging from 50 nm to 500 nm and periods ranging from 150 nm to 1400 nm is shown. Only those plasmonic reflection grating back contacts are considered where the diameter of the nanostructure is smaller than the period of the grating. It is shown that independently of the period of the Ag nanostructure, for radii smaller than the thickness of the ZnO:Al layer (80 nm), the J_{sc} remains below 18.0 mA/cm². This value is close to the J_{sc} of the flat solar cell (17.7 mA/cm²). Therefore, there is no significant light-trapping effect in these solar cells.

As described in Section 5.2, the plasmonic resonances of half-spherical Ag nano-

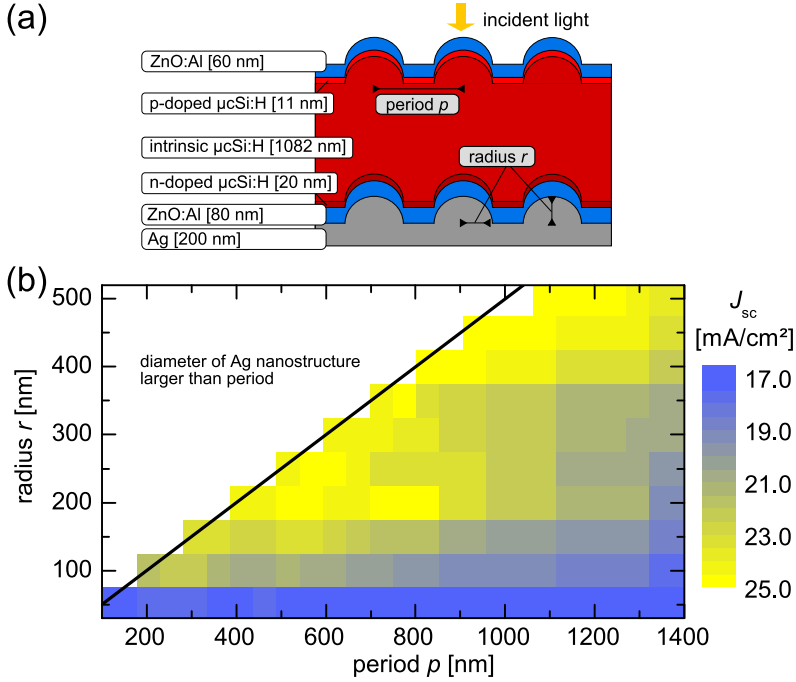


Figure 8.11: (a) Schematic cross-section of a $\mu\text{c-Si:H}$ solar cell in n-i-p configuration applying a plasmonic reflection grating back contact. (b) Map of the simulated short-circuit current density (J_{sc}) of $\mu\text{c-Si:H}$ solar cells in n-i-p configuration applying a plasmonic reflection grating back contact as a function of the period of the plasmonic reflection grating and the radius of the half-spherical Ag nanostructures.

structures of radii of 50 nm embedded in ZnO:Al are located at wavelengths smaller than 600 nm, where only a small fraction of the incident light reaches the back contact. The plasmon-induced absorption is much higher for small Ag nanostructures. With increasing radius of the nanostructures, the LSPR resonances shift to longer wavelengths and the relative plasmon-induced light scattering increases. This increased light scattering into large angles in the $\mu\text{c-Si:H}$ layer allows a better coupling of incident light into the solar cell (see Section 5.3). As a result, with an increasing radius of the Ag nanostructures, the plasmonic reflection grating back contact induces a larger light trapping in the solar cell and the J_{sc} increases (see Figure 8.11). For a fixed radius, highest J_{sc} values are found for the small periods. In these configura-

tions, the surface coverage of the nanostructures is large such that the fraction of the incident light which is diffracted into the diffraction orders at the plasmonic reflection grating back contact is enhanced (c.f. Section 5.2). With an increasing period, the surface coverage of the scattering Ag nanostructures decreases. As a result, the amount of incident light that is diffracted by the plasmonic reflection grating back contact decreases and the light trapping in the solar cells is reduced.

Maximum J_{sc} Enhancement For radii larger than 200 nm, highest values of J_{sc} above 24 mA/cm² and in some cases close to 25 mA/cm² are found. Considering the J_{sc} of 17.7 mA/cm² for a flat solar cell, the maximum identified potential in J_{sc} enhancement of the plasmonic reflection grating back contact for the given solar cell layer stack thicknesses is of around 7 mA/cm². This is significantly larger than the experimental J_{sc} enhancement of 3.3 mA/cm² for a non-optimized plasmonic reflection grating back contact (c.f. Section 8.1). Furthermore, the simulated potential presented here is a lower limit. Other geometries of the Ag nanostructures, unit cells of the plasmonic reflection grating or embedding material of the plasmonic reflection grating back contact might lead to a larger light trapping in μc -Si:H thin-film solar cells. For other solar cell configurations, such as tandem solar cells or p-i-n configurations, the potential will be different and needs to be evaluated in detail.

From an experimental point of view, it is expected that it is much more challenging to deposit a high quality μc -Si:H material on a very corrugated plasmonic reflection grating back contact substrate. The growth of the μc -Si:H material depends strongly on the texture of the substrate [202, 203]. Thus, plasmonic reflection grating back contacts which have lower modulation depth at highest J_{sc} are preferred. For the solar cells investigated in this section, plasmonic reflection gratings with nanostructure radii from 200 nm to 250 nm and periods from 600 nm to 800 nm are most promising (see Figure 8.11).

8.3 Leaky Waveguide Perspective on the Light-Trapping Effect

The light trapping effect of μc -Si:H thin-film solar cells applying plasmonic reflection grating back contacts was explained in Section 8.1.3 by an enhancement of the lengths of the light path in the μc -Si:H absorber material. This enhancement is caused by the diffraction of incident light at the back contact beyond the total internal reflection.

tion angle of the $\mu\text{c-Si:H}$ /air interface which is relevant for the total internal reflection at the front interface. The explanation is correct within the perspective of geometrical optics. However, it neglects the wave nature of propagating light within the solar cell as well as near-field effects. For this reason, the explanation is incomplete and several aspects like the appearance of very narrow resonances in the *EQE* cannot be explained in this perspective (see Section 8.2.1). This section provides a more fundamental analysis on the light trapping in thin-film silicon solar cells with plasmonic reflection grating back contacts. The light trapping is explained on the basis of leaky waveguide modes in the dielectric layer stack of the solar cell which couple to incident light.

Electric Field in the $\mu\text{c-Si:H}$ Solar Cells In Figure 8.12 (a), the simulated *EQEs* of $\mu\text{c-Si:H}$ solar cells applying a flat back contact and a plasmonic reflection grating back contact are compared for the wavelength range relevant for the light trapping (same *EQEs* as shown in Figure 8.7 (a) and Figure 8.8 (a)). In addition, the relative enhancement of the *EQE* is shown in Figure 8.12 (b). For wavelengths longer than 650 nm, several resonances of enhanced *EQE* are shown for the solar cell applying the plasmonic reflection grating back contact. These resonances have a full width half maximum value of only a few nanometers. For four distinct wavelengths of such resonances, the absolute electric field in a cross-section of the solar cell with the plasmonic reflection grating back contact is compared with the absolute electric field of the flat solar cell (see Figure 8.12 (c)). The electric field in the flat solar cell is dominated by the Fabry-Perot interferences of the dielectric layer stack of the solar cell and the highly reflecting Ag back contact. For the Fabry-Perot interferences, the local electric field strength is maximal 2 V/m, which is twice the incident electric field strength of 1 V/m. In contrast, for the solar cell with the plasmonic reflection grating back contact, the electric field exhibits a three-dimensional pattern. Some of these patterns exhibit regions of strongly enhanced electric field strength above 4 V/m. Considering that the absorption is proportional to the square of the electric field strength these patterns result in significantly enhanced *EQE*. The patterns are created by the superposition of electroamgentic waves which are diffracted at the plasmonic reflection grating back contact such that they are reflected multiple times within the solar cell (see Section 8.1.3). Due to local superpositions of electromagnetic waves of multiple reflections, the local electric field strength can be a multiple of the incident electric field strength. In addition, it shall be noted that the electric field in the vicinity of the Ag nanostructure in Figure 8.12 (c) is strongly enhanced. This enhancement is

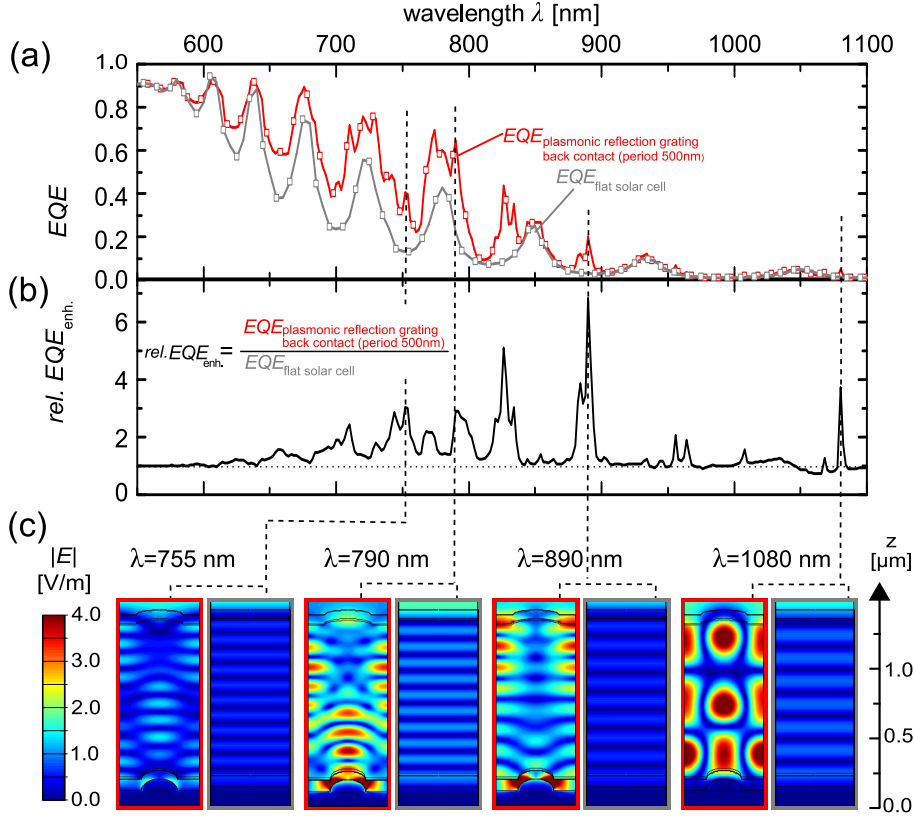


Figure 8.12: (a) Simulated external quantum efficiency (EQE) of μc -Si:H solar cells applying a flat back contact and a plasmonic reflection grating back contact of 500 nm period (shown in Figure 8.6). (b) Relative EQE enhancement ($rel. EQE_{enh.}$) of the solar cell applying the plasmonic reflection grating back contact in comparison with the flat cell. (c) Simulated absolute electric field in a cross-section of the flat solar cell (grey frame) and the solar cell with the plasmonic reflection grating back contact (red frame) at wavelengths of 755 nm, 790 nm, 890 nm and 1080 nm. The absolute electric field is given in the plane of polarization of the incident electromagnetic wave.

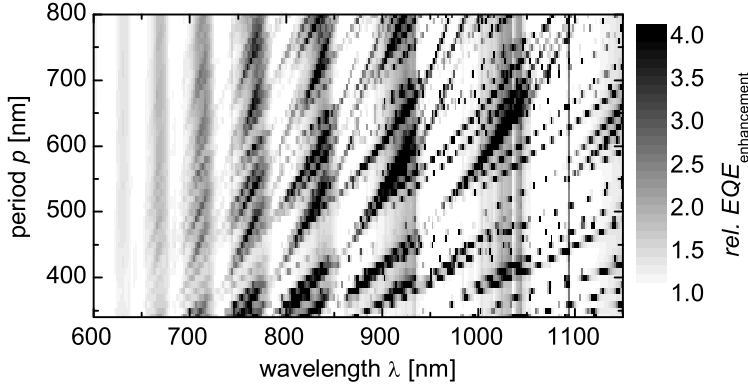


Figure 8.13: Relative enhancement of the external quantum efficiency ($rel. EQE_{\text{enhancement}}$) of the solar cell applying the plasmonic reflection grating back contact in comparison with the flat solar cell as a function of the wavelength and the period of the plasmonic reflection grating (schematic cross-section of solar cell in Figure 8.6).

attributed to the plasmonic resonance in the nanostructures. It is pronounced best for the wavelengths of 790 nm and 890 nm.

Leaky Waveguide Modes in Solar Cells with Plasmonic Reflection Grating Back Contact

Another terminology of the multiple internal reflection of the light within the layer stack of the solar cell is that the light diffracted at the plasmonic reflection grating back contact couples into guided modes (see Section 2.2.2). These modes are supported by the high refractive index μc -Si:H layers of the solar cell. In explicit, the dielectric layer stack of the solar cell represents a planar dielectric waveguide which is corrugated by the plasmonic reflection grating back contact and the front side texture. Thus, the patterns of enhanced electric field strength shown in Figure 8.12 for solar cells applying the plasmonic reflection grating back contact, belong to waveguide modes. As the incident light on the solar cell couples to the waveguide mode and vice versa, these modes are called leaky waveguide modes. Depending on the coupling efficiencies of incident light to these leaky waveguide modes, the enhancement of the electric field pattern belonging to a certain waveguide varies. As a result, the EQE exhibits resonances which correspond to resonance wavelengths of efficient coupling of incident light to a certain leaky waveguide mode.

For the μc -Si:H solar cell prototypes under study, the coupling of the leaky waveguide

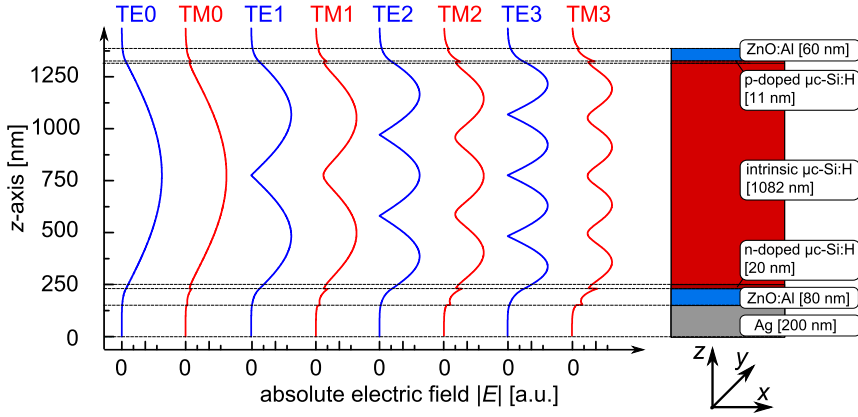


Figure 8.14: Absolute electric field of the first orders of the transverse electric (TE) and transverse magnetic (TM) modes in vertical direction of the flat $\mu\text{c-Si:H}$ solar cell layer stack for the wavelength of 650 nm.

modes to the incident light is caused by the plasmonic reflection grating back contact. Depending on the period of the plasmonic reflection grating, the diffraction angles at the back contact vary. This affects the resonance wavelength of the leaky waveguide modes. In order to illustrate this, the relative EQE enhancement of the solar cells with the plasmonic reflection grating back contacts is shown in Figure 8.13. The relative EQE enhancement is shown as a function of the period of the plasmonic reflection grating and the wavelength. The dispersive characteristic of the waveguide modes is observed. In fact, a large number of waveguide modes induce resonances of enhanced EQE . The differences in the value of the relative EQE enhancement for different leaky waveguide modes show the variation of the coupling efficiency of incident light into the waveguide modes.

Waveguide Modes in the Flat Solar Cell For perfectly flat planar waveguides, the transversal electric (TE) and transversal magnetic (TM) guided modes can be calculated numerically. A guided mode in the flat solar cell is an eigensolution of the time-harmonic Maxwell's equations. The numerical calculations of this eigenvalue problem were carried out with the Propagation Mode Solver of JCMSuite (for more details, see Appendix B). As a result, for a given wavelength, the wavevector ($k_x(\lambda)$) of an numerical eigensolution to the time-harmonic Maxwell's equations is given as well as the electric and magnetic field. In Figure 8.14, the electric field intensity of

the first orders of the TE and TM modes with the highest modal overlap with the $\mu\text{c-Si:H}$ layer are shown in vertical direction of the flat solar cell layer stack. Due to the lateral uniformity of the flat solar cell in y -direction as well as x -direction, the electric field is homogeneous in these directions.

Comparing the Waveguide Modes of the Flat Solar Cell to the Relative *EQE* Enhancement of the Solar Cells with Plasmonic Reflection Grating Back Contact

The waveguide modes calculated for a flat solar cell are compared hypothetically with the leaky waveguides of the solar cell applying a plasmonic reflection grating back contact. For the waveguide modes calculated for the perfectly flat solar cell layer stack (see Figure 8.14), a coupling to propagating electromagnetic waves outside of the solar cell is prohibited. For the coupling, a perturbation of the perfect planar geometry is essential. For the solar cells applying the plasmonic reflection grating back contact, the coupling is provided by the diffraction of incident light at the plasmonic grating coupler at the back contact. To compare the calculated waveguide modes of the perfectly flat solar cell layer stack to the leaky waveguide modes of the solar cell with plasmonic reflection grating back contact (see Figure 8.13), the periodicity of the electric fields in the latter geometry needs to be considered. This periodicity is determined by the grating constant (G_{mn}) of the plasmonic reflection grating back contact which is parallel to the direction of propagation of the considered waveguide mode:

$$|\mathbf{k}_{x,y}(\lambda)| = \frac{2\pi}{G_{mn} \cdot p}, \quad (8.1)$$

where $\mathbf{k}_{x,y}(\lambda)$ is the wavevector of the waveguide mode in the two dimensional x/y -plane. From Eq. (8.1) for a given G_{mn} and $\mathbf{k}_{x,y}(\lambda)$, the corresponding period (p) of a waveguide mode which couples to a two-dimensional grating is derived. This way, the dispersions of the waveguide modes of flat solar cells are calculated and compared with the dispersion of the leaky waveguide modes of the solar cell applying a plasmonic reflection grating back contact. In Figure 8.15 (a)-(d), for the grating constants $G_{10}, G_{11}, G_{20}, G_{21}$ and G_{22} , the calculated dispersions of the waveguide modes of the flat solar cell are superimposed on the simulated relative *EQE* enhancement map of the solar cells applying the plasmonic reflection grating back contact. It is shown that all leaky waveguide modes observed in the simulated *EQE* enhancement map can be correlated well to a waveguide mode of the flat solar cell. In particular, the bands of enhanced *EQE* in the 700 nm to 1100 nm range correlate well to the calculated waveguide modes in the flat device. Deviations between the calculated

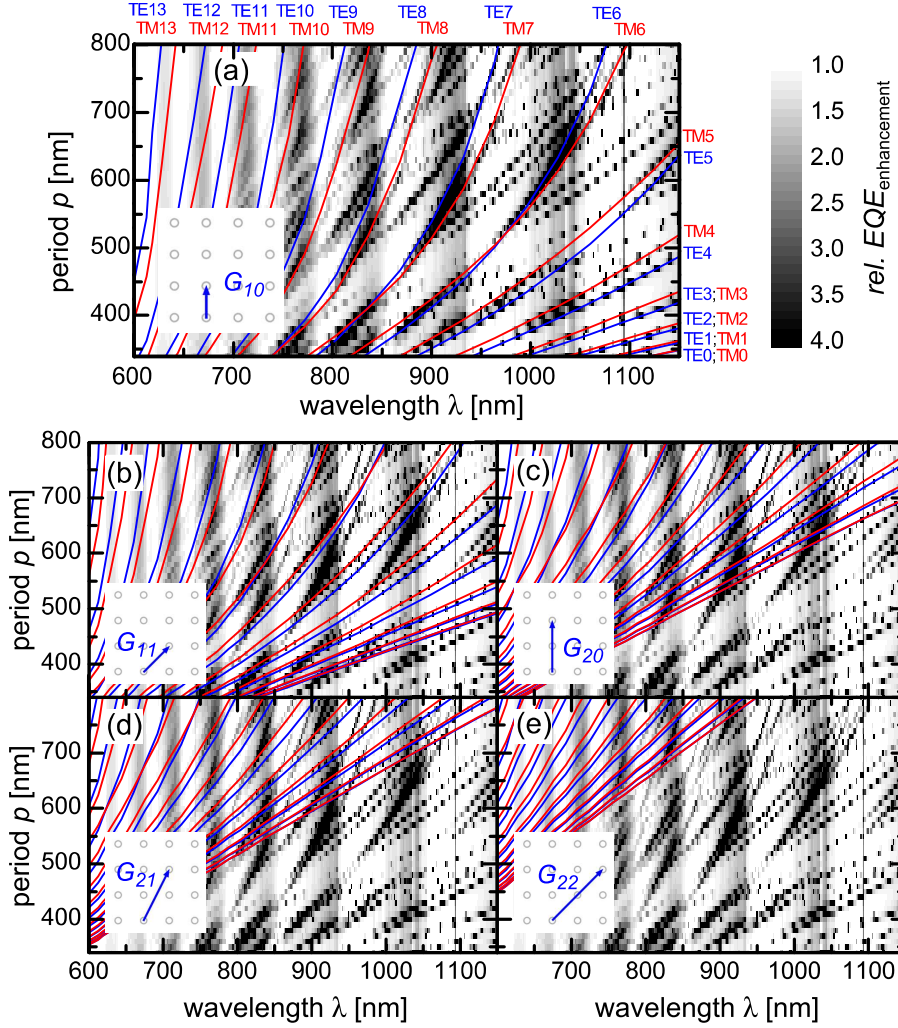


Figure 8.15: Relative enhancement of the external quantum efficiency ($rel. EQE_{enhancement}$) of the solar cell applying the plasmonic reflection grating back contact and calculated dispersion of the waveguide modes of a flat solar cell (red and blue lines) for the grating constants $G_{10}, G_{11}, G_{20}, G_{21}$ and G_{22} .

waveguide modes of flat solar cells and the leaky waveguide modes are attributed to geometric deviations of the flat solar cell and the corrugated solar cell with plasmonic reflection grating back contact. All modes which contribute significantly to the *EQE* enhancement of the solar cells applying the plasmonic reflection grating back contact can be associated with the waveguide modes of the flat solar cell. For a complete nomenclature, the variables m and n of the two-dimensional grating constant G_{mn} and the number and type (TE or TM) of the waveguide mode are sufficient.

In conclusion, the *EQE* enhancement reported for the solar cells applying the plasmonic reflection grating back contact is caused by a coupling of incident light into leaky waveguide modes of the solar cell layer stack. The solar cells which apply a plasmonic reflection grating back contact can be imagined as flat planar waveguides with perturbations, i.e., the plasmonic reflection grating back contact. These perturbations enable the coupling of the incident light into the waveguides. In future, it is of great interest to study the coupling of incident electromagnetic waves to waveguide modes.

8.4 Conclusion

In this chapter, the implementation and optical simulation of plasmonic reflection grating back contacts in $\mu\text{c-Si:H}$ thin-film solar cells in n-i-p configuration were presented. Prototypes of the solar cells applying the plasmonic reflection grating back contact were shown which exhibit a significantly enhanced *EQE* and J_{sc} when compared with flat solar cells. For a period of the plasmonic reflection grating of 500 nm, even an enhanced J_{sc} was observed in comparison with the state-of-the-art random texture for light trapping in thin-film silicon solar cells. Thus, experimentally the potential of light trapping via plasmonic reflection grating back contacts and, in more general terms, of nanostructures at the back contact in thin film silicon solar cell, has been demonstrated.

An excellent agreement was presented between the simulated and the measured *EQE* of the prototype solar cells. Based on this agreement, a simulation based optimization of the geometric parameters of the plasmonic reflection grating back contact was conducted. A large improvement potential of thin-film silicon solar cells applying plasmonic reflection grating back contacts was presented.

In addition, three-dimensional electromagnetic simulations were applied in this chapter to explain the working principle of the plasmonic reflection grating back

contacts. First, the light propagation in the solar cell was analyzed from the more intuitive perspective of geometrical optics. Second, the light trapping caused by the plasmonic reflection grating back contact in the solar cells was explained from the perspective of waveguide theory.

Chapter 9

Conclusion and Outlook

In this work, plasmon-induced optical losses at textured Ag back contacts and plasmonic light-trapping with nanostructured Ag back contacts in thin-film silicon solar cells were studied. Electromagnetic simulations of various plasmonic effects at nanotextured Ag back contacts along with solar cell prototypes were presented. The studies applied microcrystalline silicon solar cells which are commonly used as bottom solar cells of tandem thin-film silicon solar cell devices. In this type of solar cell, light trapping is particularly relevant for light in the infrared and near-infrared ($500 \text{ nm} < \lambda < 1100 \text{ nm}$). For light-scattering plasmonic nanostructures placed at the rear side of the solar cell, the operating spectral range of the plasmonic back contacts matches this wavelength range.

Conclusion First, the development of the ultra violet nanoimprint lithography was presented. It was used in this work as a technology platform for the replication of nanotextures for light trapping in solar cells. Two types of texture were replicated at very high precision: randomly textured ZnO:Al substrates and periodic nanotextures. It was found that the ultraviolet nanoimprint lithography opens new possibilities to replicate novel textures for light trapping such as plasmonic grating structures. The investigation of plasmonic back contacts started with a numerical study on the light-matter interaction of Ag nanostructures which exhibit localized plasmonic resonances. The applied three-dimensional electromagnetic simulation method proved to be a powerful tool for the simulation of plasmonic effects. It allowed an in-depth analysis of the absorption characteristic and scattering characteristic of nanostructures on the Ag back contact at the rear side of $\mu\text{c-Si:H}$ solar cells. It was shown

that the size, shape, embedding dielectric layers and arrangement of the nanostructures have to be chosen carefully in order to scatter incident light at high efficiency and low optical losses at the plasmonic back contact. For example, for small Ag nanostructures of dimension below 100 nm, localized plasmons were found to induce strong optical losses. Only for Ag nanostructures of radius larger than 200 nm, plasmonic nanostructures on Ag back contacts scatter incident light at high efficiencies into large angles in the $\mu\text{c-Si:H}$ absorber layer of the solar cell. The latter is required for light trapping in thin-film silicon solar cells. Both, periodic and isolated Ag nanostructures showed promising potential for light trapping in solar cells. A particular advantage for the periodic arrangement of plasmonic nanostructures on the Ag back contact, called plasmonic reflection grating back contacts, is the possibility to control the scattering angles of the plasmonic back contact via the diffraction orders.

In addition to plasmon-induced light scattering, plasmon-induced optical losses of small nanostructures on randomly textured Ag back contacts were studied. It was shown that even at a comparably low surface coverage of small hemispherical Ag nanostructures (dimensions below 200 nm) at the back contact, the LSPP resonances induce strong optical losses. Thus, it was concluded that in addition to propagating plasmon-induced absorption losses which have been discussed in the literature, also localized plasmon induced optical losses decrease the reflectivity of randomly textured Ag back contacts in state-of-the-art thin-film silicon solar cells. Due to the shift of the plasmonic resonances to shorter wavelengths with decreasing refractive index of the embedding material, their impact on the solar cell performance is reduced if interlayers of low refractive index are used at the rear side of the solar cell. The effect is demonstrated by comparing a $\mu\text{c-Si:H}$ thin-film solar cell with and without ZnO:Al interlayer at the back contact. For dielectric interlayers of even smaller refractive index than ZnO:Al an additional, but small, potential for increasing the reflection at the back contact was demonstrated in $\mu\text{c-Si:H}$ thin-film solar cells.

Next, the light-trapping effect of plasmonic back contacts with non-ordered Ag nanostructures in a $\mu\text{c-Si:H}$ thin-film solar cell prototype was studied. Ag back contacts with various distributions of non-ordered half-ellipsoidal Ag nanostructures were prepared. Their reflectance spectra in air are qualitatively well reproduced by reflectance spectra calculated from electromagnetic simulations of localized plasmon resonances in isolated nanostructures on Ag back contacts. This allowed the measured enhanced diffuse reflection at the back contacts to be attributed to plasmon-induced light scattering at the nanostructures at the back contacts. As a consequence, the light trapping demonstrated in a $\mu\text{c-Si:H}$ solar cell prototype in n-i-p configuration, which applies

one promising type of plasmonic Ag back contacts with non-ordered Ag nanostructures, was attributed to plasmon-induced light scattering. However, due to the overall low diffuse reflectance of the Ag back contacts with non-ordered nanostructures into the $\mu\text{c-Si:H}$ layer, the light trapping effect of the prototype solar cell is low.

Finally, $\mu\text{c-Si:H}$ thin-film solar cells with plasmonic reflection grating back contacts were studied. These solar cells exhibited a very good light trapping. For an optimized period of the plasmonic reflection grating back contact, even an enhanced light trapping in comparison with the state-of-the-art random texture was shown. Thus, experimentally the potential of light trapping via plasmonic reflection grating back contacts was demonstrated. Based on electromagnetic simulation, the light trapping caused by the plasmonic reflection grating back contact was explained in the intuitive perspective of geometrical optics as well as in terms of waveguide theory. An excellent agreement was achieved between the measured and simulated spectral response of the prototype solar cells. This allowed a simulation based optimization of the geometric parameters of the plasmonic reflection grating back contact.

It shall be highlighted that the demonstrated light-trapping effect of plasmonic reflection grating back contacts is the first experimental proof that plasmonic nanostructures can induce a light-trapping effect competitive with the state-of-the-art random texture for light trapping in microcrystalline thin-film silicon solar cells. Moreover, based on optical simulations, an additional significant improvement potential for thin-film silicon solar cells with plasmonic reflection grating back contacts was identified.

Outlook For all types of solar cells, light trapping is essential as it allows incident light to be guided in optically thin absorber layers. This way, the material consumption is reduced or the short-circuit current density is enhanced and the material requirements are decreased. Thus, the presented findings of plasmonic light trapping as well as approaches presented in this work to design the plasmonic back contacts are of great interest for many other solar cell technologies. The most proximate type of solar cell technology to the studied thin-film silicon solar cells are thin crystalline silicon solar cells. Currently, crystalline silicon solar cells process crystalline silicon wafers of thicknesses ranging from 250 μm to 100 μm [25]. In order to decrease the material costs, several groups currently work on reducing the thickness of the crystalline silicon absorber layer down to a few micrometers [218, 219]. With decreasing thickness, the absorptance of the wafers decreases and light trapping will become an important aspect for silicon wafer based photovoltaics which today have a share of around 88% of the annual solar cell production. As the spectral range for light-trapping in thin crystalline silicon solar cells is similar to the spectral range in

$\mu\text{c-Si:H}$ thin-film solar cells, the presented results on plasmonic light trapping are very useful to design and prototype plasmonic reflection grating back contacts at the rear side of crystalline silicon solar cells.

For the plasmonic reflection grating back contacts in $\mu\text{c-Si:H}$ thin-film solar cells, based on the electromagnetic simulations, a large improvement potential was identified in this work. In future studies, this improvement potential shall be addressed by optimizing the geometrical parameters of the plasmonic reflection grating back contacts. In addition, the electromagnetic simulations shall be employed to identify further optimization potential of the plasmonic reflection gratings. Hexagonal gratings and combinations of different gratings shall be investigated. Moreover, the plasmonic reflection grating back contacts shall also be applied to single junction $a\text{-Si:H}$ thin-film solar cells in p-i-n configuration as well as tandem thin-film silicon solar cells.

In general, the combination of three-dimensional electromagnetic simulations and prototyping of plasmonic devices proved to be an efficient approach to study plasmonic light-trapping concepts. Making use of these combined methods will allow an efficient and accelerated development of novel nano-optical light-trapping concepts and solar cell designs in future studies. In particular, regarding the prototyping of new nano-optical light trapping concepts, the UV-NIL provides a new technology platform. The applied three-dimensional electromagnetic solver proved to be an efficient method to design periodic nanophotonic textures for light trapping in thin-film solar cells.

In this work, solely plasmonic Ag nanostructures have been studied. Due to the scarcity of the noble metal Ag, and to address the related high material cost, alternative metals such as Cu and Al shall be explored in future with regard to plasmonic and nanophotonic effects in solar cells. Alternatively, due to presumably lower optical losses, dielectric grating structures at the rear side of a solar cell are of great interest in order to replace metal reflection gratings.

Finally, understanding the broadband light trapping with multiple narrow leaky waveguide resonances in periodic solar cell devices is a matter of on-going research. Several fundamental aspects, such as the role of the coupling efficiency between incident light and waveguide modes, shall be looked at in future work. In general, it is believed that a deeper understanding of light trapping in thin-film silicon solar cells requires a leaky waveguide perspective.

Appendix A

Optical Parametrization

The presented three-dimensional electromagnetic simulations of solar cell devices rely on realistic optical data. The optical data sets applied in this work are taken from measurements of state-of-the-art materials which are prepared at the IEK5-Photovoltaik (Forschungszentrum Jülich GmbH) for the preparation of thin-film silicon solar cells. The real part and the imaginary part of the complex refractive index $\tilde{n}(\lambda) = n(\lambda) + i\kappa(\lambda)$ is shown for each material applied in this work. Following the standard conventions, the real part of the complex refractive index $n(\lambda)$ is simply called the refractive index and the imaginary part of the complex refractive index $\kappa(\lambda)$ is called extinction coefficient.

Optical Data of Dielectrics The optical data of the dielectric materials applied in this work was determined by combining photothermal deflection spectroscopy, transmission and reflection measurements and ellipsometry measurements. Details of the measurements are presented in [74, 75]. The data of the intrinsic, p-doped and n-doped μc -Si:H and a -Si:H as well as front and back ZnO:Al are presented in Figure A.1, Figure A.2 and Figure A.3, respectively.

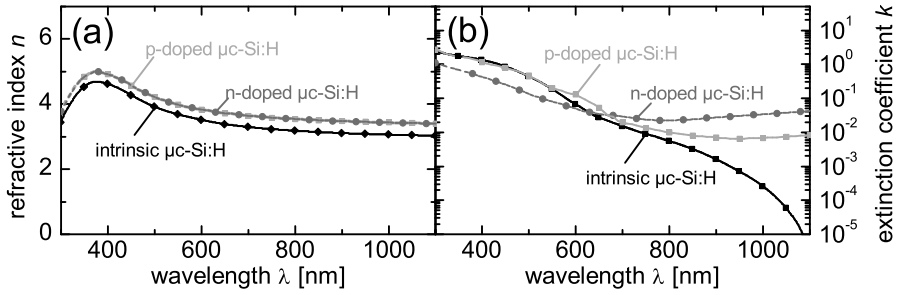


Figure A.1: Refractive index (n) and extinction coefficient (κ) of intrinsic, p-doped and n-doped $\mu\text{c-Si:H}$ prepared by PECVD for thin-film silicon solar cells.

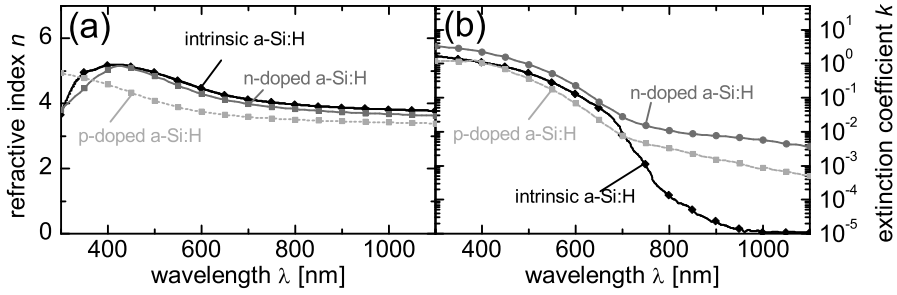


Figure A.2: Refractive index (n) and extinction coefficient (κ) of intrinsic, p-doped and n-doped a-Si:H prepared by PECVD for thin-film silicon solar cells.

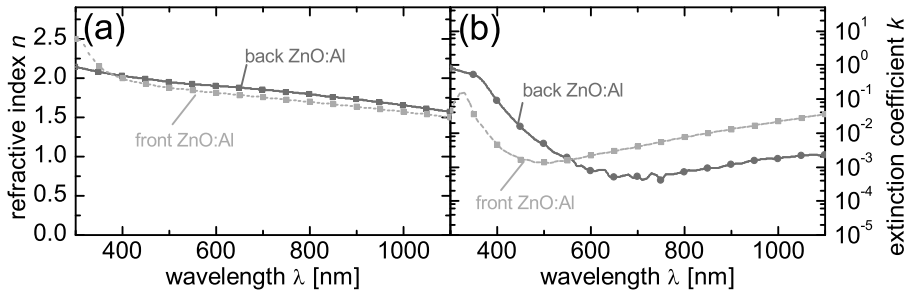


Figure A.3: Refractive index (n) and extinction coefficient (κ) of the ZnO:Al layers at the front and rear side of the thin-film silicon solar cells.

Optical Data of Ag The optical data of Ag layers strongly depends on the preparation conditions. In a recent study, it was shown that the optical data of thermally evaporated Ag films is influenced strongly by the substrate and growth of Ag crystallites in the Ag layer [73]. In fact, the quality of the Ag material is seldomly as good as reported in the standard reference for crystalline Ag [72]. In the presented work, the optical data of Ag is taken from ellipsometry measurements of a reference set of 500 nm thick thermally evaporated Ag layers deposited on glass substrate. In Figure A.4, the applied optical data of Ag is compared with the reference data from literature.

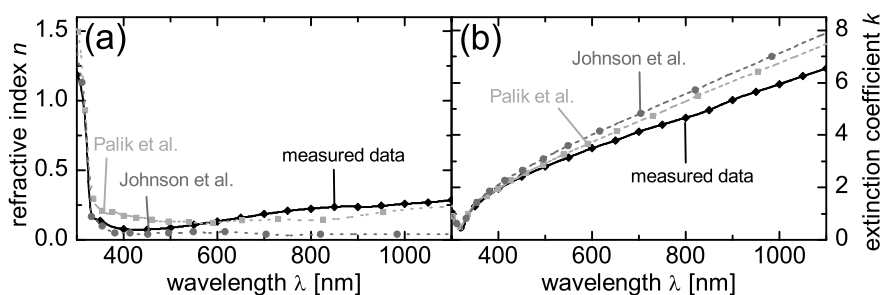


Figure A.4: The measured refractive index (n) and extinction coefficient (κ) of Ag compared with reference data from literature [72, 220].

Appendix B

Waveguide Modes in Planar Layer Stacks

For planar waveguides, in the stationary case, the waveguide modes are eigen solutions of an eigenvalue problem described in the section. In this work, the solutions of this eigenvalue problem which provide the transversal electric (TE) and transversal magnetic (TM) waveguide modes are calculated numerically with the Propagation Mode Solver of JCMSuite [122]. Here we follow the description of the eigenvalue problem given in [123].

In general, a waveguide mode in a flat layer stack is given as an eigensolution of the time-harmonic formulation of Maxwell's equations. This formulation exhibits a time-harmonic dependency in plane with the layer stack (in this case the z -direction):

$$\mathbf{E}_{\text{th}}(\mathbf{x}) = \mathbf{E}_{\text{th,GM}}(x, y) \cdot e^{(ik_z z)} \quad (\text{B.1})$$

$$\mathbf{H}_{\text{th}}(\mathbf{x}) = \mathbf{H}_{\text{th,GM}}(x, y) \cdot e^{(ik_z z)}, \quad (\text{B.2})$$

where k_z is the propagation constant in plane with the layer stack. It is sufficient to discuss the magnetic case as all considerations are valid for the electrical case if one interchanges \mathbf{H}_{th} and \mathbf{E}_{th} and ϵ and μ .

The magnetic field can be written as:

$$\mathbf{H}_{\text{th,GM}}(\mathbf{x}) = \begin{bmatrix} \mathbf{H}_{\perp}(x, y) \\ H_z(x, y) \end{bmatrix} \cdot e^{(ik_z z)}, \quad (\text{B.3})$$

$$(\text{B.4})$$

which gives

$$\nabla \times \mathbf{H}_{\text{th}}(\mathbf{x}) = \begin{bmatrix} ik_z P & -P\nabla \\ -\nabla_{\perp} & 0 \end{bmatrix} \begin{bmatrix} \mathbf{H}_{\perp}(x, y) \\ H_z(x, y) \end{bmatrix} \cdot e^{(ik_z z)}, \quad (\text{B.5})$$

with

$$P = \begin{bmatrix} 0 & -1 \\ 1 & 0 \end{bmatrix} \quad \text{and} \quad \nabla_{\perp} = \begin{pmatrix} \partial_x \\ \partial_y \end{pmatrix}. \quad (\text{B.6})$$

Applying this formulation of magnetic field to the time harmonic Maxwell's equations shown for the electric field in Eq. (2.20) and Eq. (2.19) gives:

$$\begin{bmatrix} P\nabla_{\perp}\epsilon_z^{-1}\nabla_{\perp} \cdot P - k_z^2 P\epsilon_{\perp}^{-1}P & -ik_z P\epsilon_{\perp}^{-1}P\nabla_{\perp} \\ -ik_z \nabla_{\perp} \cdot P\epsilon_{\perp}^{-1}P & \nabla_{\perp} \cdot P\epsilon_{\perp}^{-1}P\nabla_{\perp} \end{bmatrix} \begin{bmatrix} \mathbf{H}_{\perp}(x, y) \\ H_z(x, y) \end{bmatrix} = \omega^2 \begin{bmatrix} \mu_{\perp} & 0 \\ 0 & \mu_z \end{bmatrix} \begin{bmatrix} \mathbf{H}_{\perp}(x, y) \\ H_z(x, y) \end{bmatrix}, \quad (\text{B.7})$$

with

$$\epsilon = \begin{bmatrix} \epsilon_{\perp} & 0 \\ 0 & \epsilon_z \end{bmatrix} \quad \text{and} \quad \mu = \begin{bmatrix} \mu_{\perp} & 0 \\ 0 & \mu_z \end{bmatrix}. \quad (\text{B.8})$$

Then, Eq. (B.7) is a quadratic eigenvalue problem of k_z which is solved in this work by the Propagation Mode Solver of JCMsuite [122, 123].

References

- [1] “World Population Data Sheet 2010,” Population Reference Bureau (2010).
(URL: http://www.prb.org/pdf10/10wpds_eng.pdf, 01.04.2012).
- [2] “Renewable Energy Sources and Climate Change Mitigation - Special Report of the IPCC,” Intergovernmental Panel on Climate Change, Cambridge University Press, New York (2012).
- [3] “World Energy Outlook 2011,” International Energy Agency (2011).
(URL: <http://www.oecd-ilibrary.org/energy> , 24.3.2012).
- [4] M. Z. Jacobson and M. A. Delucchi, “Providing all global energy with wind, water, and solar power, Part I: Technologies, energy resources, quantities and areas of infrastructure, and materials,” *Energy Policy* **39**, 1154–1169 (2011).
- [5] M. Z. Jacobson, “Review of solutions to global warming, air pollution, and energy security,” *Energy & Environmental Science* **2**, 148 (2009).
- [6] M. Loster, “Total Primary Energy Supply From Sunlight,” (2010).
(URL: http://www.ez2c.de/ml/solar_land_area/, 01.04.2012).
- [7] D. M. Chapin, C. S. Fuller, and G. L. Pearson, “A New Silicon p-n Junction Photocell for Converting Solar Radiation into Electrical Power,” *Journal of Applied Physics* **25**, 676 (1954).
- [8] B. A. Sandén, “Solar solution: the next industrial revolution,” *Materials Today* **11**, 22–24 (2008).
- [9] “Global Market Outlook - for Photovoltaics until 2016,” European Photovoltaic Industry Association (2012). (URL: “<http://files.epia.org>”, 14.04.2012).

- [10] G. Hering, "Das Jahr des Drachen - Die Production von Solarzellen ist 2011 auf 37 Gigawatt gestiegen und die Dominanz Chinas wächst," *Photon - das Solarstrom Magazin* **4**, 42–63 (2012).
- [11] F. Dross, K. Baert, T. Bearda, J. Deckers, V. Depauw, O. El Daif, I. Gordon, A. Gougam, J. Govaerts, S. Granata, R. Labie, X. Loozen, R. Martini, A. Masolin, B. O'Sullivan, Y. Qiu, J. Vaes, D. Van Gestel, J. Van Hoeymisen, A. Vanleenhove, K. Van Nieuwenhuysen, S. Venkatachalam, M. Meuris, and J. Poortmans, "Crystalline thin-foil silicon solar cells: where crystalline quality meets thin-film processing," *Progress in Photovoltaics: Research and Applications* (2012). (article published online 01.02.2012).
- [12] H. Sakata, Y. Tsunomura, H. Inoue, S. Taira, T. Baba, H. Kanno, T. Kinoshita, M. Taguchi, and E. Maruyama, "R&D Progress of Next-Generation Very Thin HIT_{tm} Solar Cells," in *Proceedings of the 25th EUPVSEC* (Valencia, 2010), 1102–1105.
- [13] M. A. Green, "Thin-film solar cells: review of materials, technologies and commercial status," *Journal of Materials Science: Materials in Electronics* **18**, 15–19 (2007).
- [14] A. Wang, J. Zhao, S. R. Wenham, and M. A. Green, "21.5% Efficient thin silicon solar cell," *Progress in Photovoltaics: Research and Applications* **4**, 55–58 (1996).
- [15] K. L. Chopra, P. D. Paulson, and V. Dutta, "Thin-film solar cells: an overview," *Progress in Photovoltaics: Research and Applications* **12**, 69–92 (2004).
- [16] B. A. Andersson, "Materials availability for large-scale thin-film photovoltaics," *Progress in Photovoltaics: Research and Applications* **8**, 61–76 (2000).
- [17] B. A. Andersson, C. Azar, J. Holmberg, and S. Karlsson, "Material constraints for thin-film solar cells," *Energy* **23**, 407–411 (1998).
- [18] A. W. Blakers, J. H. Werner, E. Bauser, and H. J. Queisser, "Silicon epitaxial solar cell with 663-mV open-circuit voltage," *Applied Physics Letters* **60**, 2752 (1992).
- [19] R. Brendel and H. Queisser, "On the thickness dependence of open circuit voltages of p-n junction solar cells," *Solar Energy Materials and Solar Cells* **29**, 397–401 (1993).

-
- [20] K. R. Catchpole and A. Polman, “Plasmonic solar cells,” *Optics Express* **16**, 21793–21800 (2008).
- [21] F. J. Beck, A. Polman, and K. R. Catchpole, “Tunable light trapping for solar cells using localized surface plasmons,” *Journal of Applied Physics* **105**, 114310 (2009).
- [22] H. A. Atwater and A. Polman, “Plasmonics for improved photovoltaic devices,” *Nature Materials* **9**, 205–213 (2010).
- [23] V. E. Ferry, J. N. Munday, and H. A. Atwater, “Design considerations for plasmonic photovoltaics,” *Advanced Materials* **22**, 4794–4808 (2010).
- [24] F. Hallermann, C. Rockstuhl, S. Fahr, G. Seifert, S. Wackerow, H. Graener, G. V. Plessen, and F. Lederer, “On the use of localized plasmon polaritons in solar cells,” *physica status solidi (a)* **205**, 2844–2861 (2008).
- [25] M. A. Green and S. Pillai, “Harnessing plasmonics for solar cells,” *Nature Photonics* **6**, 130–132 (2012).
- [26] P. Würfel, *Physik der Solarzellen* (Spektrum Akademischer Verlag GmbH, Heidelberg Berlin Oxford, 1995).
- [27] M. A. Green, *Solar Cells: Operating Principles, Technology, and System Applications* (Prentice Hall, Englewood Cliffs - New Jersey, 1982).
- [28] D. E. Carlson and C. R. Wronski, “Amorphous silicon solar cell,” *Applied Physics Letters* **28**, 671–673 (1976).
- [29] R. A. Street, *Hydrogenated Amorphous Silicon* (Cambridge University Press, Cambridge, 1991).
- [30] B. Rech and H. Wagner, “Potential of amorphous silicon for solar cells,” *Applied Physics A: Materials Science & Processing* **69**, 155–167 (1999).
- [31] J. Meier, F. L. Flückiger, H. Keppner, and A. Shah, “Complete microcrystalline p-i-n solar cell – Crystalline or amorphous cell behavior ?” *Applied Physics Letters* **65**, 860–862 (1994).

- [32] K. Yamamoto, M. Yoshimi, T. Suzuki, Y. Tawada, Y. Okamoto, and A. Nakajima, "Thin film poly-Si solar cell on glass substrate fabricated at low temperature," *Applied Physics A: Materials Science & Processing* **69**, 131179–131185 (1998).
- [33] O. Vetterl, F. Finger, R. Carius, P. Hapke, L. Houben, O. Kluth, A. Lambertz, A. Mück, B. Rech, and H. Wagner, "Intrinsic microcrystalline silicon: A new material for photovoltaics," *Solar Energy Materials and Solar Cells* **62**, 97–108 (2000).
- [34] N. W. Ashcroft and D. N. Mermin, *Solid State Physics* (Thomas Learning Inc., Singapore South Melbourne Toronto London Mexico Madrid, 1976).
- [35] W. Shockley and H. J. Queisser, "Detailed Balance Limit of Efficiency of p-n Junction Solar Cells," *Journal of Applied Physics* **32**, 510 (1961).
- [36] J. Meier, R. Flückiger, H. Keppner, M. Goetz, and A. Shah, "Microcrystalline silicon p-i-n solar cells prepared by very high frequency-glow discharge," in *12th EC Photovoltaic Solar Energy Conference* (Amsterdam, 1994), 1237–1240.
- [37] K. Yamamoto, "Thin-film crystalline silicon solar cells," *Japan Society of Applied Physics International* **7**, 12–19 (2003).
- [38] B. Rech, T. Repmann, M. van den Donker, M. Berginski, T. Kilper, J. Hüpkes, S. Calnan, H. Stiebig, and S. Wieder, "Challenges in microcrystalline silicon based solar cell technology," *Thin Solid Films* **511-512**, 548–555 (2006).
- [39] R. E. I. Schropp, "Large-Area Thin-Film Silicon: Synergy between Displays and Solar Cells," *Japanese Journal of Applied Physics* **51**, 03CA07 (2012).
- [40] U. Kroll, J. Meier, L. Fesquet, J. Steinhäuser, S. Benagli, B. Wolf, D. Borrello, L. Castens, Y. Djeridane, X. Multone, G. Choong, D. Dominé, M. Marmelo, G. Monteduro, B. Dehbozorgi, D. Romang, E. Omnes, M. Chevalley, G. Charitat, A. Pomey, S. Marjanovic, G. Kohnke, K. Koch, J. Liu, R. Modavis, D. Thelen, S. Vallon, A. Zakharian, and D. Weidman, "Recent developments of high-efficiency micromorph tandem solar cells in kai-m/ plasmabox pecvd reactors," in *Proceedings of the 26th EUPVSEC* (Hamburg, 2011), 2340 – 2343.

-
- [41] M. A. Green, K. Emery, Y. Hishikawa, W. Warta, and E. D. Dunlop, "Solar cell efficiency tables (version 39)," *Progress in Photovoltaics: Research and Applications* **20**, 12–20 (2012).
- [42] K. Yamamoto, A. Nakajima, M. Yoshimi, T. Sawada, S. Fukuda, and T. Suezaki, "High efficiency thin film silicon hybrid cell and module with newly developed innovative interlayer," in *Proceedings of the IEEE 4th World Conference on Photovoltaic Energy Conversion* (Waikoloa, 2006), 1489–1492.
- [43] P. Buehlmann, J. Bailat, D. Dominé, A. Billet, F. Meillaud, A. Feltrin, and C. Ballif, "In situ silicon oxide based intermediate reflector for thin-film silicon micromorph solar cells," *Applied Physics Letters* **91**, 143505 (2007).
- [44] A. Lambertz, T. Grundler, and F. Finger, "Hydrogenated amorphous silicon oxide containing a microcrystalline silicon phase and usage as an intermediate reflector in thin-film silicon solar cells," *Journal of Applied Physics* **109**, 113109 (2011).
- [45] W. Böttler, V. Smirnov, A. Lambertz, J. Hüpkas, and F. Finger, "Window layer development for microcrystalline silicon solar cells in n-i-p configuration," *physica status solidi (c)* **7**, 1069–1072 (2010).
- [46] O. Kluth, B. Rech, L. Houben, S. Wieder, G. Schöpe, C. Beneking, H. Wagner, A. Löffl, and H. Schock, "Texture etched ZnO:Al coated glass substrates for silicon based thin film solar cells," *Thin Solid Films* **351**, 247–253 (1999).
- [47] J. Müller, O. Kluth, S. Wieder, H. Siekmann, G. Schöpe, W. Reetz, O. Vetterl, D. Lundszen, A. Lambertz, F. Finger, B. Rech, and H. Wagner, "Development of highly efficient thin film silicon solar cells on texture-etched zinc oxide-coated glass substrates," *Solar Energy Materials and Solar Cells* **66**, 275–281 (2001).
- [48] J. Hüpkas, J. I. Owen, S. E. Pust, and E. Bunte, "Chemical etching of zinc oxide for thin-film silicon solar cells," *Chemphyschem : a European Journal of Chemical Physics and Physical Chemistry* **13**, 66–73 (2012).
- [49] N. Taneda, K. Masumo, M. Kambe, T. Oyama, and K. Sato, "Highly Textured SnO₂ Films for a-Si/ μ c-Si Tandem Solar Cells," in *Proceedings of the 23th EUPVSEC* (Valencia, 2008), 2084–2087.

- [50] M. Kambe, A. Takahashi, N. Taneda, K. Masumo, T. Oyama, and K. Sato, "Fabrication of a-Si:H Solar cells on high haze SnO₂:F thin films," in *33rd IEEE - Photovoltaic Specialists Conference* (San Diego, 2008), 1–4.
- [51] S. Faÿ, J. Steinhauser, S. Nicolay, and C. Ballif, "Polycrystalline ZnO: B grown by LPCVD as TCO for thin film silicon solar cells," *Thin Solid Films* **518**, 2961–2966 (2010).
- [52] J. Hüpkes, J. Müller, and B. Rech, "Transparent Conductive Zinc Oxide: Basics and Applications in Thin Film Solar Cells," in *Transparent Conductive Zinc Oxide: Basics and Applications in Thin Film Solar Cells*, K. Ellmer, A. Klein, and B. Rech, eds. (Springer, Berlin, 2008), p. 362.
- [53] J. Hüpkes, B. Rech, O. Kluth, T. Repmann, B. Zwaygardt, J. Müller, R. Drese, and M. Wuttig, "Surface textured MF-sputtered ZnO films for microcrystalline silicon-based thin-film solar cells," *Solar Energy Materials and Solar Cells* **90**, 3054–3060 (2006).
- [54] M. Berginski, J. Hüpkes, M. Schulte, G. Schöpe, H. Stiebig, B. Rech, and M. Wuttig, "The effect of front ZnO:Al surface texture and optical transparency on efficient light trapping in silicon thin-film solar cells," *Journal of Applied Physics* **101**, 074903 (2007).
- [55] M. Berginski, "Schichten und Schichtsysteme zur Verbesserung der Lichteinkopplung in Silizium-Dünnschichtsolarzellen," Doctoral thesis, RWTH Aachen University (2007).
- [56] J. Hüpkes, "Untersuchung des reaktiven Sputterprozesses zur Herstellung von aluminiumdotierten Zinkoxid- Schichten für Silizium-Dünnschichtsolarzellen," Doctoral thesis, RWTH Aachen University (2005).
- [57] H. Overhof and P. Thomas, *Electronic transport in hydrogenated amorphous semiconductors* (Springer-Verlag, Berlin, 1989).
- [58] D. L. Staebler and C. R. Wronski, "Reversible conductivity changes in discharge-produced amorphous Si," *Applied Physics Letters* **31**, 292 (1977).
- [59] S. Klein, T. Repmann, and T. Brammer, "Microcrystalline silicon films and solar cells deposited by PECVD and HWCVD," *Solar Energy* **77**, 893–908 (2004).

-
- [60] A. V. Shah, J. Meier, E. Vallat-Sauvain, N. Wyrsh, U. Kroll, C. Droz, and U. Graf, "Material and solar cell research in microcrystalline silicon," *Solar Energy Materials and Solar Cells* **78**, 469–491 (2003).
- [61] L. Houben, M. Luysberg, P. Hapke, R. Carius, F. Finger, and H. Wagner, "Structural properties of microcrystalline silicon in the transition from highly crystalline to amorphous growth," *Philosophical Magazine A* **77**, 1447–1460 (1998).
- [62] R. Carius, T. Merdzhanova, F. Finger, S. Klein, and O. Vetterl, "A comparison of microcrystalline silicon prepared by plasma-enhanced chemical vapor deposition and hot-wire chemical vapor deposition : electronic and device properties," *Journal of Materials Science: Materials in Electronics* **14**, 625–628 (2003).
- [63] "Reference Solar Spectral Irradiance: Air Mass 1.5," American Society for Testing and Materials - Terrestrial Reference Spectra for Photovoltaic Performance Evaluation (2007). (URL: <http://rredc.nrel.gov/solar/spectra/am1.5/>, 5.04.2010).
- [64] C. Gueymard, D. Myers, and K. Emery, "Proposed reference irradiance spectra for solar energy systems testing," *Solar Energy* **73**, 443–467 (2002).
- [65] T. Merdzhanova, "Personal Communication - IV characteristic of state-of-the-art tandem thin-film silicon solar cell (IEK-5 Photovoltaik)," (2012).
- [66] "Technical Specifications for the LAMBDA 950 UV/Vis/NIR Spectrophotometers," PerkinElmer Inc. (2007). (URL: http://www.perkinelmer.com/CMSResources/Images/44-74789SPC_LAMBDA1050LAMBDA950.pdf, 12.04.2012).
- [67] S. J. Pennycook and P. D. Nellist, *Scanning Transmission Electron Microscopy* (Springer, New York, 2011).
- [68] K. Shimizu and T. Mitani, *New Horizons of Applied Scanning Electron Microscopy* (Springer, Berlin Heidelberg, 2010).
- [69] W. R. Bowen and N. Hilal, *Atomic Force Microscopy in Process Engineering An Introduction to AFM for Improved Processes and Products* (Elsevier/Butterworth-Heinemann, Oxford, 2009).

- [70] G. Kaupp, *Atomic Force Microscopy, Scanning Nearfield Optical Microscopy and Nanoscratching* (Springer, Berlin, 2006).
- [71] “SPIP version 5.1.6,” Image Metrology A/S, Horsholm, Denmark (2011).
- [72] P. B. Johnson and R. W. Christy, “Optical Constants of the Noble Metals,” *Physical Review B* **6**, 4370–4379 (1972).
- [73] J. Hyuk Park, P. Nagpal, S.-H. Oh, and D. J. Norris, “Improved dielectric functions in metallic films obtained via template stripping,” *Applied Physics Letters* **100**, 081105 (2012).
- [74] M. Ermes, “Study of optical properties of individual layers and layer stacks as used in silicon based thin-film solar cells,” Master thesis, RWTH Aachen University (2010).
- [75] K. Ding, “Charakterisierung und Simulation von a-Si:H/ μ c-Si:H Tandem Solarzellen,” Master thesis, RWTH Aachen University (2009).
- [76] J. D. Jackson, *Classical Electrodynamics* (JohnWiley & Sons, New Jersey, 1999).
- [77] T. Fliessbach, *Elektrodynamik* (Spektrum Akademischer Verlag, Heidelberg, 2008).
- [78] E. Hecht, *Optics* (Addison Wesley Publishing Company, Reading, 1997).
- [79] B. E. A. Saleh and M. C. Teich, *Fundamentals of photonics* (Wiley, Hoboken - New Jersey, 2007).
- [80] J. Tominaga and T. Nakano, *Optical Near-Field Recording: Science and Technology* (Springer-Verlag, Berlin Heidelberg, 2005).
- [81] B. C. Capps and D. A. Systems, “Near field or far field ?” *Designfeature* (2001).
- [82] K. Bittkau and T. Beckers, “Near-field study of light scattering at rough interfaces of a-Si:H/ μ c-Si:H tandem solar cells,” *physica status solidi (a)* **207**, 661–666 (2010).

-
- [83] K. Bittkau, T. Beckers, S. Fahr, C. Rockstuhl, F. Lederer, and R. Carius, "Nanoscale investigation of light-trapping in a-Si:H solar cell structures with randomly textured interfaces," *physica status solidi (a)* **205**, 2766–2776 (2008).
- [84] U. Kreibig and M. Vollmer, *Optical Properties of Metal Clusters* (Springer-Verlag, Berlin, 1995).
- [85] H. Raether, *Surface Plasmons on Smooth and Rough Surfaces and on Gratings* (Springer, Berlin, 1988).
- [86] S. A. Maier, *Plasmonics: Fundamentals and Applications* (Springer, Berlin, 2007).
- [87] K. R. Catchpole and A. Polman, "Design principles for particle plasmon enhanced solar cells," *Applied Physics Letters* **93**, 191113 (2008).
- [88] A. V. Zayats and I. I. Smolyaninov, "Near-field photonics : surface plasmon polaritons and localized surface plasmons," *Journal of Optics A: Pure and Applied Optics* **5**, 16–50 (2003).
- [89] P. Nagpal, N. C. Lindquist, S.-H. Oh, and D. J. Norris, "Ultrasmooth patterned metals for plasmonics and metamaterials," *Science* **325**, 594–597 (2009).
- [90] S. A. Maier and H. A. Atwater, "Plasmonics: Localization and guiding of electromagnetic energy in metal/dielectric structures," *Journal of Applied Physics* **98**, 011101 (2005).
- [91] C. Dahmen and G. von Plessen, "Optical Effects of Metallic Nanoparticles," *Australian Journal of Chemistry* **60**, 447 (2007).
- [92] G. Mie, "Beiträge zur Optik trüber Medien, speziell kolloidaler Metallösungen," *Annalen der Physik* **330**, 377–445 (1908).
- [93] T. Klar, M. Perner, S. Grosse, G. von Plessen, W. Spirkel, and J. Feldmann, "Surface-Plasmon Resonances in Single Metallic Nanoparticles," *Physical Review Letters* **80**, 4249–4252 (1998).
- [94] C. Sönnichsen, T. Franzl, T. Wilk, and J. Feldmann, "Plasmon resonances in large noble-metal," *New Journal of Physics* **4**, 1–8 (2002).

- [95] C. F. Bohren and D. R. Huffman, *Absorption and Scattering of Light by Small Particles* (Wiley-VCH, New York, 1998).
- [96] J. J. Mock, M. Barbic, D. R. Smith, D. A. Schultz, and S. Schultz, "Shape effects in plasmon resonance of individual colloidal silver nanoparticles," *The Journal of Chemical Physics* **116**, 6755 (2002).
- [97] J. Aizpurua, P. Hanarp, D. Sutherland, M. Käll, G. Bryant, and F. García de Abajo, "Optical Properties of Gold Nanorings," *Physical Review Letters* **90**, 5–8 (2003).
- [98] C. Oubre and P. Nordlander, "Finite-difference time-domain studies of the optical properties of nanoshell dimers," *The Journal of Physical Chemistry B* **109**, 10042–10051 (2005).
- [99] P. Nordlander and F. Le, "Plasmonic structure and electromagnetic field enhancements in the metallic nanoparticle-film system," *Applied Physics B* **84**, 35–41 (2006).
- [100] P. Nordlander, C. Oubre, E. Prodan, K. Li, and M. I. Stockman, "Plasmon Hybridization in Nanoparticle Dimers," *Nano Letters* **4**, 899–903 (2004).
- [101] H. Wang, D. W. Brandl, F. Le, P. Nordlander, and N. J. Halas, "Nanorice: a hybrid plasmonic nanostructure," *Nano Letters* **6**, 827–832 (2006).
- [102] E. Prodan, C. Radloff, N. J. Halas, and P. Nordlander, "A hybridization model for the plasmon response of complex nanostructures," *Science* **302**, 419–422 (2003).
- [103] M. Moskovits, "Surface-enhanced Raman spectroscopy: a brief retrospective," *Journal of Raman Spectroscopy* **36**, 485–496 (2005).
- [104] P. L. Stiles, J. A. Dieringer, N. C. Shah, and R. P. Van Duyne, "Surface-enhanced Raman spectroscopy," *Annual Review of Analytical Chemistry* **1**, 601–26 (2008).
- [105] S.-Y. Lien, C.-H. Yang, C.-H. Hsu, Y.-S. Lin, C.-C. Wang, and D.-S. Wu, "Optimization of textured structure on crystalline silicon wafer for heterojunction solar cell," *Materials Chemistry and Physics* **133**, 63–68 (2012).

-
- [106] A. Taflové and S. C. Hagness, *Computational Electrodynamics: The Finite-Difference Time-Domain Method* (Artech House, Boston, 2005).
- [107] S. Humphries, *Field Solutions on Computers* (CRC Press, Boca Raton, 1997).
- [108] P. Monk, *Finite Element Methods for Maxwell's Equations* (Clarendon Press, Oxford, 2003).
- [109] L. Demkowicz, *Finite Element Methods for Maxwell Equations* (John Wiley & Sons, Ltd, Hoboken - New Jersey, 2007).
- [110] L. Li, "New formulation of the Fourier modal method for crossed surface-relief gratings," *Journal of the Optical Society of America A* **14**, 2758 (1997).
- [111] T. Weiland, "Diskretisierung der Maxwell-Gleichungen," *Physicalische Blätter* **7**, 191–201 (1986).
- [112] C. Rockstuhl, S. Fahr, F. Lederer, K. Bittkau, T. Beckers, and R. Carius, "Local versus global absorption in thin-film solar cells with randomly textured surfaces," *Applied Physics Letters* **93**, 061105 (2008).
- [113] P. Obermeyer, C. Haase, and H. Stiebig, "Advanced light trapping management by diffractive interlayer for thin-film silicon solar cells," *Applied Physics Letters* **92**, 181102 (2008).
- [114] C. Haase and H. Stiebig, "Optical properties of thin-film silicon solar cells with grating couplers," *Progress in Photovoltaics: Research and Applications* **14**, 629–641 (2006).
- [115] V. E. Ferry, M. A. Verschuuren, H. B. T. Li, E. Verhagen, R. J. Walters, R. E. I. Schropp, H. A. Atwater, and A. Polman, "Light trapping in ultrathin plasmonic solar cells," *Optics Express* **18**, 237–245 (2010).
- [116] U. W. Paetzold, E. Moulin, B. E. Pieters, U. Rau, and R. Carius, "Optical simulations and prototyping of microcrystalline silicon solar cells with integrated plasmonic reflection grating back contacts," in *Proceedings of SPIE* (San Diego, 2011), **8111**, 811107.
- [117] C. Heine and R. H. Morf, "Submicrometer gratings for solar energy applications," *Applied Optics* **34**, 2476–82 (1995).

- [118] M. Peters, M. Rüdiger, B. Bläsi, and W. Platzer, “Electrooptical simulation of diffraction in solar cells,” *Optics Express* **18**, 584 (2010).
- [119] D. Duche, P. Torchio, L. Escoubas, F. Monestier, J.-J. Simon, F. Flory, and G. Mathian, “Improving light absorption in organic solar cells by plasmonic contribution,” *Solar Energy Materials and Solar Cells* **93**, 1377–1382 (2009).
- [120] S. Burger, “Benchmark of FEM, waveguide and FDTD algorithms for rigorous mask simulation,” in *Proceedings of SPIE* (Monterey, 2005), **5992**, 599216.
- [121] J. Smajic, C. Hafner, L. Raguin, K. Tavzarashvili, and M. Mishrikey, “Comparison of Numerical Methods for the Analysis of Plasmonic Structures,” *Journal of Computational and Theoretical Nanoscience* **6**, 763–774 (2009).
- [122] “JCMsuite version 2.40,” JCMWave GmbH, Berlin, Germany (09.08.2011). (URL: <http://www.jcmwave.com/>, 25.08.2011).
- [123] “JCMsolve - Tutorial Electromagnetics,” JCMWave GmbH (2009). (URL: <http://www.jcmwave.com/JCMsuite/doc/html>, 01.02.2011).
- [124] L. Zschiedrich, “Transparent Boundary Conditions for Maxwells Equations: Numerical Concepts beyond the PML Method,” Doctoral thesis, Freie Universität Berlin (2009).
- [125] L. Zschiedrich, R. Klose, A. Schädle, and F. Schmidt, “A new finite element realization of the perfectly matched layer method for Helmholtz scattering problems on polygonal domains in two dimensions,” *Journal of Computational and Applied Mathematics* **188**, 12–32 (2006).
- [126] X. Deng and E. Schiff, *Handbook of Photovoltaic Science and Engineering*. (A. Luque and S. Hegedus, Hoboken - New Jersey, 2003), chap. Amorphous Silicon-based Solar Cells, pp. 505–565.
- [127] O. Vetterl, A. Lambertz, A. Dasgupta, F. Finger, B. Rech, O. Kluth, and H. Wagner, “Thickness dependence of microcrystalline silicon solar cell properties,” *Solar Energy Materials and Solar Cells* **66**, 345–351 (2001).
- [128] S. Klein, F. Finger, R. Carius, and H. Stiebig, “Light-induced degradation of microcrystalline silicon thin-film solar cells prepared by hot-wired cvd,” in *Proceedings of the 19th EUPVSEC* (Paris, 2004), 1579.

-
- [129] M. A. Green, "Lambertian light trapping in textured solar cells and light-emitting diodes: analytical solutions," *Progress in Photovoltaics: Research and Applications* **10**, 235–241 (2002).
- [130] A. Luque, *Solar Cells and Optics for Photovoltaic Concentration* (Taylor & Francis, Bristol, 1989).
- [131] E. Yablonovitch, "Statistical ray optics," *Journal of the Optical Society of America* **72**, 899 (1982).
- [132] E. Yablonovitch and G. Cody, "Intensity enhancement in textured optical sheets for solar cells," *IEEE Transactions on Electron Devices* **29**, 300–305 (1982).
- [133] P. Campbell and M. Green, "The limiting efficiency of silicon solar cells under concentrated sunlight," *IEEE Transactions on Electron Devices* **33**, 234–239 (1986).
- [134] A. Luque and J. C. Miñano, "Optical aspects in photovoltaic energy conversion," *Solar Cells* **31**, 237–258 (1991).
- [135] C. Ulbrich, S. Fahr, J. Üpping, M. Peters, T. Kirchartz, C. Rockstuhl, R. Wehrspohn, A. Gombert, F. Lederer, and U. Rau, "Directional selectivity and ultra-light-trapping in solar cells," *physica status solidi (a)* **205**, 2831–2843 (2008).
- [136] H. W. Deckman, "Optically enhanced amorphous silicon solar cells," *Applied Physics Letters* **42**, 968 (1983).
- [137] P. Campbell and M. A. Green, "Light trapping properties of pyramidally textured surfaces," *Journal of Applied Physics* **62**, 243 (1987).
- [138] R. A. Pala, J. White, E. Barnard, J. Liu, and M. L. Brongersma, "Design of Plasmonic Thin-Film Solar Cells with Broadband Absorption Enhancements," *Advanced Materials* **21**, 3504–3509 (2009).
- [139] R. Biswas and C. Xu, "Nano-crystalline silicon solar cell architecture with absorption at the classical $4n^2$ limit," *Optics Express* **19**, 664–672 (2011).
- [140] V. E. Ferry, L. A. Sweatlock, D. Pacifici, and H. A. Atwater, "Plasmonic nanostructure design for efficient light coupling into solar cells," *Nano Letters* **8**, 4391–4397 (2008).

- [141] S. Fahr, C. Rockstuhl, and F. Lederer, "Metallic nanoparticles as intermediate reflectors in tandem solar cells," *Applied Physics Letters* **95**, 121105 (2009).
- [142] C. Eisele, C. E. Nebel, and M. Stutzmann, "Periodic light coupler gratings in amorphous thin film solar cells," *Journal of Applied Physics* **89**, 7722 (2001).
- [143] J. Bhattacharya, N. Chakravarty, S. Pattnaik, W. Dennis Slafer, R. Biswas, and V. L. Dalal, "A photonic-plasmonic structure for enhancing light absorption in thin film solar cells," *Applied Physics Letters* **99**, 131114 (2011).
- [144] W. Bai, Q. Gan, F. Bartoli, J. Zhang, L. Cai, Y. Huang, and G. Song, "Design of plasmonic back structures for efficiency enhancement of thin-film amorphous Si solar cells," *Optics Letters* **34**, 3725–3727 (2009).
- [145] J. Üpping, A. Bielawny, R. B. Wehrspohn, T. Beckers, R. Carius, U. Rau, S. Fahr, C. Rockstuhl, F. Lederer, M. Kroll, T. Pertsch, L. Steidl, and R. Zentel, "Three-dimensional photonic crystal intermediate reflectors for enhanced light-trapping in tandem solar cells." *Advanced Materials* **23**, 3896–3900 (2011).
- [146] H. Sai and M. Kondo, "Effect of self-orderly textured back reflectors on light trapping in thin-film microcrystalline silicon solar cells," *Journal of Applied Physics* **105**, 094511 (2009).
- [147] C. Battaglia, C.-M. Hsu, K. Söderström, J. Escarré, F.-J. Haug, M. Charrière, M. Boccard, M. Despeisse, D. Alexander, M. Cantoni, Y. Cui, and C. Ballif, "Light Trapping in Solar Cells: Can Periodic Beat Random?" *ACS NANO* **6**, 2790–2797 (2012).
- [148] N. Senoussaoui, M. Krause, J. Müller, E. Bunte, T. Brammer, and H. Stiebig, "Thin-film solar cells with periodic grating coupler," *Thin Solid Films* **451-452**, 397–401 (2004).
- [149] D. Zhou and R. Biswas, "Photonic crystal enhanced light-trapping in thin film solar cells," *Journal of Applied Physics* **103**, 093102 (2008).
- [150] O. Isabella, B. Lipovšek, J. Krč, and M. Zeman, "Photonic Crystal Back Reflector in Thin-film Silicon Solar Cells," in *MRS Proceedings* (San Francisco, 2011), **1153**, 1153–A03–05.

-
- [151] Z. Yu, A. Raman, and S. Fan, "Fundamental limit of nanophotonic light trapping in solar cells," *Proceedings of the National Academy of Sciences of the United States of America* **107**, 17491–17496 (2010).
- [152] Z. Yu, A. Raman, and S. Fan, "Fundamental limit of light trapping in grating structures," *Optics Express* **18**, 366–380 (2010).
- [153] D. Redfield, "Multiple-pass thin-film silicon solar cell," *Applied Physics Letters* **25**, 647 (1974).
- [154] M. Green, A. Wang, and S. Wenham, "Very high efficiency silicon solar cells—science and technology," *IEEE Transactions on Electron Devices* **46**, 1940–1947 (1999).
- [155] M. A. Green, "Surface texturing and patterning in solar cells," *Advances in Solar Energy* **8**, 231–269 (1993).
- [156] J. Zhao, A. Wang, M. A. Green, and F. Ferrazza, "19.8% Efficient Honeycomb Textured Multicrystalline and 24.4% Monocrystalline Silicon Solar Cells," *Applied Physics Letters* **73**, 1991 (1998).
- [157] J. Müller, B. Rech, J. Springer, and M. Vanecek, "TCO and light trapping in silicon thin film solar cells," *Solar Energy* **77**, 917–930 (2004).
- [158] T. Söderström, F.-J. Haug, X. Niquille, and C. Ballif, "TCOs for nip thin film silicon solar cells," *Progress in Photovoltaics: Research and Applications* **17**, 165–176 (2009).
- [159] M. Zeman, J. Willems, L. Vosteen, G. Tao, and J. Metselaar, "Computer modelling of current matching in a-Si : H/a-Si : H tandem solar cells on textured TCO substrates," *Solar Energy Materials and Solar Cells* **46**, 81–99 (1997).
- [160] K. Bittkau, W. Böttler, M. Ermes, V. Smirnov, and F. Finger, "Light scattering at textured back contacts for n-i-p thin-film silicon solar cells," *Journal of Applied Physics* **111**, 083101 (2012).
- [161] K. Ding, T. Kirchartz, B. E. Pieters, C. Ulbrich, A. M. Ermes, S. Schicho, A. Lambert, R. Carius, and U. Rau, "Characterization and simulation of a-Si:H/ μ c-Si:H tandem solar cells," *Solar Energy Materials and Solar Cells* **95**, 3318–3327 (2011).

- [162] J. Krč, M. Zeman, F. Smole, and M. Topič, “Optical modelling of thin-film silicon solar cells deposited on textured substrates,” *Thin Solid Films* **451-452**, 298–302 (2004).
- [163] M. Schulte, K. Bittkau, K. Jager, M. Ermes, M. Zeman, and B. E. Pieters, “Angular resolved scattering by a nano-textured ZnO/silicon interface,” *Applied Physics Letters* **99**, 111107 (2011).
- [164] D. Dominé, F.-J. Haug, C. Battaglia, and C. Ballif, “Modeling of light scattering from micro- and nanotextured surfaces,” *Journal of Applied Physics* **107**, 044504 (2010).
- [165] C. Ulbrich, A. Gerber, K. Hermans, A. Lambertz, and U. Rau, “Analysis of short-circuit current gains by an anti-reflective textured cover on silicon thin-film solar cells,” *Progress in Photovoltaics: Research and Applications* (submitted 2012).
- [166] C. Ulbrich, M. Peters, B. Bläsi, T. Kirchartz, A. Gerber, and U. Rau, “Enhanced light trapping in thin-film solar cells by a directionally selective filter,” *Optics Express* **18**, 133–138 (2010).
- [167] S. Fahr, C. Ulbrich, T. Kirchartz, U. Rau, C. Rockstuhl, and F. Lederer, “Rugate filter for light-trapping in solar cells,” *Optics Express* **16**, 9332–9343 (2008).
- [168] A. Bielawny, J. Üpping, P. T. Miclea, R. B. Wehrspohn, C. Rockstuhl, F. Lederer, M. Peters, L. Steidl, R. Zentel, S.-M. Lee, M. Knez, A. Lambertz, and R. Carius, “3D photonic crystal intermediate reflector for micromorph thin-film tandem solar cell,” *physica status solidi (a)* **205**, 2796–2810 (2008).
- [169] H. Sai, H. Fujiwara, and M. Kondo, “Back surface reflectors with periodic textures fabricated by self-ordering process for light trapping in thin-film microcrystalline silicon solar cells,” *Solar Energy Materials and Solar Cells* **93**, 1087–1090 (2009).
- [170] M. Kroll, S. Fahr, C. Helgert, C. Rockstuhl, F. Lederer, and T. Pertsch, “Employing dielectric diffractive structures in solar cells - a numerical study,” *physica status solidi (a)* **205**, 2777–2795 (2008).

-
- [171] R. Dewan and D. Knipp, "Light trapping in thin-film silicon solar cells with integrated diffraction grating," *Journal of Applied Physics* **106**, 074901 (2009).
- [172] P. Spinelli, V. E. Ferry, J. van de Groep, M. van Lare, M. A. Verschuuren, R. E. I. Schropp, H. A. Atwater, and A. Polman, "Plasmonic light trapping in thin-film Si solar cells," *Journal of Optics* **14**, 024002 (2012).
- [173] U. W. Paetzold, E. Moulin, D. Michaelis, W. Bottler, C. Wachter, V. Hagemann, M. Meier, R. Carius, and U. Rau, "Plasmonic reflection grating back contacts for microcrystalline silicon solar cells," *Applied Physics Letters* **99**, 181105 (2011).
- [174] S. Pillai, K. R. Catchpole, T. Trupke, and M. A. Green, "Surface plasmon enhanced silicon solar cells," *Journal of Applied Physics* **101**, 093105 (2007).
- [175] C. Hagglund, M. Zach, G. Petersson, and B. Kasemo, "Electromagnetic coupling of light into a silicon solar cell by nanodisk plasmons," *Applied Physics Letters* **92**, 053110 (2008).
- [176] M. Westphalen, U. Kreibig, J. Rostalski, H. Lüth, and D. Meissner, "Metal cluster enhanced organic solar cells," *Solar Energy Materials and Solar Cells* **61**, 97–105 (2000).
- [177] D. Derkacs, S. H. Lim, P. Matheu, W. Mar, and E. T. Yu, "Improved performance of amorphous silicon solar cells via scattering from surface plasmon polaritons in nearby metallic nanoparticles," *Applied Physics Letters* **89**, 093103 (2006).
- [178] S. Nunomura, A. Minowa, H. Sai, and M. Kondo, "Mie scattering enhanced near-infrared light response of thin-film silicon solar cells," *Applied Physics Letters* **97**, 063507 (2010).
- [179] V. E. Ferry, M. A. Verschuuren, M. C. V. Lare, R. E. I. Schropp, H. A. Atwater, and A. Polman, "Optimized spatial correlations for broadband light trapping nanopatterns in high efficiency ultrathin film a-Si:H solar cells," *Nano Letters* **11**, 4239–4245 (2011).
- [180] C. Eminian, F.-J. Haug, O. Cubero, X. Niquille, and C. Ballif, "Photocurrent enhancement in thin film amorphous silicon solar cells with silver nanoparticles," *Progress in Photovoltaics: Research and Applications* **19**, 260–265 (2011).

- [181] E. Moulin, J. Sukmanowski, P. Luo, R. Carius, F. Royer, and H. Stiebig, "Improved light absorption in thin-film silicon solar cells by integration of silver nanoparticles," *Journal of Non-Crystalline Solids* **354**, 2488–2491 (2008).
- [182] U. W. Paetzold, E. Moulin, B. E. Pieters, R. Carius, and U. Rau, "Design of nanostructured plasmonic back contacts for thin-film silicon solar cells," *Optics Express* **19**, 1219 (2011).
- [183] E. A. Schiff, "Thermodynamic limit to photonic-plasmonic light-trapping in thin films on metals," *Journal of Applied Physics* **110**, 104501 (2011).
- [184] C. Hägglund and S. P. Apell, "Plasmonic Near-Field Absorbers for Ultrathin Solar Cells," *The Journal of Physical Chemistry Letters* pp. 1275–1285 (2012).
- [185] C. Rockstuhl, S. Fahr, and F. Lederer, "Absorption enhancement in solar cells by localized plasmon polaritons," *Journal of Applied Physics* **104**, 123102 (2008).
- [186] U. W. Paetzold, "Plasmonic effects in thin-film silicon solar cells," Doctoral thesis, RWTH Aachen University (2009).
- [187] P. Senanayake, C.-H. Hung, J. Shapiro, A. Lin, B. Liang, B. S. Williams, and D. L. Huffaker, "Surface Plasmon-Enhanced Nanopillar Photodetectors," *Nano Letters* **11**, 5279–5283 (2011).
- [188] V. Shalaev, C. Douketis, J. Stuckless, and M. Moskovits, "Light-induced kinetic effects in solids," *Physical Review B* **53**, 11388–11402 (1996).
- [189] E. Moulin, P. Luo, B. Pieters, J. Sukmanowski, J. Kirchhoff, W. Reetz, T. Müller, R. Carius, F.-X. Royer, and H. Stiebig, "Photoresponse enhancement in the near infrared wavelength range of ultrathin amorphous silicon photosensitive devices by integration of silver nanoparticles," *Applied Physics Letters* **95**, 033505 (2009).
- [190] M. Meier, U. W. Paetzold, M. Prömpers, T. Merdzahnova, R. Carius, and A. Gordijn, "UV nanoimprint for the replication of etched ZnO:Al textures applied in thin-film silicon solar cells," *Progress in Photovoltaics: Research and Applications* (in press, DOI:10.1002/pip.2382).

-
- [191] U. W. Paetzold, W. Zhang, M. Prömpers, J. Kirchhoff, T. Merdzhanova, S. Michard, R. Carius, A. Gordijn, and M. Meier, "Thin-film silicon solar cell development on imprint-textured glass substrates," *Materials Science and Engineering B* **178**, 617–622 (2013).
- [192] S. Y. Chou, P. R. Krauss, and P. J. Renstrom, "Imprint Lithography with 25-Nanometer Resolution," *Science* **272**, 85–87 (1996).
- [193] A. Boltasseva, "Plasmonic components fabrication via nanoimprint," *Journal of Optics A: Pure and Applied Optics* **11**, 114001 (2009).
- [194] E. A. Costner, M. W. Lin, W.-I. Jen, and C. G. Willson, "Nanoimprint Lithography Materials Development for Semiconductor Device Fabrication," *Annual Review of Materials Research* **39**, 180 (2009).
- [195] M. Meier, C. Nauenheim, S. Gilles, D. Mayer, and C. Ku, "Nanoimprint for future non-volatile memory and logic devices," *Microelectronic Engineering* **85**, 870–872 (2008).
- [196] "International Technology Roadmap for Semiconductors - 2011," Semiconductor Industry Association (2011).
(URL: <http://www.itrs.net/>, 15.04.2012).
- [197] M. D. Austin, H. Ge, W. Wu, M. Li, and Z. Yu, "Fabrication of 5 nm linewidth and 14 nm pitch features by nanoimprint lithography," *Applied Physics Letters* **84**, 5299–5301 (2004).
- [198] S. Gilles, "Nanoimprint Lithographie als Methode zur chemischen Oberflächenstrukturierung für Anwendungen in der Bioelektronik," Doctoral thesis, RWTH Aachen University (2010).
- [199] M. Meier, "Entwicklung einer Nanotechnologie-Plattform für die Herstellung Crossbar-basierter Speicherarchitekturen," Doctoral thesis, RWTH Aachen University (2009).
- [200] J. Escarré, K. Söderström, C. Battaglia, F.-j. Haug, and C. Ballif, "Solar Energy Materials & Solar Cells High fidelity transfer of nanometric random textures by UV embossing for thin film solar cells applications," *Solar Energy Materials and Solar Cells* **95**, 881–886 (2011).

- [201] C. Battaglia, J. Escarré, K. Söderström, L. Erni, L. Ding, G. Bugnon, A. Billet, M. Boccard, L. Barraud, S. De Wolf, F.-J. Haug, M. Despeisse, and C. Ballif, “Nanoimprint lithography for high-efficiency thin-film silicon solar cells,” *Nano Letters* **11**, 661–665 (2011).
- [202] M. Kondo, Y. Toyoshima, A. Matsuda, and K. Ikuta, “Substrate dependence of initial growth of microcrystalline silicon in plasma-enhanced chemical vapor deposition,” *Journal of Applied Physics* **80**, 6061 (1996).
- [203] L. L. Smith, E. Srinivasan, and G. N. Parsons, “Investigation of substrate-dependent nucleation of plasma-deposited microcrystalline silicon on glass and silicon substrates using atomic force microscopy,” *Journal of Applied Physics* **82**, 6041 (1997).
- [204] J. I. Owen, J. Hüpkens, H. Zhu, E. Bunte, and S. E. Pust, “Novel etch process to tune crater size on magnetron sputtered ZnO:Al,” *physica status solidi (a)* **208**, 109–113 (2011).
- [205] Q. Xia, W. M. Tong, W. Wu, J. J. Yang, X. Li, W. Robinett, T. Cardinali, M. Cumbie, J. E. Ellenson, P. Kuekes, and R. S. Williams, “On the integration of memristors with CMOS using nanoimprint lithography,” in *Proceedings of SPIE* (San Jose, 2009), **7271**, 727106.
- [206] S. Gilles, M. Meier, M. Prömpers, A. V. D. Hart, C. Kügeler, A. Offenhäusser, and D. Mayer, “UV nanoimprint lithography with rigid polymer molds,” *Microelectronic Engineering* **86**, 661–664 (2009).
- [207] M. Schmid, R. Klenk, M. C. Lux-Steiner, M. Topic, and J. Krc, “Modeling plasmonic scattering combined with thin-film optics,” *Nanotechnology* **22**, 025204 (2011).
- [208] J. Springer, A. Poruba, L. Müllerova, M. Vanecek, O. Kluth, and B. Rech, “Absorption loss at nanorough silver back reflector of thin-film silicon solar cells,” *Journal of Applied Physics* **95**, 1427 (2004).
- [209] F.-J. Haug, T. Söderström, O. Cubero, V. Terrazzoni-Daudrix, and C. Ballif, “Plasmonic absorption in textured silver back reflectors of thin film solar cells,” *Journal of Applied Physics* **104**, 064509 (2008).

-
- [210] F.-J. Haug, T. Söderström, O. Cubero, V. Terrazzoni-Daudrix, and C. Ballif, "Influence of the ZnO buffer on the guided mode structure in Si/ZnO/Ag multilayers," *Journal of Applied Physics* **106**, 044502 (2009).
- [211] U. W. Paetzold, F. Hallermann, B. E. Pieters, U. Rau, R. Carius, and G. von Plessen, "Localized plasmonic losses at metal back contacts of thin-film silicon solar cells," in *Proceedings of SPIE* (Brussels, 2010), **7725**, 772517.
- [212] E. Moulin, U. W. Paetzold, H. Siekmann, J. Worbs, A. Bauer, and R. Carius, "Study of thin-film silicon solar cell back reflectors and potential of detached reflectors," *Energy Procedia* **10**, 106–110 (2011).
- [213] E. Moulin, U. W. Paetzold, J. Kirchhoff, A. Bauer, and R. Carius, "Study of detached back reflector designs for thin-film silicon solar cells," *physica status solidi (RRL) - Rapid Research Letters* **6**, 65–67 (2012).
- [214] U. W. Paetzold, C. Haase, and H. Stiebig, "Localized Plasmonic Effects at Metal Back Contacts of Thin-Film Silicon Solar Cells," in *Proceedings of the 24th EUPVSEC* (Hamburg, 2009), 2779–2783.
- [215] U. W. Paetzold, M. Meier, E. Moulin, V. Smirnov, B. E. Pieters, U. Rau, and R. Carius, "Plasmonic Back Contacts with Non-Ordered Ag Nanostructures for Light Trapping in Thin-Film Silicon Solar Cells," *Materials Science and Engineering B* **178**, 630 – 634 (2013).
- [216] E. Moulin, "Thin-Film Silicon Solar Cells with Integrated Metal Nanoparticles and Metal Nanostructures for an Enhanced Light Absorption," Doctoral thesis, University Paul Verlaine - Metz (2009).
- [217] U. W. Paetzold, E. Moulin, B. E. Pieters, U. Rau, and R. Carius, "Optical simulations of microcrystalline silicon solar cells applying plasmonic reflection grating back contacts," *Journal of Photonics for Energy* **2**, 027002 (2012).
- [218] R. Brendel, *Thin-Film Crystalline Silicon Solar Cells - Physics and Technology* (WILEY-VCH, Berlin, 2003).
- [219] K. R. Catchpole, M. J. McCann, K. J. Weber, and A. W. Blakers, "A review of thin-film crystalline silicon for solar cell applications. Part 2: Foreign substrates," *Solar Energy Materials and Solar Cells* **68**, 173–215 (2001).

- [220] E. D. Palik, *Handbook of optical constants of solids* (Academic Press, San Diego, 1985).

List of Symbols and Abbreviations

Symbol	Description	Unit
A	Absorptance	-
A_{\max}	Maximal absorptance	-
AFM	Atomic force microscopy	
\mathbf{B}	Magnetic induction vector	T
c_0	Speed of light in vacuum	m/s
\mathbf{D}	Dielectric displacement vector	C/m ²
\mathbf{E}	Electric field vector	V/m
\mathbf{E}_0	Electric field strength (vector)	V/m
EQE	External quantum efficiency	-
FEM	Finite element method	
FF	Fill factor	-
G_{mn}	Two-dimensional grating constant	
\mathbf{H}	Magnetic field vector	A/m
HCl	Hydrochloric acid	
\mathbf{J}_{ext}	External electric current density (vector)	A/m ²
J_{mpp}	Current density at the maximum power point	mA/cm ²
J_{sc}	Short-circuit current density	mA/cm ²
\mathbf{k}	Wavevector	1/m
LSPP	Localized surface plasmon polariton	
\tilde{n}	Complex refractive index	-
n	Real part of the refractive index	-
NIL	Nanoimprint lithography	

Symbol	Description	Unit
PECVD	Plasma enhanced chemical vapor deposition	
Q_{abs}	Absorption efficiency	-
Q_{sca}	Scattering efficiency	-
\bar{Q}_{sca}	Averaged scattering efficiency	-
\bar{Q}_{abs}	Averaged absorption efficiency	-
$\max. Q_{\text{sca}}$	Maximum of Q_{sca} of a LSPP resonance	-
$\max. Q_{\text{abs}}$	Maximum of Q_{abs} of a LSPP resonance	-
P_0	Irradiated power	W
R, R_{tot}	Total reflectance	-
R_{diff}	Diffuse reflectance	-
$R_{\text{non-spec}}$	Non-specular reflectance	-
SEM	Scanning electron microscopy	
SiO_2	Silicon dioxide	-
SnO_2	Tin oxide	-
SPP	Surface plasmon polariton	
TCO	Transparent conductive oxide	
TE	Transversal electric	
TM	Transversal magnetic	
UV	Ultra violet light	
UV-NIL	Ultra violet nanoimprint lithography	
V_{mpp}	Voltage at the maximum power point	mV
V_{oc}	Open-circuit voltage	mV
ZnO:Al	Aluminium doped zinc oxide	
α	Absorption coefficient	1/cm
$a\text{-Si:H}$	Hydrogenated amorphous silicon	
ϵ	Dielectric constant	-
ϵ_0	Vacuum permittivity	F/m
η	Energy conversion efficiency	-
κ	Extinction coefficient	-
λ	Wavelength	nm
λ_{SPP}	Resonance wavelength of propagating SPPs	nm
$\mu\text{c-Si:H}$	Hydrogenated microcrystalline silicon	
μ	Relative permeability	-
μ_0	Vacuum permeability	Vs/(Am)
ρ_{ext}	Scalar free charge density	C/m ²
σ	Conductivity	1/(Ωm)
ω	Angular frequency	1/s
ω_{SPP}	Resonance frequency of propagating SPP	1/s

List of Publications

Journal Publications Related to This Work

1. U. W. Paetzold, E. Moulin, D. Michaelis, W. Böttler, C. Wachter, V. Hagemann, M. Meier, R. Carius, and U. Rau, "Plasmonic reflection grating back contacts for microcrystalline silicon solar cells," *Applied Physics Letters* **99**, 181105 (2011).
2. U. W. Paetzold, E. Moulin, B. E. Pieters, R. Carius, and U. Rau, "Design of nanostructured plasmonic back contacts for thin-film silicon solar cells," *Optics Express* **19**, 1219 - 1230 (2011).
3. E. Moulin, U. W. Paetzold, H. Siekmann, J. Worbs, A. Bauer, and R. Carius, "Study of thin-film silicon solar cell back reflectors and potential of detached reflectors," *Energy Procedia* **10**, 106 - 110 (2011).
4. U. W. Paetzold, E. Moulin, B. E. Pieters, U. Rau, and R. Carius, "Optical simulations of microcrystalline silicon solar cells applying plasmonic reflection grating back contacts," *Journal of Photonics for Energy* **2**, 027002 (2012).
5. E. Moulin, U. W. Paetzold, J. Kirchhoff, A. Bauer, and R. Carius, "Study of detached back reflector designs for thin-film silicon solar cells," *physica status solidi (RRL) - Rapid Research Letters* **6**, 65 - 67 (2012).
6. M. Meier, U. W. Paetzold, M. Prömpers, T. Merdzahnova, R. Carius, and A. Gordijn, "UV nanoimprint for the replication of etched ZnO:Al textures applied in thin-film silicon solar cells," *Progress in Photovoltaics: Research and Applications* (in press, DOI:10.1002/pip.2382).

7. U. W. Paetzold, W. Zhang, M. Prömpers, J. Kirchhoff, T. Merdzhanova, S. Michard, R. Carius, A. Gordijn, and M. Meier, "Thin-film silicon solar cell development on imprint-textured glass substrates," *Materials Science and Engineering B* **178**, 617 - 622 (2013).
8. U. W. Paetzold, M. Meier, E. Moulin, V. Smirnov, B. E. Pieters, U. Rau, and R. Carius, "Plasmonic Back Contacts with Non-Ordered Ag Nanostructures for Light Trapping in Thin-Film Silicon Solar Cells," *Materials Science and Engineering B* **178**, 630 - 634 (2013).
9. E. Moulin, U. W. Paetzold, K. Bittkau, M. A. Ermes, L. Ding, L. Fanni, S. Nicolay, J. Kirchhoff, A. Bauer, A. Lambertz, C. Ballif, and R. Carius, "Thin-Film Silicon Solar Cells Applying Optically Decoupled Back Reflectors," *Materials Science and Engineering B* **178**, 645 - 650 (2013)).

Contributions to Conference Proceedings Related to This Work

1. U. W. Paetzold, C. Haase, and H. Stiebig, "Localized Plasmonic Effects at Metal Back Contacts of Thin-Film Silicon Solar Cells," in *Proceedings of the 24th EUPVSEC* (Hamburg,2009), 2779 - 2783.
2. C. Jandl, W. Dewald, U. W. Paetzold, A. Gordijn, C. Pflaum, and H. Stiebig, "Simulation of tandem thin-film silicon solar cells," in *Proceedings of SPIE* (Brussels,2010), **7725**,772516.
3. U. W. Paetzold, F. Hallermann, B. E. Pieters, U. Rau, R. Carius, and G. von Plessen, "Localized plasmonic losses at metal back contacts of thin-film silicon solar cells," in *Proceedings of SPIE* (Brussels,2010), **7725**, 772517.
4. U. W. Paetzold, E. Moulin, K. Bittkau, B. E. Pieters, R. Carius, and U. Rau, "Localized Plasmon Assisted Scattering at the Back Contact of Thin-Film Silicon Solar Cells" in *Proceedings of the 25th EUPVSEC* (Valencia,2010), 3036 - 3041.
5. R. Carius, U. W. Paetzold, and E. Moulin, "Light Harvesting in Thin Film Silicon Solar Cells and Detectors by Ag Nanostructures," in *Proceedings of the IEEE Photonics Conference* (Arlington,2011), **1**, 861 - 862.

6. U. W. Paetzold, E. Moulin, B. E. Pieters, U. Rau, and R. Carius, "Optical simulations and prototyping of microcrystalline silicon solar cells with integrated plasmonic reflection grating back contacts," in *Proceedings of SPIE* (San Diego, 2011), **8111**, 811107.

Further Journal Publications

1. M. Meier, T. Merdzhanova, U. W. Paetzold, S. Muthmann, A. Mck, R. Schmitz, and Aad Gordijn, "In Situ Current Determination of a-Si/ μ c-Si Tandem Solar Cells via Transmission Measurements During Silicon PECVD," *IEEE Journal of Photovoltaics* **2**, 1 - 6 (2011).

Acknowledgments

Last but not least, I want to thank all people who contributed to this work in one way or another. This thesis would not have been possible without your support.

Thank you very much !

I wish to express my special gratitude to ...

Prof. Dr. Gero von Plessen for the supervision of this thesis and the interest in the topic. Discussions with an expert in the field of nanooptics and plasmonics have been very valuable.

Prof. Dr. Uwe Rau for his continuous scientific incitements along with extensive support. I am very thankful for his confidence in my work and his encouragement during difficult steps.

Prof. Dr. Reinhard Carius for being abundantly helpful and offering invaluable support. I am deeply grateful for his advices, critical reflections, and patient guidance. His ideas, perspectives and constructive criticism helped me through the challenging moments of this work.

Matthias Meier for being a wonderful coworker, pushing the topic nanoimprint and sharing my type of humour.

Tsvetelina Merdzhanova for always offering help when help was needed and giving motivation in challenging moments.

Urs Aeberhard for revealing and wonderful discussions on science as well as virtually everything ranging from politics to economics and ethics.

Etienne Moulin for being an exceptional helpful colleague and sharing his experience on plasmonics with me.

Stefan Michard for intensive discussions and the fun time in the joint carpool.

Sascha Pust for helping out with his expertise in chemistry whenever it was needed, knowing answers to all administrative questions and being the perfect office neighbour.

Bart E. Pieters for his interest in my work, the numerous discussions on the simulations and the help whenever help was needed.

Karsten Bittkau for sharing his knowledge on light trapping with me and discussing several difficulties in my work.

Kaining Ding, Markus Ermes, Friedhelm Fingers, Aad Gordijn, Christian Haase, Jürgen Hüpkens, Andreas Lambertz, Vladimir Smirnov, Caroline Ulbrich and Wendi Zhang for in-depth discussions on problems and details of my work.

Michael Prömpers, Rebecca van Aubel, Wanjiao Böttler, Hans Peter Bochem, Alain Doumit, Markus Hülsbeck, Juraj Hotovy, Gunnar Schöpe, Joachim Kirchhoff, Josef Klomfaß, Hilde Siekmann, Wilfried Reetz for technical assistance and sample preparation.

Prof. Dr. Helmut Stiebig for introducing me into the field of plasmonics and the field of thin-film silicon solar cells.

Susanne Griesen, Astrid Nogga and Andrea Mühlheims for administrative support. all participants of the bilateral "Plasmonik-Treff" between the I. Institute of Physics at the RWTH Aachen University and the IEK5 - Photovoltaik at the Forschungszentrum Jülich. In particular, I thank Prof. Dr. Thomas Taubner for his support as well as Florian Hallerman, Daniela Schneevoigt and Alexander Sprafke for the help with darkfield microscopy measurements.

the partners of the project "SunPlas" which is funded by the German Federal Ministry of Education and Research (contract 03SF0354D).

Dirk Michaelis and Christoph Wächter from Fraunhofer-Institut für Angewandte Optik und Feinmechanik in Jena for sharing their knowledge on nanooptics and electromagnetic simulations.

Volker Hagemann from Schott AG in Mainz supported this work by providing textured samples prepared by nanoimprint lithography.

Sven Burger for technical support with the software of JCMwave.

Denise Parkinson for proofreading the manuscript.

Finally, I want to thank all my family and all my friends for supporting me throughout the last three years. I feel blessed with wonderful parents, Christian Paetzold and Berta Paetzold, who keep encouraging me. I am deeply thankful to Lena Schulze for always being at my side, making me laugh and supporting me.

Curriculum Vitae

Personal Data

Name: Ulrich Wilhelm Paetzold
 Address: Stephanstraße 10
 52064 Aachen
 Germany
 E-Mail: ulrich.paetzold@rwth-aachen.de
 Date of Birth: October 1st, 1982
 Place of Birth: Lingen(Ems), Germany

Education and Professional Experience

09/2009 -09/2012 **Doctoral studies** in physics at RWTH Aachen University and researcher at the IEK5 - Photovoltaik, Forschungszentrum Jülich GmbH (Jülich, Germany).
 04/2009-07/2009 **Internship with Schott AG** (Barcelona, Spain).
 08/2006-01/2011 **Studies in "industrial ecology - for a sustainable society"**, an interdisciplinary master program at Chalmers University of Technology (Gothenburg, Sweden).
 03/2008-03/2009 **Diploma candidate** and research assistant at the IEK5 - Photovoltaik, Forschungszentrum Jülich GmbH (Jülich, Germany).
 08/2006-07/2007 **UNITECH student** - the scientific studies at Chalmers University of Technology were complemented with insights in management theory and practice (Gothenburg, Sweden).
 10/2003-04/2009 **Diploma studies in physics** and intermediate examinations in mathematics at RWTH Aachen University (Aachen, Germany).
 08/2002-08/2003 **Volunteer social worker** with the Brazilian NGO AVI-CRES in the suburbs of Rio de Janeiro (Baixada Fluminense, Brazil).
 09/1993-06/2002 **Grammar School** - Gymnasium Nepomucenum Rietberg (Rietberg, Germany).

Band / Volume 171

Pulvermetallurgische Herstellung von porösem Titan und von NiTi-Legierungen für biomedizinische Anwendungen

M. Bram (2013), X, 238 pp

ISBN: 978-3-89336-866-2

Band / Volume 172

IEK-3 Report 2013. Langlebige Elektrochemische Verfahrenstechnik

(2013), ca. 185 pp

ISBN: 978-3-89336-868-6

Band / Volume 173

Combined Steady State and High Cycle Transient Heat Load Simulation with the Electron Beam Facility JUDITH 2

Th. Loewenhoff (2013), XVI, 108 pp

ISBN: 978-3-89336-869-3

Band / Volume 174

High-Quality Thorium TRISO Fuel Performance in HTGRs

K. Verfondern, H. Nabielek, M.J. Kania, H.-J. Allelein (2013), viii, 109 pp

ISBN: 978-3-89336-873-0

Band / Volume 175

Characterization of effective hydraulic properties of unsaturated porous media using spectral induced polarization (SIP)

K. Breede (2013), xiv, 72 pp

ISBN: 978-3-89336-875-4

Band / Volume 176

Zur Mikrostruktur siliziumbasierter Dünnschichten für die Photovoltaik

F. Köhler (2013), i, 100 pp

ISBN: 978-3-89336-876-1

Band / Volume 177

Grundlagen für die Transformation von Energiesystemen

Texte und Ergebnisse der Cadenabbia-Tagung 2012

der Konrad-Adenauer-Stiftung und des Forschungszentrum Jülich GmbH

L. Gruber, J.-F. Hake (Eds.) (2013), VI, 114 pp

ISBN: 978-3-89336-877-8

Band / Volume 178

Thermo - mechanical investigations and predictions for oxygen transport membrane materials

G. Pećanac (2013), 143 pp

ISBN: 978-3-89336-878-5

Band / Volume 179

**Thermomechanische Charakterisierung neu entwickelter
Feuerfestwerkstoffe**

E. Skiera (2013), III, 133 pp

ISBN: 978-3-89336-885-3

Band / Volume 180

**Entwicklung und Herstellung von metallgestützten Festelektrolyt-
Brennstoffzellen mit Hilfe des Hohlkathoden-Gasflusssputterns**

M. Haydn (2013), XVI, 174 pp

ISBN: 978-3-89336-886-0

Band / Volume 181

**Characterization and stability investigation of water dispersible colloids
(WDCs) in natural soils**

C. Jiang (2013), X, 102 pp

ISBN: 978-3-89336-887-7

Band / Volume 182

**Monazite-type Ceramics for Conditioning of Minor Actinides:
Structural Characterization and Properties**

C. Babelot (2013), x, 127 pp

ISBN: 978-3-89336-889-1

Band / Volume 183

**High-rate growth of hydrogenated amorphous and microcrystalline silicon
for thin-film silicon solar cells using dynamic very-high frequency plasma-
enhanced chemical vapor deposition**

T. Zimmermann (2013), x, 126 pp

ISBN: 978-3-89336-892-1

Band / Volume 184

IEK-3 Report 2013. Durable Electrochemical Process Engineering

(2013), ca. 180 pp

ISBN: 978-3-89336-893-8

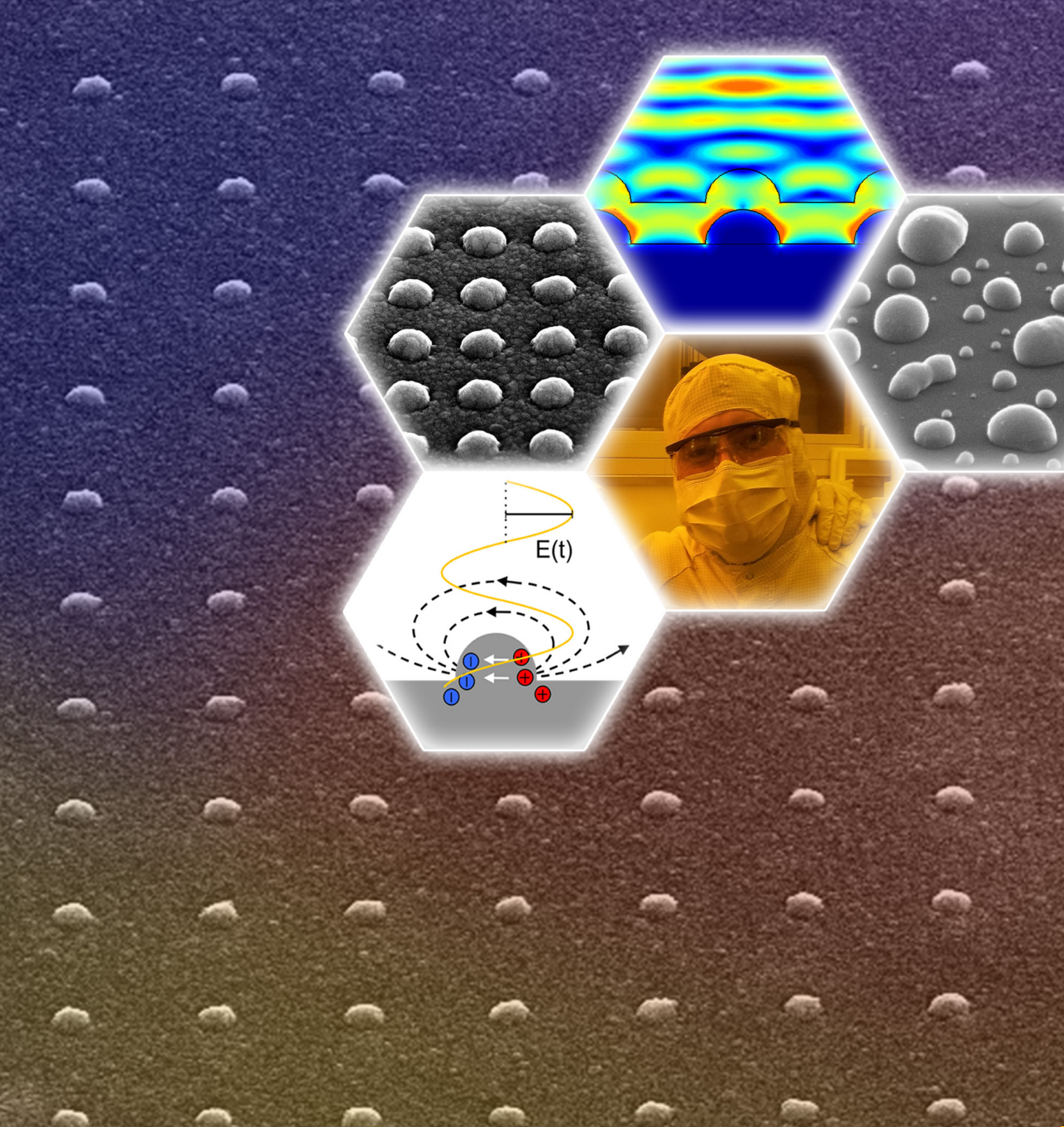
Band / Volume 185

**Light Trapping with Plasmonic Back Contacts in Thin-Film Silicon Solar
Cells**

U. W. Paetzold (2013), X, 175 pp

ISBN: 978-3-89336-895-2

Weitere **Schriften des Verlags im Forschungszentrum Jülich** unter
<http://wwwzb1.fz-juelich.de/verlagextern1/index.asp>



Energie & Umwelt / Energy & Environment
Band / Volume 185
ISBN 978-3-89336-895-2

